Electromagnetic Energy Harvesting Surfaces

by

Ahmed Z. Ashoor

A thesis
presented to the University of Waterloo
in fulfillment of the
thesis requirement for the degree of
Doctor of Philosophy
in
Electrical and Computer Engineering

Waterloo, Ontario, Canada, 2018

Examining Committee Membership

The following served on the Examining Committee for this thesis. The decision of the Examining Committee is by majority vote.

External Examiner: Mo Mojahedi
Professor, Dept. Dept. Electrical & Computer Engineering
University of Toronto

Supervisor: Omar M. Ramahi
Professor, Dept. Electrical & Computer Engineering
University of Waterloo

Internal Members: Safieddin Safavi-Naeini
Professor, Dept. Electrical & Computer Engineering
University of Waterloo

Karim S. Karim
Professor, Dept. Electrical & Computer Engineering
University of Waterloo

Internal-External Member: Sean Peterson
Associate Professor, Dept. of Mechanical & Mechatronics Engineering
University of Waterloo

Abstract

The concept of wireless power transfer (WPT) was successfully demonstrated in the early years of the 20th century. One promising application of using the WPT concept is the WPT transmission utilizing a large array of solar cells outside the earth's atmosphere to collect solar energy and then converts it to microwave power for transmission to earth using highly directive antennas. Space solar power (SSP) transmission concept may play an important role in the near future in harvesting clean and sustainable energy from space. The SSP concept calls for the large rectenna (i.e., antennas and rectifying circuitry) arrays farms that receive the microwave power that is transmitted from space and convert it into usable DC power. To obtain high power and high output voltage, the use of a large rectenna array is necessary, and hence the focus in this thesis is on improving the harvesting efficiency of rectenna systems.

The two main figures of merit to evaluate a WPT rectenna system are the radiation to AC efficiency, and the radiation to DC efficiency. The latter combines the efficiencies of the electromagnetic energy collectors or antenna, and that of the rectifying circuitry. In the progress towards improving the efficiency of a rectenna array system, efforts were heavily focused on improving the AC to DC conversion efficiencies. However, in most previous works, efforts to improve the efficiency of the antennas were not pursued. The majority of rectennas were in fact designed using conventional antennas because of their wide use in modern communications technologies but not for their particular ability or suitability to efficiently harvest electromagnetic radiation.

The first part of this thesis introduces, for the first time, the use of dielectric resonator antenna (DRA) in an array form as an energy harvester. A single DRA and a 1×3 array were used to build foundation profiles for using DRAs in an array form as an energy harvester. The proposed structures were designed and fabricated to maximize energy reception around 5.5 GHz. The size of the ground plane and coupling between dielectric resonator (DR) elements in an array were studied with special focus on the overall efficiency of the antenna structure for different incident polarizations. A 5×5 array was built and tested numerically and experimentally. Measurements showed that energy absorption efficiency as high as 67% can be achieved using an array of DRAs. Then an extension of this finding was carried out considering the DRA's fabrication challenges. A complementary DRAs structure consisting of DR blocks backed by cut grounds is proposed. It was shown through numerical simulations that the complementary DR blocks resonator can efficiently deliver the incident power carried by an electromagnetic wave to a load with an efficiency of 80%.

The concept of using an electromagnetic energy harvesting surface (EHS) structure is introduced in the second part of this thesis. A design of an electromagnetic EHS inspired by an array of printed metallic dipolar elements is introduced. The unit cell of the EHS is based on two printed asymmetric off-center fed dipoles. As a proof of concept, a finite array of 9×3 unit cells was analyzed numerically and experimentally to work at 3 GHz. The array was first analyzed for maximizing radiation to AC absorption where each dipole was terminated by a resistor across its gap. An overall radiation to DC harvesting efficiency of 76% was obtained experimentally.

The third part of this dissertation presents a design for a multi-polarization electromagnetic EHS inspired by a multi-layer unit cell of printed asymmetrical metallic dipolar elements. The harvesting array features two layers that collectively capture the incident energy from various incident angles. The harvester was first analyzed for maximizing the radiation to AC absorption at 3 GHz where each dipole was terminated by a resistor across its energy-collecting gap. As a proof of concept, a multi-layer array consisting of 3×3 asymmetrical dipolar elements of the multi-layer unit cell was fabricated and measured experimentally. The experimental results yielded an overall radiation to DC harvesting efficiency of 70% for multiple incident polarizations.

Next, an EHS is introduced for receiving multiple polarizations while using only one metallization layer. The EHS unit cell is based on two cross-dipoles that enable capturing the energy from various angles of illuminations at an operating frequency of 3 GHz. The simulation results yielded a radiation to AC efficiency of 94% at multiple angles of polarization. For validation, a finite array of 7×7 unit cells was fabricated and tested experimentally. The experimental results of the EHS energy harvesting array show an overall radiation to DC harvesting efficiency of 74% at various polarization angles. A critical design feature of the proposed cross-dipole EHS array is that it allows direct matching to a rectifying circuitry at the dipoles plane.

The thesis concludes by introducing an efficient dual-band EHS array using two stacked-layer of cross-dipole elements for efficient harvesting at two frequency bands for multiple polarizations. The proposed EHS array introduces the concept of stacked surfaces that can be directly integrated with the rectification circuitry. The multilayer EHS array allows direct matching to a rectifying circuitry such that DC power is collected at the elements' plane for each layer. The total achieved harvested DC power is the collective contribution of the rectified DC power from the EHS's layers. A finite multi-layer array of 7×7 unit cells was fabricated and tested experimentally. The experimental results of the dual-band EHS energy harvesting array show an overall radiation to DC harvesting efficiencies of 77% and 70%, respectively, at various polarization angles at the desired operating frequencies of 2.7 GHz and 3.4 GHz.

Acknowledgments

I would like to sincerely thanks my advisor Prof. Omar M. Ramahi for his continued support, guidance, encouragement, and great discussions which have made those Ph.D. years exciting, changing and transforming years of life.

Also, I would like to thanks all of my thesis committee members: Prof. Mo Mojahedi, Prof. Safieddin Safavi-Naeini, Prof. Karim S. Karim, and Prof. Sean Peterson for their insightful comments and encouragement.

Special thanks to all my family members: my parents, my brothers, and sisters for their spiritual supports throughout my academic gurney and my life in general.

I also like to truly appreciate and thank all my research group fellows for their stimulating discussions, support, help form one way or another, and all the great time we have had in the past years.

Finally, I would like to thank the Ministry of Education of Saudi Arabia for their generous financial support throughout my Ph.D. program.

Dedication

To my parents and siblings, my beloved wife Anssaf and my lovely daughters Zainab and Batool.

Table of Contents

List of Figures

Abbreviations

DR dielectric resonator iv, ix, xiii, 12, 13, 24–26, 32, 36–41, 43, 44, 46–48

DRA dielectric resonator antenna iv, viii, ix, xi–xiii, 12, 13, 23–38, 42–48, 98

DWM dielectric waveguide model 25, 43

EH energy harvesting 12, 13, 98, 99

EHS energy harvesting surface iv, v, viii, ix, xvi–xix, 4, 12–14, 16, 18, 49, 50, 62, 69–99, 101

SSP space solar power iv, xi, 4, 6, 7, 11, 12

WPT wireless power transfer iv, viii, xi, 1–9, 11–13, 15–17, 22, 69, 70, 99

Chapter 1

Introduction

With the current living standard and the high demands on energy, there have been increasing worldwide concerns on finding solutions that help to provide clean energy sources without harming the environment. Even with the governmental and research efforts that are continuously taken, the use of fossil-based power production to generate electricity is still dominating and is considered the highest economically favorable among all other possible alternatives. Traditionally, energy harvesting sources that are available in the environment include geothermal, solar, and vibrational. Such sources can be utilized as clean environmental friendly power sources [5]. However, there are common limitations being attached to those sources. Solar energy, for instance, has the highest power density on a sunny day, but also suffer from its large variability. Its power density varies from 100 uW/cm^3 to 100 mW/cm^3 [5] depending on the weather conditions, incident angles, etc. Vibrational energy harvesting which has been developed by S Roundy and P. K. Wright [6] for wireless electronics and then other work in harvesting human vibrational energy was reported in [7] in which the Piezoelectric materials convert the mechanical energy into electrical energy or vice versa. Vibration energy requires motion which makes its availability very limited and often not suitable for remote applications. On the venue of finding an alternative source of power, it is believed that wireless power transfer (WPT) technologies will support in providing, form one way or another, environmentally friendly solutions to such an energy issue.

1.1 Research Motivation

Wireless power transfer (WPT) is the fruit of combining the field of electromagnetic and the field radiowaves. The WPT transfer is considered as a future promising technology. WPT can be categorized into two broad categories: short distance and long distance WPTs. The difference between the WPT types strictly depends on the separation distance between the transmitter and the receiver with regards to their own fields surrounding the transmitter and receiver. If the separation distance between the transmitter and the receiver is within an electric distance where a strong near-field coupling occurs, then the system is considered as a near-field WPT, and the system is a far-field WPT if the electric separation (i.e. with respect to the operating wavelength) between the transmitter and the receiver is far from their own near-fields (i.e., several wavelengths separation) and where no coupling between those fields occur.

The short distance or what can be called near-field WPT technologies, such as inductive and capacitive coupling, are purely based on the electromagnetic theory where a transmitter and a receiver are coupled electromagnetically within their near-field region. The near-field WPT systems generally consist of two coils; i.e., a transmitter and a receiver, placed electrically close (i.e., with respect to the operating wavelength) to each other. Once the coupling occurs, the power is wirelessly transmitted via electric fields, magnetic fields, or through a combination of both. The efficiency of the transferred power between the coils is the ratio of the power delivered to a load on the secondary coil (receiver) to the power injected to excite the primary coil (transmitter). This efficiency is primarily dependent on the separation distance and alignment between the two coils [8, 9]. In the near-field powering, the harvester (receiver) is either inductively or capacitively coupled to a source (transmitter) and is small compared to the wavelength which makes it very sensitive to its relative position. This technology is based on non-radiating magnetic fields generated by resonating coils and hence called near-field powering.

At MIT (Massachusetts Institute of Technology), a near-field WPT experiment was demonstrated for continuously power a light bulb with 40% WPT efficiency at 2 m distance and they were able to continuously power a light bulb with wireless power [10]. The MIT experiments shown in Fig. 1.1 involved an inductive near-field coupling of power from a primary AC-excited coil to a secondary coil which is located 2 m away where a 60-W light bulb is attached and powered wirelessly. Although this demonstration seems very interesting, it is very limited to extremely short distances because the non-radiating magnetic near-field power density attenuates at a rate proportional to the inverse of the sixth power of distance [11]. In a practical manner, a magnetic resonance receiver coil that achieves 40% efficiency at 2 meters distance has to be enlarged to 244 times larger

Figure 1.1: MIT near-field WPT experimental demonstration [1].

in surface area to achieve the same 40% efficiency at 5 meters distance, which is neither practical nor compact. The near-field WPTs have variety of applications in charging portable electronics [12, 13, 14]. Also, charging electric vehicles is an application that can benefit from using the near-field WPT technology [15, 16].

The long-distance WPTs or what is called the far-field WPT systems, on the other hand, uses the theory of radiated electromagnetic waves and radiowaves. Unlike the near-field WPTs that can operate at very low frequencies, transmitting the electromagnetic power wirelessly for a long distance requires systems operating on the range of microwave frequencies allowing the traveling of electromagnetic waves. The far-field WPT system generally utilizes antennas as transmitters and receivers to radiate and collect electromagnetic power, respectively. In the far-field WPT systems, AC signal is firstly generated and then fed to a transmitter. The transmitted converts and transmits in a form of microwave power wirelessly from one point to another where then it gets converted back to a usable DC power through a component called rectenna. A rectenna system consisted of a receiving antenna and a rectifying circuitry, far from the transmitter, collects the microwave energy and then converts it to dc power. The rectenna plays a crucial rule in the WPTsystem as it is the element that should effectively capture the transmitted microwave power. The receiver collects the transmitted or the available microwave power and converts it to an AC signal. The AC signal gets rectified then by a rectifier circuitry converting the AC signal to usable DC power. Hence, a "rectenna" term is given to such a system as it combines the two words: rectifier and "antenna".

One promising application for the far-field WPT utilizing rectenna systems is to harvest energy from space as showing in Fig. 1.2. This concept was initially introduced by

Figure 1.2: Far-field SSP WPT concept [1].

Glasser [17, 18, 19] and called space solar power (SSP) where a large array of solar cells in space is used to collect solar energy and then converts it to microwave power for transmission using direct beaming antennas. Large rectenna arrays farms then receive the transmitted power and convert it into usable DC power.

Moreover, RF energy nowadays is broadcasted all around the world from billions of radio transmitters. These include but are not limited to mobile telephones and base stations, and television, radio broadcast stations, and the number of Wi-Fi routers and wireless devices are also another source of RF energy. One can detect more than ten Wi-Fi transmitters from a single location [20] in some urban environments. Thus, WPT and energy harvesting are technologies that can also be used to charge batteries in mobile phones, PCs, electric vehicles, and a host of other wireless devices.

Concerned by the huge power consumption demands that continue to increase over the years and being motivated in solving a worldwide energy issue by providing green energy solutions, the research presented in this thesis intends to target an energy-related issue in the field of microwave WPT. The study is to improve the harvesting efficiency of large rectenna arrays proposing different far-field energy harvesting surface's (EHS's) structures.

1.2 Literature Review

In 1831, Michael Faraday's empirical experiment shows the first work of transferring power wirelessly. Faraday inductively couples two coils to transfer energy from one coil to the other; i.e., what is called and known as Faraday's law. Since a strong mutual inductive coupling is required to efficiently exchange the energy between the coils, the two coils must be placed within a very limited short distance in which the transferring of energy degrades dramatically when the distance increases [21]. Towards the end of the 19th Century, Maxwell's mathematical model for predicting the existence of radiowaves [22] and Hertz's spark-gap experiment confirming their existence [23] were the actual beginning of WPT. Hertz's spark-gap experiment using parabolic reflectors at the transmitter and receive sides used a half-wavelength dipole spark gap to generate and transmit power at 500 MHz where he can detect this transmitted power at the receiver [23]. Hertz experimentally proves what Maxwell's equations has predicted by generating and transferring electromagnetic waves from one point to another [23, 2].

Nicola Tesla in the end years of the 19^{th} century and the early years of the 20^{th} century successfully demonstrated the concept of WPT conducting many projects and experiments [2, 24]. In 1898, Tesla used coils shown in Fig. 1.3 to generate power at 150 kHz to light 200 light bulbs placed at a distance of 26 miles away from the transmitting base station. Tesla's experiments on high power WPT continued until the year of 1910, but with limited success due to the limitations on the availability of high power energy sources to generate high-frequency signals [24].

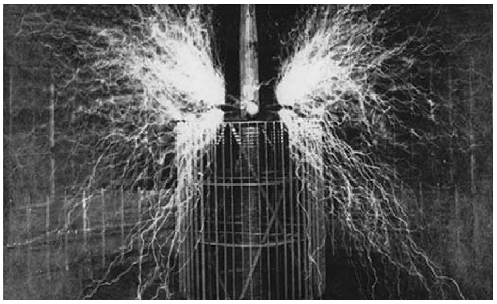

Figure 1.3: Tesla's coil used in his WPT experiment [1].

After Tesla's experiments, conducted research efforts were carried on both in Japan [25] and the U.S. [26] during the years of the 1920's and 1930's. The conducted studies were focused on the feasibility of the WPT technology. As a device did not exist that could transmit a narrow beam carrying large amount of electromagnetic power, both studies suggested and concluded that such a WPT technology is not feasible. In the late 1930s, the velocity-modulated beam tube (known as the Klystron tube) and the microwave cavity magnetron were invented [26]. These invented devices were able to generate high powered microwaves and solved the issues suggested by Japan and the U.S. research studies.

In the 1950's, the high power microwave tubes development had enabled an efficient device to generate power microwaves aiding the feasibility of the WPT technology. In 1960, the U.S. Department of Defense through Raytheon Company developed a 400 kW of continuous wave (CW) output power at 3 GHz with an overall DC-to-RF efficiency of 80% [27]. However, this development had not fully enabled the WPT technology due to a lack of any device that can convert the AC received power to DC [2]. Therefore, The U.S. Air Force conducted different studies through a number of companies to study the rectification of the AC microwave power and the fruit of those studies was the one done by Purdue University that investigate the use of semiconductor diodes as a rectifier [28, 29].

In 1960, Raytheon developed the first efficient receiving and rectifying device (i.e., rectenna) of microwave power. The developed rectenna consisted of a half-wave dipole antenna operating at 2.45 GHz with a single semiconductor diode placed above a reflecting plane where a resistive load terminating the output for the DC collected power. A thermionic diode was used to convert the received power to DC with a maximum conversion efficiency of 50% [30]. A more efficient conversion and power handling Schottky-barrier diode were developed by Hewlett-Packard to enable more efficient WPT systems [30, 31].

Motivations had started then following Raytheons great successes in demonstrating WPT systems. Following that, the U.S. Air Force showed an interest to wirelessly power an aircraft implementing the WPT technology. In 1964, William C. Brown at Raytheon built a far-field WPT system operating at the radio frequencies (RF) [2]. Brown's WPT system shown in Fig. 1.4 was built to power wirelessly a tethered helicopter [32], and it consisted of a DC source that fed a transmitting circuitry that generated an AC signal. The AC signal is then transmitted in space as an RF energy through a transmitting antenna [32].

Following Brown's demonstration, the Marshall Space Flight Center (MSFC) became interested in WPT to power satellites from a central space station [2]. Raytheon then in 1970 built a WPT system for MSFC with an overall DC-to-DC efficiency of 26%. Raytheon in a few years following this work demonstrated an improvement in the rectenna design using microwave beam launching methods shown in Fig.1.5 which resulted in a DC-to-DC conversion efficiency of 55% [1].

In 1968, Glasser [18] introduced the concept of SSP was introduced. The SSP concept showing in Fig. 1.6 consisted of a large array of solar cells in space that is used to collect solar energy and then get converted to microwave power for transmission using direct

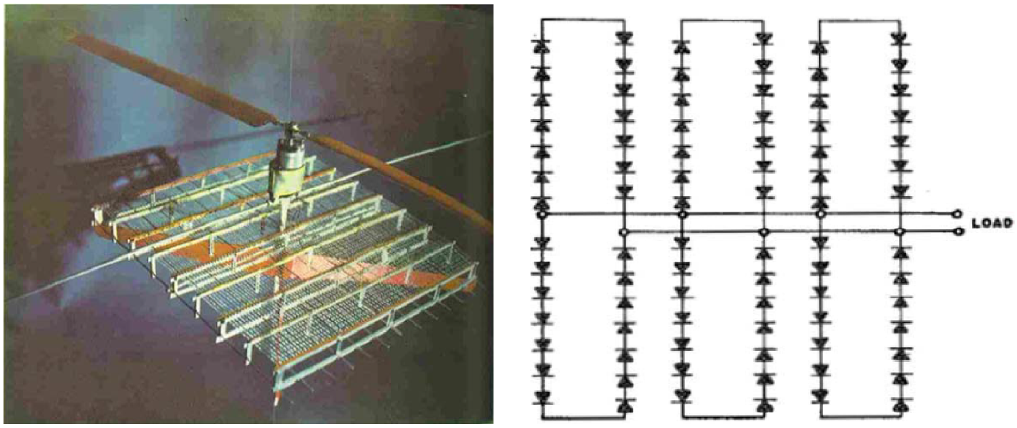

(a) (b)

Figure 1.4: (a) Brown's WPT helicopter rectenna by Raytheon Company [2]. (b) A schematic drawing showing the arrangement of the dipoles and rectifying diodes used in the helicopter rectenna [3].

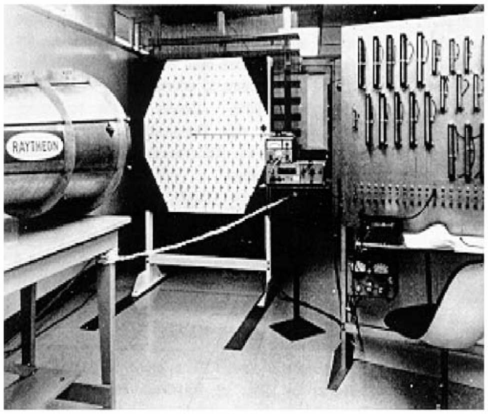

Figure 1.5: Raytheon WPT setup that resulted a DC-to-DC conversion efficiency of 55% [1].

beaming antennas [18, 19]. Large rectenna arrays farms then receive the transmitted power and convert it into usable DC power. NASA in 1973 started investigating the feasibility of SSPing contracted with four companies: Arthur D. Little, Raytheon, Grumman Aerospace, and Textron [33]. NASA's showed more interests then in WPTs supporting projects at both the Jet Propulsion Laboratory (JPL) and the Lewis Research Center (LeRC) [34, 35]. In 1975, an On-site far-field WPT experiment was conducted in the Mojave Desert at JPLs facility. A parabolic antenna operating at 2.4 GHz and fed by high powered klystron was used. The transmitted energy was received by 4590 dipole rectennas at a distance of one mile far from the transmitter with a DC output of 30 kW [34].

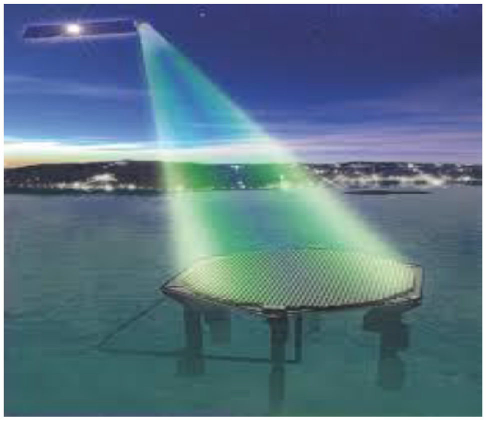

Figure 1.6: Large recenna farms on earth ground receiving the transmitted microwave power from the outer space [4].

Following the success of the Mojave Desert experiment, rectenna conversion efficiency continued to improve. Brown in 1977 achieved a rectification efficiency (i.e., AC to DC conversion) of 90.6% using GaAs Schottky diode and an aluminum bar dipole [36]. Also, a number of programs in Canada and Japan were specifically launched to build WPT's systems. In 1980, Canada built the Stationary High-Altitude Relay Program (SHARP) to wirelessly power an aircraft showing in Fig. 1.7 [37, 34, 38]. The SHARP aircraft were able to flow for 20 minutes at an altitude of 150 m powered wirelessly by a 10 kW ground parabolic dish antenna operating at 2.45 GHz.

Japan started their first WPT experiment in 1984 and launched their Microwave Ionosphere Nonlinear Interaction Experiment (MINIX) [39]. MINIX experiment focused on the effect of the ionospheric plasma when high-power microwave transmitted through it. Following this experiment, Japan also launched different WPT projects over the years of 1990's and are shown in Fig. 1.8 [40, 41, 42]. The Japanese International Space Year-Microwave Power Transmission in Space (ISY-METS) collaborated with Texas A&M University demonstrated the first WPT in space experiment between two rockets [42]. One rocket was responsible to transmit a power of 800 W to the other rocket at a frequency of 2.45 GHz that received the transmitted power by a dual-polarized rectenna (to the right in Fig. 1.8).

Recent developments in the WPT system were given towards improving various aspects

Figure 1.7: The Canadian wirelessly powered aircraft [1].

Figure 1.8: Japanese WPT experiments in the 1990s [1].

of rectenna systems which is also depending on the targeted applications. Different designs of single and small array Rectennas operating at dual or multiple frequency bands were introduced in the literature as an attempt to increase the amount of collected energy [43, 44, 45]. However, it remains a challenge to design a single rectifier that operates at the multiple frequency bands or a rectifying circuitry network that can cover multiple frequencies. In either case, a matching network is needed resulting in limited the bandwidth and degraded the rectifying efficiency. Other rectenna designs attempted to cover wider frequencies rather than operating at multiple bands [46, 47, 48, 49]. Channeling and rectifying the received energy still remain a challenge, and the same difficulty faced for the multiple bans is encountered for wideband rectennas. Two works presented by Popovic's group [50, 51] proposing the idea of directly matching the rectifying diodes at the same plane by mounting those diodes on antenna's feeds were no matching network getting an efficiency of 5 to 45%. The design was able to harvest at a wideband response, but with very low efficiency over the operating bands.

In the progress toward improving the efficiency of a rectenna array system, efforts were heavily focused to improve the AC to DC conversions [52, 50, 53, 54, 55, 56]. However, the efficiency of the main collectors was left untouched while relying on antenna theory analyses considering primarily metallic antennas such as patches, dipoles, microstrip patches, spiral antennas and other types [57, 58, 59, 60, 51, 61, 1, 5, 62, 63, 64, 45]. In this regards, therefore, various circuit topologies such as half-wave shunt/serious and voltage multipliers rectifiers were mostly presented for a rectenna system with single antenna element [61, 1]. The single rectenna element shows less complexity to integrate with different rectifier topologies compared to the array form rectennas. Unlike the single element rectennas that do not require any RF combining network for the received AC electromagnetic power, the array form rectennas normally require a combining network to combine the received AC power. Thus, most of the published works with single element rectennas have yielded higher harvesting efficiencies than the array form rectennas [61, 1]. An attempt to design a full-wave rectifier was presented in [56]. Even though this work presents an interesting way of achieving a full-wave rectification, the woke did not highlight the benefits of doing such a task. In fact, the loses will be increased as more rectifying elements are needed for the full-wave structure as compared to the half-wave one.

The harvested amount of power is very minimal when using single element rectennas (might be feasible for very low-power applications such as medical implants) [65, 60, 66, 58, 57, 45, 67]. To have sufficient amounts of harvested power, one needs to consider rectennas in an array form. The focus of the previous rectenna arrays based antennas were on the improving of the AC to DC efficiency with different receiving characteristics such as linear or circular polarizations [68, 69, 70, 71]. The achieved harvesting efficiency for the array rectennas are still lower than the single rectennas. The AC or DC channeling mechanisms, or both, still remains a challenge and difficult to achieve. Unlike the single element rectennas that do not require any RF combining network as only one feeding port is involved for the received electromagnetic AC power, the array form rectennas normally require a combining AC network or an extra matching network to combine the received AC power that gets rectified. Then, the rectified power can be smoothed by connecting a series inductor [65], shunt capacitor [59] and/or short and/or open stubs [72]. The DC rectified power then gets channeled to resistive load either in series, parallel or in both combinations [73, 74, 75].

In previous works considering rectenna arrays that are built based on antenna elements, none have considered looking at the array harvesting efficiency, in particular the array's capability to capture the incoming microwave energy and to convert it to AC power (i.e, the radiation to AC efficiency) [54, 70, 76]. Attempts to improve the main collector efficiency, namely the radiation to AC efficiency, considered using the concept of building mediums of electrically-small elements that are called metamaterial absorbers or metasurfaces for energy harvesting. The absorption concept of these electrically small collectors rely on matching the medium's impedance to the free-space impedance in which maximum energy is absorbed/harvested per footprint [77, 78, 79, 80, 81]. Despite the fact that these metamaterial/metasurface harvesters have yielded higher radiation to ac efficiencies, none have demonstrated complete rectenna systems by integrating a rectifying circuitry to show the radiation to DC conversion efficiency. One of the inherent disadvantages of using electrically-small elements structures as energy harvesters is that the received power density seen at each element is lower than what is required to turn-ON a rectifying diode. The low power density issue is faced when a direct matching mechanism is chosen between these electrically-small structure's element and a rectifying circuitry like the designs presented in [78] and [80]. These two works showed only designs with purely resistive impedance at each element that can be directly matched to a rectifying circuitry without integrating any rectifying circuitry, and not mention also here the difficulty that will also raise afterward for channeling the DC rectified power if a rectifying circuitry were successfully integrated.

To overcome such challenges in these electrically-small structures, a metasurface harvesting array presented in [82] integrates a layer of feeding network that channels the harvested ac energy into a single rectification circuit. The metasurface harvester in [82] was able to harvest the incoming energy with a radiation to DC efficiency of 40%. Another work presented in [83] introduces the concept of using super-cell metamaterial to build an energy harvester. In [83], the goal was to maximize the power density per super cell and was able to achieve a radiation to DC efficiency of 70% at multiple polarizations. Despite the fact that both works in [82] and [83] have attempted to solve the issue of having sufficient rectifying power density when using electrically-small elements as energy harvesters, they still required integrating additional layer that serves as a feeding network. Not only the loses are increased due to adding an additional layer, but also the designs became very complex due to the challenge of fabricating vias.

The reported applications that use the concept of WPT's technology vary. The WPT appears on applications such as radio-frequency identification (RFID's) [84], implantable biomedical devices [85], remote sensing [86, 87], to name a few. However, the application of WPT that currently drawing the most attention is SSP. The evidence of such a claim can be seen in the announcement made by the Japanese 2020 to 2030's plans. Their plans are to have an MW class SSP system in place in the 2020s and a commercial 1 GW class SSP system in place in the 2030s [88]. This stems from Japans desire for unlimited clean energy to replace its limited energy resources and reliance on foreign oil. With this SSP commitment and the numerous other WPT applications, rectennas have a bright and promising future.

1.3 Research Objectives

The two main figures of merit to evaluate a WPT rectenna system concluded from the above literature review are the radiation to AC efficiency and the radiation to DC efficiency. The latter combines the efficiencies of the electromagnetic energy collectors or antenna, and that of the rectifying circuitry. In the progress towards improving the efficiency of a rectenna array system, efforts were heavily focused on improving the AC version efficiencies, i.e. the rectifying circuitry. However, in most previous works, efforts to improve the efficiency of the antennas were not pursued. The majority of rectennas operating in the microwave were in fact designed using conventional antennas because of their wide use in modern communications technologies but not for their particular ability or suitability to efficiently harvest electromagnetic radiation.

The main objectives, therefore, of this research are summarized as follow:

1. **Define** a meaningful and practical definition to calculate the efficiency for energy harvesting (EH) and WPT structures.
2. **Introduce** the concept of using unconventional energy collectors based on appreciable electrically-large elements to build EHSs and WPT structures.
3. **Propose** the use of dielectric resonator antennas (DRAs) in an array form to efficiently build energy harvesters in the microwave regime considering the fabrication challenges of such antennas.
4. **Extend** the study in 3 to minimize the fabrication complexity by introducing a complementary design DRA investigating different dielectric resonator (DR) materials.
5. **Investigate** on the use of an electrically small DRA as an efficient harvester that can be directly integrated with rectifying circuity.

6. **Propose** various unconventional EHS's array structures that are consisted of appreciable electrically-large elements to increase the power density per array element and to maximize the turn-ON time for the rectifying diodes.
7. **Propose** direct rectifying and channeling mechanisms for the collected power for the EHS array structures to avoid the use of any matching networks or extra layers for channeling the power.
8. **Propose** different EHS structures that are capable of collecting the microwave energy at multiple polarizations.
9. **Propose** the concept of using multi-layering EHSs to operate the WPT and EH systems at multiple frequencies.

1.4 Thesis Outline

The remaining of this thesis is organized as follows:

Chapter 2, of this thesis gives an overview of the fundamental foundations and backgrounds for EH and WPT structures. The chapter also defines in details a meaningful way to calculate the harvesting AC and DC efficiency that is different than the classical efficiency calculation used in characterizing antennas.

Chapter 3 of the thesis introduces, for the first time, the use of DRA in an array form as an energy harvester. Simulation studies were performed to build foundation profiles for the use of DRAs in an array form as an energy harvester. The study considers the size of the ground plane and the coupling between DR elements effects on the AC efficiency of the antenna structure for different incident polarizations. Then the chapter extends to proposes a solution considering the DRA's fabrication challenges that are normally faced when fabricating DRAs. Thus, the chapter introduces a complementary DRAs structure consisted of dielectric resonator blocks and backed by cut grounds. The complementary DRA array is studied numerically showing that this proposed structure is not only solving the fabrication challenges but it can also efficiently deliver the incident power and convert it to AC power.

The concept of using electromagnetic EHS structure is introduced in **Chapter 4** of this thesis considering the challenges to rectify the received AC power. A design of an electromagnetic EHS inspired by an array of printed metallic dipolar elements is proposed. The unit cell of the EHS is based on two printed appreciable electrically large asymmetric off-center fed dipoles. An EHS array is then analyzed numerically and experimentally for maximizing radiation to AC absorption. After proving the AC absorption capability of the asymmetrical dipolar structure, a channeling mechanism is proposed to rectify the absorbed AC power and converted to DC. The rectifying circuitry is integrated at the elements plan of the EHS structure providing direct and efficient rectifying mechanize. The chapter concludes by showing experimentally the overall radiation to DC harvesting efficiency for an EHS array. Then the chapter extends presenting a design for a multi-polarization electromagnetic EHS inspired by the printed asymmetrical metallic dipolar elements. The harvesting array features two layers that collectively capture the incident energy from various incident angles. The multilayer asymmetrical metallic dipolar EHS experimentally yields an efficient overall radiation to DC harvesting efficiency for multiple incident polarizations.

Chapter 5 introduces then the concept of multiple polarizations EHS while only using one metallization layer. Two cross-dipole unit cell that enables capturing the energy from various angles of illuminations are used as EHS. A critical design feature of the proposed cross-dipole EHS is that it allows direct matching to a rectifying circuitry at the dipoles plane. A cross-dipole EHS array is built and validated experimentally for an overall radiation to DC harvesting efficiency at various polarization angles. The thesis concludes by introducing in **Chapter 5** the concept of stacking multilayer EHS's for an efficient harvesting at dual-band or multiple bands frequencies. A unit cell of two stacked-layer of cross-dipole elements for operating at two frequency bands for multiple polarizations is proposed. The proposed EHS array introduces the concept of stacked surfaces that can be directly integrated with the rectification circuitry. The DC channeling was achieved for the multi-layer EHS structure such that it is collected at the elements' plane for each layer where the total achieved harvested DC power is the collective contribution of the rectified DC power from the EHS layers. A finite multi-layer array of 7×7 unit cells was fabricated and tested experimentally.

The main contributions and outcomes of the thesis are summarized in **Chapter 6** followed by suggestions for future research work.

Chapter 2

Far-Field Wireless Power Transfer

2.1 Introduction

WPT is a system build based on an interaction between electromagnetic waves and the response of the materials creating an electromagnetic phenomenon. Maxwell's four equations and the constitutive equations shown below govern all electromagnetic phenomenon. These equations are used to describe WPT systems in a fundamentally similar way when treating and describing a phenomenon on the field of wireless communication.

$$\nabla \times E = -\frac{\partial B}{\partial t} \tag{2.1}$$

$$\nabla \times H = J + \frac{\partial D}{\partial t} \tag{2.2}$$

$$\nabla . D = \rho \tag{2.3}$$

$$\nabla . B = 0 \tag{2.4}$$

where the constitutive equations are as follows: $B = \mu H$, $D = \varepsilon E$, and $J = \sigma E$.

The fundamental difference between the WPT and communication systems, however, is the definition of the system's efficiency on each system. The WPT systems rely on the efficiency of the system's elements such as the signal generator and the amplifier. Also, it depends on the ability of the transmitter's beam to efficiently transmit and focus the electromagnetic waves on a targeted rectenna. Additionally, the efficiency of the rectenna has a major effect on the overall efficiency of a WPT system as it is the element that captures the transmitted signal and converts it into usable DC power. On the other hand, a wireless communication system's efficiency is normally based on a specific noise level and bandwidth as the microwave is simply used to carry on information where the gain of both the transmitter and receiver, the noise figure and other antenna and communication parameters are considered to determine the efficiency of such a communication system.

As the focus in this thesis is on the rectenna side of the far-field WPT system where the distance between the transmitter and the receiver is multiple of wavelengths, theoretical background on the WPT system and the rectennas element. Also, this chapter will address and define the harvesting efficiency used in the thesis to evaluate the proposed EHS structures.

2.2 WPT system

A far-field WPT system shown in Fig. 2.1 consists of three main subsystems: a transmitter, a medium for the traveling/transmitting waves and a receiver or what is called a "rectenna". The first element represents the transmitting antenna that is responsible to convert the DC/AC source power to microwave and radiate it with an efficiency η_t. The middle element shown in Fig. 2.1 represents the medium that electromagnetic waves are traveling/propagating in and it is the free space in our case. The efficiency of the waves propagating from the transmitter to receiver η_s which is the ratio of received power to transmitted power at each side plane. The third element to the left of Fig. 2.1 is the rectenna that captures the radiated wave traveling from a transmitter and converts it to AC power in which this power then converted to DC using rectifying circuitry. The efficiency of the rectenna/receiver system is given as η_r.

The transmitted power density is very critical for efficient wave transmission. A work by Goubau and Schwering showed that microwave power transmission can approach 100% if the transmitting aperture is illuminated properly [89, 90]. The transmitting efficiency which is a function of the parameter τ [90] is given by

$$\tau = \frac{\sqrt{A_r\ A_t}}{\lambda D} \tag{2.5}$$

where A_r and A_t are the aperture areas of the receiver and transmitter respectively, λ is

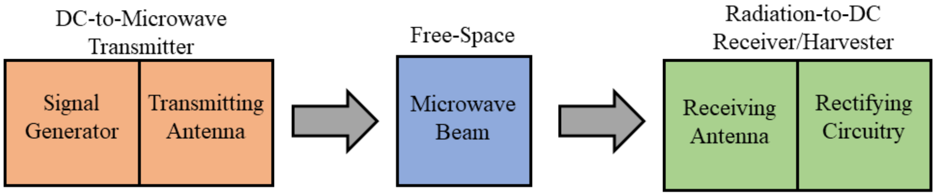

Figure 2.1: A diagram showing the main elements of a WPT system.

the wavelength of the transmitted wave, and D is the distance between the transmitter and receiver and thus the beam efficiency η_t is given by

$$\eta = (1 - e^{-\tau^2}) \times \ 100\ \% \tag{2.6}$$

The above equation suggests that larger values of τ will yield a higher efficiency which is directly related to the aperture areas of both the transmitter and receiver.

The shown block diagram in Fig. 2.2 presents the basic and classical components of a rectenna which normally used when considering a single antenna that includes a receiving antenna or an energy harvester, a harmonic rejection filter, a diode, a DC-pass filter (capacitor), and a resistive load to collect DC power.

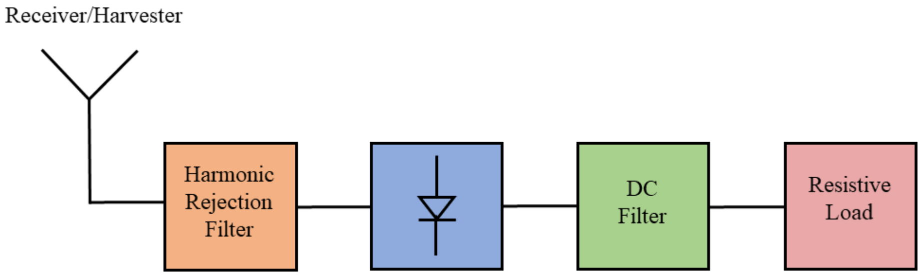

Figure 2.2: A diagram showing the elements of a rectenna system.

The classical conversion efficiency of the rectenna is calculated as

$$\eta = \frac{P_{DC}}{P_{received}} \times \ 100\ \% \tag{2.7}$$

where P_{DC} is the measured output power across the load at DC and Preceived is the RF power received by the rectennas antenna. $P_{received}$ can be calculated using the Friis transmission equation [91] by

$$P_{received} = P_t G_t G_r \left(\lambda_o / 4\pi r\right)^2 = A_{apr} \frac{P_t G_t}{4\pi r^2} \tag{2.8}$$

where the effective area of the receiving antenna is

$$A_{apr} = \frac{G_r \lambda_o^2}{4\pi} \tag{2.9}$$

P_t is the transmitted power, G_t and G_r are the transmitting and receiving antenna gains respectively, λ_o is the free space wavelength, and r is the distance between the transmitter and the rectenna. Rectenna efficiency is given as a function of received power density S_D. The power density S_D be expressed as

$$S_D = \frac{P_{received}}{A_{apr}} = \frac{P_t G_t}{4\pi r^2} \tag{2.10}$$

Therefore, the overall efficiency $\eta_{overall\ efficiency}$ of the wireless power transmission system is the ratio of DC output power at the rectenna to the DC (or AC) input power given at the transmitter side which is given by

$$\eta_{\ overall\ efficiency} = \eta_t \ \times \ \eta_s \ \times \ \eta_r \tag{2.11}$$

2.3 Efficiency Calculation of the EHS's

The energy harvesting efficiency in this thesis is defined based on the footprint area of the structure. Following [92], this definition measure how efficient the harvester is in converting the available incident microwave power, P_{in}, to an average AC power, P_{out}. The available power P_{in} is dependent on the footprint (real estate) occupied by the harvester. Thus, the overall efficiency of the harvester $\eta_{ch2/eff}$ was defined as the ratio of the total time average power P_{out} to the available microwave power P_{in} available at the harvester footprint area and dependent only on the incident plane wave, its propagation direction, and polarization.

The radiation to AC/DC absorption efficiency describes the ability of an absorber to capture the energy per footprint area [77]. What is referred to in this work as a radiation to AC efficiency is the efficiency of the harvester to transfer the total power incident on a specific area to available power at the feed (i.e., efficiently absorb and channel the illuminated electromagnetic power to a resistive load or multiple loads where a rectifying circuitry is placed for the AC to DC conversion). The radiation to AC conversion efficiency is calculated by calculating the footprint (surface area) in square meters. The Radiation to AC conversion efficiency of an energy harvester occupying a specific footprint is then described as

$$\eta_{Rad-AC} = P_{out}/P_{in} \tag{2.12}$$

where P_{in} is the total time-averaged power incident on the footprint, and P_{out} is the available time-average AC power received by the harvesters' collectors (i.e., where a resistive load or a diode rectifying circuity is placed) and is given by

$$P_{out} = \sum_{n=1}^{N} V_i^2/R_i \tag{2.13}$$

where V_i is the voltage across the resistance of the i^{th} collector (R_i) and N is the total number of collectors.

This Radiation to AC efficiency definition is indicative of the ability of the harvester to utilize the available electromagnetic energy incident on a given area and the ability of the harvester or its collectors to deliver the absorbed energy to resistive loads. This definition provides a measure of how efficient the absorber, occupying a specific footprint, is in converting the available incident microwave power to AC energy.

For energy harvesting applications, the physical area definition is of importance as it is linked to the real estate in a manner similar to placing solar cells over a specific well-defined footprint. Thus, efficiency appreciably higher than 100% can be obtained based on this definition. This is due to the fact that the structure can receive power larger than its physical area. This is easier to see if one recalls that the effective aperture for some small antennas can easily exceed its physical area.

In this thesis, the efficiency definition is used in two forms: the radiation to AC which represents the efficiency of the harvester before the rectifying is taken place, and the radiation to DC conversion efficiencies that accounts for rectification efficiency.

2.4 Background Operation of a Rectenna

The basic rectenna rectifying circuit is based on a half-wave rectifier with a capacitor added in shunt. It is therefore important to understand the operation of a half- wave rectifier so that the rectennas operation can be understood. An explanation of a half-wave rectifier can be found in many publications(refer to these two reference for more details [93, 61]) and rectenna operation theory is discussed in details in these works [94, 95, 93, 61]. A brief summary will be present here for a half-wave rectifier and its voltage waveforms showing in Fig. 2.3.

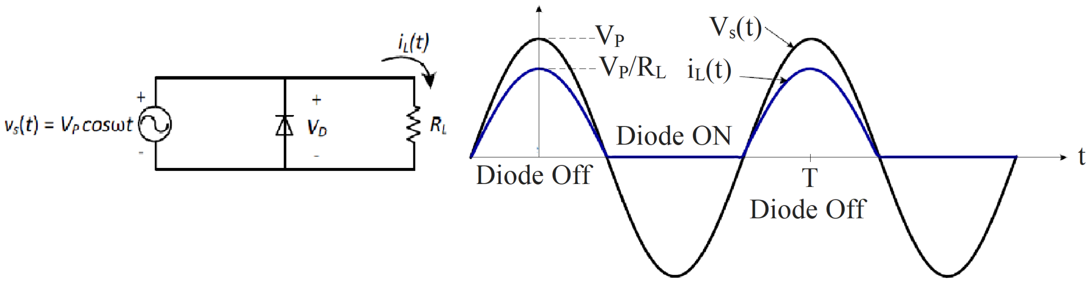

Figure 2.3: Circuit and voltage waveforms of a half-wave rectifier.

Assuming an ideal diode and a perfect input sinusoid v_s, during the positive half-cycle where ($v_s \geq 0$) in which the diode is short circuited (as shown in waveform cycle illustrated in Fig. 2.3). This will cause all of the current to flow through the resistive load R_L. Whereas, the diode is open circuited during the negative half-cycle (as shown in the waveform in Fig. 2.3) where ($v_s \leq 0$). In this case, the current will flow through the diode and bypassing the resistive load which makes the current to flow through the resistive load R_L with unidirectional behavior and have a finite averaged value of a DC component. This explanation is simply the rectification of the source current that can be used to convert the received AC signal to usable DC power. Thus, the averaged rectified DC current $I_L(DC)$ can be expressed as

$$I_{L,DC} = \frac{1}{T}\int_T i_L(t)\ dt = \frac{1}{T}\left(\int_{-T/4}^{-T/4} \frac{V_p}{R_L}\ cos\ \omega t\ dt\right) \tag{2.14}$$

where T is the period of the incident sinusoid and $\omega = 2\pi/T$. By solving the above integral, the averaged DC current is then given by

$$I_{L,DC} = \frac{V_p}{\pi R_L} \tag{2.15}$$

The averaged r.m.s. DC voltage across the load than can be found. If a capacitor is added in shunt as a DC-pass filter to the above half-wave rectifier circuit, the waveforms behavior seen in Fig. 2.4 will result where the voltage across the load is given by

$$v_L(t) = V_p e^{-t/R_L C} \tag{2.16}$$

where $R_L C$ is the time constant and t is the time measured from the peak of the waveform where $v_L(t) \neq V_p$. The exponential decrease in the load voltage can be approximated by a straight line since the period is very short compared to the time constant at microwave frequencies.

Using the straight line approximation for the exponential decay where the linear terms are kept while the rest are discarded. The minimum value of v_L is at t = T is then given as

$$V_{min} = v_L(t = T) \approx V_p\left(1 - \frac{T}{R_L C}\right) = V_p\left(1 - \frac{1}{f R_L C}\right) \tag{2.17}$$

Once the voltage $v_L(t)$ decreases to V_{min}, the diode will be non-conducting and the source voltage will be rising above V_{min} which will again raise the load voltage v_L to its peak value of V_P. The average r.m.s. DC voltage across the resistive load, considering the peak-to-peak ripple voltage of V_L, is give by

$$V_{L,DC} = \frac{V_{max} + V_{min}}{2} = Vp\left(1 - \frac{1}{2 f R_L C}\right) \approx V_p \tag{2.18}$$

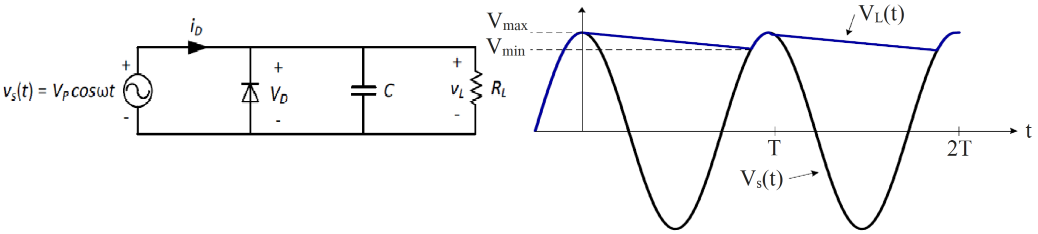

Figure 2.4: Circuit and waveforms of a Half-wave rectifier waveforms with a capacitor added to the circuit.

2.4.1 Effect of Input Power on Rectenna Efficiency

The magnitude of the input power or the power density seeing at the rectenna's feeds has a major effect on the rectifying circuitry conversion efficiency. The diode conversion efficiency rises to a certain peak point and then starts to fall down and decrease respectively with the increase of the input power [96]. The conversion efficiency is expected to be very low at low input power (low power density) levels as the diode voltage will be still below or just approaching the turn-on voltage V_{bi}. In other words, the diode is in a state in which it not fully turned-ON. As the power level increased; i.e., the density level seen by the rectenna and channeled to the diode, the diode voltage exceeds the turn-ON voltage at which the conversion efficiency increases.

2.5 Conclusion

This chapter has presented the fundamental basics of WPT systems. It also shows theoretically how the rectification circuity works. More importantly, the chapter describes the radiation to DC efficiency implemented in this thesis and how it differs from the efficiency calculation normally used in classical antenna theory.

Chapter 3

DRA for Energy Harvesting

3.1 Introduction

Several researchers have studied energy harvesting from electromagnetic waves to provide power to broad range of low-power devices using primarily metallic antennas such as microstrip patches, spiral antennas and metamaterial cells [97, 98, 99, 100, 101, 102, 92, 103, 104]. Apart from severe metallic losses or low radiation efficiencies when operating in high frequencies, it was found that metallic antennas generally offer narrow impedance bandwidths [105]. On the other hand, DRA, which are considered as non-metallic antennas [106], offer some advantages when compared to metallic antennas [101]. Particularly, DRAs provide high radiation efficiency, wide bandwidth and compact size in the microwave frequency range [105, 106, 107].

The resonant frequency of DRA is a function of size, shape and dielectric permittivity [108]. The impedance bandwidth for DRAs is a function of the dielectric permittivity and aspect ratio (length-to-height)[107]. Thus, for a given dielectric permittivity (ε_r), the aspect ratio can be adjusted to provide compact low profile antenna or a wide-bandwidth. The dimensional degrees of freedom are considered when comparing different geometries of the DRAs (in fact, a proper choice may depend upon the desired bandwidth, directivity or volume [108, 106]). The DRA can tolerate relatively high temperatures (in comparison to metallic antennas), thus, its resonant frequency remains stable with temperature fluctuation [109]. This advantage makes DRAs highly suitable for applications in harsh environments such as military applications [109] and remotely powered sensors in uncontrolled environments [110]. DRAs can be designed in smaller size than conventional metallic antennas ($1/\sqrt{\varepsilon_r}$). Using high permittivity constant for compact designs, DRAs offer wider bandwidth compared to microstrip antennas [108, 101].

Good energy absorption call for minimal Ohmic and dielectric losses such that the power absorbed is maximized [97]. The work in [101] showed that DRAs have negligible losses and thus offer higher radiation efficiency in the microwave regime when compared to microstrip patch antennas. DRAs offer compatibility with existing feeding techniques which make them easy to fabricate using current circuit and microwave printed technology [106, 111]. The design in [112] of a rectangular DRA fed by a metallic waveguide showed the ability of low-temperature co-fired ceramic technology to integrate dielectric and metal layers in a single process. Such techniques can be employed to design DRAs and to integrate them in highly compact packages.

This chapter focuses on using DRAs for energy harvesting in the microwave regime. The emphases will be on the ability of DRA, as a single antenna and in array arrangement, to efficiently harvest the microwave energy and convert it into a usable AC power. The AC power can be converted into DC using classical rectification circuitry. The emphasize of this chapter is on the conversion from radiation to AC where the rectification to convert the AC power to DC and the DC channeling are not the subjects of this chapter.

3.2 Rectangular DRA for Energy Harvesting

DRAs can be designed in a variety of shapes. Basic DR shapes are generally used due to their ease of analysis and simple fabrication [100]. In this section, a rectangular DR was chosen as it offers advantages over the hemispherical and cylindrical geometries [106, 113]. Hemispherical and cylindrical DRAs offer no degree and one degree of freedom, respectively. On the other hand, rectangular DRs have two degrees of freedom, also referred to as the aspect ratios (height/length and width/length). Because of these two aspect ratios, designers have flexibility in selecting the proper ratio to suit the needs of the intended application. These degrees of freedom offer design choices when controlling the antenna bandwidth, operating frequency, and excitation mechanisms [108, 106]. The DRA specifications were determined such that the antenna resonates at 5.5GHz. This frequency was chosen partially based on the material availability. In particular, this section highlights the importance of mutual coupling between adjacent elements on the harvested power efficiency. Experiments are also presented to validate the numerical simulation [114].

3.2.1 Proof of Concept

The following approach was taken to design single rectangular DRA. Initially, two material constraints were imposed, the DR height (b = 6.35mm) and dielectric constant (ε_r = 9.8). Then the DR dimensions (see Fig. 3.1) were calculated by employing the dielectric waveguide model (DWM) formula for a rectangular dielectric resonator [113]. The DWM was used to solve for the desired resonant frequency as follows:

$$k_x \ tan(k_x a/2) = \sqrt{(\varepsilon_r - 1)k_{mn}^2 - k_x} \tag{3.1}$$

Where:

$$\begin{gathered} k_{mn} = 2\pi f_{mn}/v \\ k_y = \frac{m\pi}{c} \quad k_z = \frac{n\pi}{2b} \\ k_x^2 + k_y^2 + k_z^2 = \varepsilon_r k_{mn}^2 \end{gathered} \tag{3.2}$$

In Eq. 3.1 and 3.2, m and n are positive integers corresponding to the field variation in the y and z directions, respectively, and f_{mn} is the resonant frequency of the (m, n) mode. v is the speed of light in free space and ε_r is the dielectric constant of the resonator. a, b, and c are the dimensions of the DR.

The DWM set of equations can be used to determine the dimensional parameters of the resonator for a desired frequency of operation when constraining some of the parameters. Based on the solutions of Eqs. 3.1 and 3.2, different possible rectangular DR dimensions can be obtained that satisfy the desired resonant frequency. Thus, by using the above DWM set of equations solving for the lowest TE modes and constraining the height to $b = 6.35$mm and permittivity to $\varepsilon_r = 9.8$, a single DRA was designed to operate at 5.5GHz and then simulated using ANSYS HFSS [115]. After minor optimization to achieve resonance at 5.5GHz, the dimensions of the DR were found to be a = 16.5mm and c = 11.4mm. The DR was centered on a ground plane with W' and $= L'$ and $= \lambda/5$ as shown in Fig. 3.1. It is noted that the values for W' and L' were the result of optimization such that the ground plane was minimized while maximizing the DRA return loss and radiation efficiency. This setup gave a ground plane size of width $W = 38$mm and length $L = 33$mm. An HRM(V)-306S SMA type 50Ω probe feeder was used with outer radius of 2.05mm and inner conductor radius of 0.64mm (these values were taken from the specifications sheet). The inner conductor of the probe that connects to the body of the DR has a length of $h = 5.37 \ mm$ and was positioned at $c/2$ on $y\text{–}axis$ and at $s = 2.4$mm on $x\text{–}axis$ as shown in Fig. 3.1. The resulting simulated Return Loss (RL) and simulated input impedance of the DRA are shown in Figs. 3.2(a) and 3.2(b).

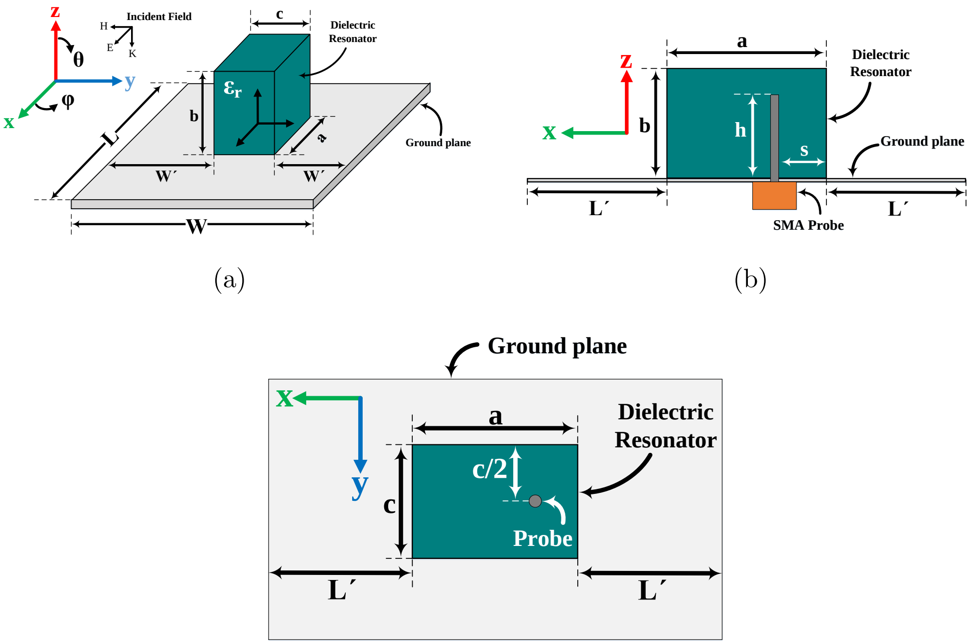

(a) (b)

(c)

Figure 3.1: Schematic showing a single DRA placed on a conducting ground plane fed by an SMA probe: (a) Perspective view black, (b) Side view and (c) Top view showing the probe location.

Since the efficiency of the harvester was defined based on its physical footprint, including any ground plane, it is expected that the size of the ground plane will change the harvesting efficiency levels. The ground plane size was defined by placing the DR at the middle of a ground plane and varying W' and L' proportionally to the DRA free-space wavelength of $\lambda = 54.5$mm in the particular case considered (see Fig. 3.1). Variations in W' and L' were taken from 0 to $\lambda/2$. For instance, having $W' = L' = \lambda/2$ gave a ground plane size of $W = 71.1$mm and $L = 66$mm, where a $W' = L' = 0$ gave a ground size of ($W = 16.5$mm and $L = 11.4$mm).

To calculate the harvesting efficiency of the single DRA, the structure was simulated with normal incidence ($\theta = 0$ and $\phi = 0$) plane waves for different ground plane sizes. The resulting power efficiency for various ground plane sizes are shown in Fig. 3.3(a). In Fig. 3.3(b), the ground plane size is fixed at $W' = L' = \lambda/5$ (corresponding to $W = 38.3$mm and $L = 33.5$mm) and show the efficiency for three different incident angles $\theta = 0$, $\theta = 30$,

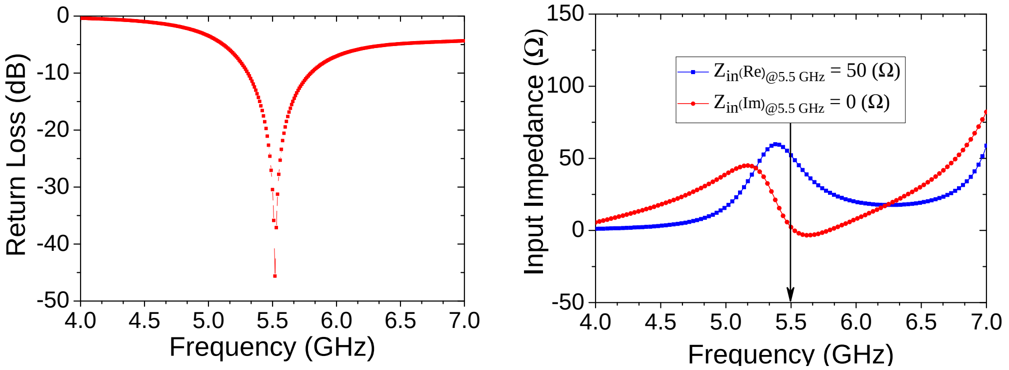

(a) (b)

Figure 3.2: (a) Simulated return loss (S_{11}) of the single rectangular DRA. (b) Simulated input impedance of the single rectangular DRA: real and imaginary parts.

and $\theta = 60$ where $\phi = 0$. It is observed that the smaller the ground plane, the higher the efficiency. This conclusion, although not intuitive, does not necessarily imply that the smaller the ground plane, the higher the power absorbed by the DRA. It need to be kept in mind that the efficiency definition is based on the total footprint of the entire antenna structure.

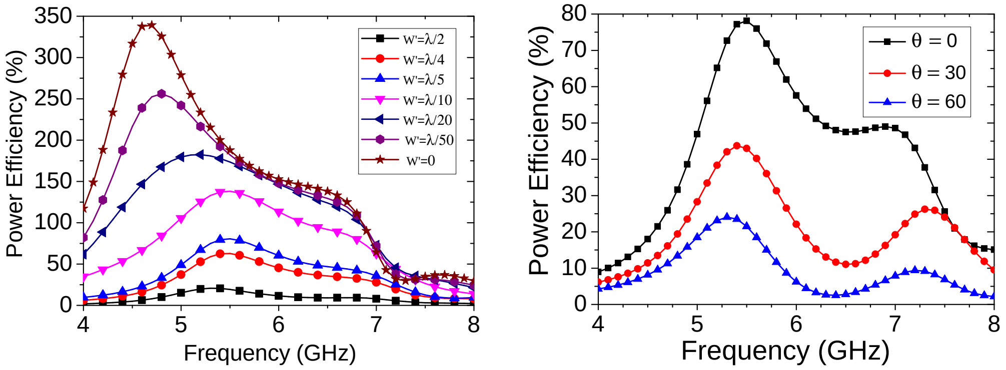

(a) (b)

Figure 3.3: (a) The effect of the single DRA ground plane size on the simulated power efficiency with a normally incident illumination $\theta = 0$ *and* $\phi = 0$ ($W' = L'$; see Fig. 3.1). (b) Simulated power efficiency of a single DRA with ground size spacing of $\lambda/5$ for three different incident illuminations $\theta = 0$, $\theta = 30$, and $\theta = 60$ where $\phi = 0$.

Next, a one-dimensional 1×3 DRA array shown in Fig 3.4(a) is considered. Arrays are typically used to improve the antenna gain and directivity [91]. Spacing between array elements introduces mutual coupling that affects the radiation property of each array element. In most antenna communication applications where gain enhancement is the goal, an inter-element spacing of $\lambda/2$ between array elements is generally used to provide, not full, but sufficient isolation between adjacent antennas [116]. The 1×3 DRA array was designed using the dimensions used above for the single rectangular DRA. In particular, the focus is given to the effect of mutual coupling and size of ground plane on the efficiency.

The power harvesting efficiency of the array elements were studied for different ground plane sizes and for different inter-element spacing d while setting $W' = L' = d$ (see Fig. 3.4(a)). Each element was fed by a 50Ω coaxial probe. First, the scattering parameters of the array middle element (S_{11}, S_{12}, and S_{13}) were simulated to show the impact of mutual coupling. Fig. 3.4(b) shows the scattering parameters for different inter-element spacings. Because of symmetry, only S_{11} and S_{12} are shown in Fig. 3.4(b). Amongst the cases considered, the $\lambda/2$ inter-element spacing gave the least mutual coupling.

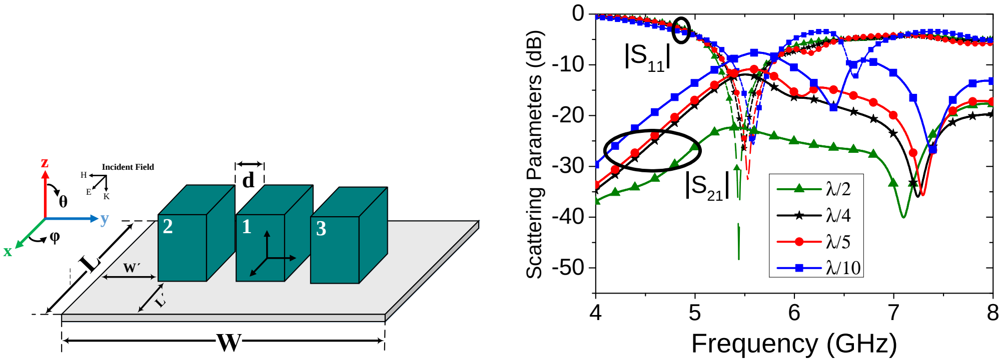

(a) (b)

Figure 3.4: (a) Schematic showing a DRA array of 1×3 unites placed on a conducting ground plane with an inter-element spacing d between each against element. (b) Simulated 1×3 DRA array scattering parameters S_{11} and S_{21} for different inter-element spacings d.

The array then was illuminated by a normal incident plane wave for. Lumped impedances of 50Ω were placed at all ports to simulate the received power from each array element. The total available power received by the three elements is given by

$$P_{out} = \sum_{n=1}^{N} p_{out}^{(n)} \tag{3.3}$$

where N is the number of elements in the array and $p_{out}^{(n)}$ is the received power from each array element.

Two investigations were considered to study factors that may affect the harvesting efficiency for the array. First, a fixed ground plane size of $W = 2.6\lambda$ and $L = 1.3\lambda$ was used while the inter-element spacing d was varied proportionally to the free-space wavelength $\lambda = 54.5$mm from 0 to $\lambda/2$. The simulation results are shown in Fig. 3.5(a). Here, our interest lies mainly in the effect of the elements coupling on the efficiency.

The second investigation was to study the effects of varying both the inter-element spacing d between array element and the ground plane size on efficiency. The variation of the ground plane size was defined similarly to the above study for the single DRA ground by centering the middle element and varying $W' = L'$ proportionally to the DRA free-space wavelength $\lambda = 54.5$mm (refer to Fig. 3.4(a)). Variations of the ground plane sizes and the inter-element spacing d between element were taken simultaneously from 0 to $\lambda/2$. For instance, $W' = L' = d = \lambda/4$ gave a ground plane size of $W = 88.8$mm and $L = 43.8$mm. The simulated power efficiency of the 1×3 DRA array having different ground plane sizes and inter-element spacings between elements is shown in Fig. 3.5(b). It is observed that both Fig. 3.5(a) and Fig. 3.5(b) have identical plots for the case of $\lambda/2$ inter-element spacing, when the maximum power efficiency reaches approximately 25%.

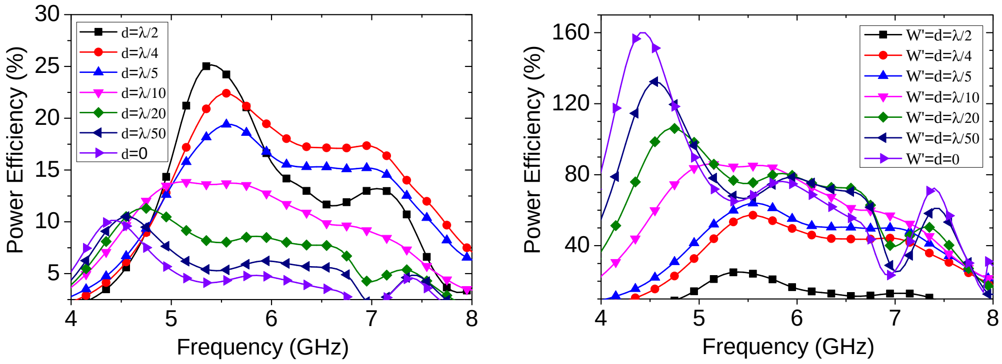

(a) (b)

Figure 3.5: Normal incidence ($\theta = 0$ and $\phi = 0$) simulated power efficiency of the 1×3 array illuminated by a plane wave for (a) a fixed ground plane size of $W \times L = 2.6\lambda \times 1.3\lambda$ and different inter-element spacings $d = \lambda/2$, $\lambda/4$, $\lambda/5$ and $\lambda/10$ (see Fig. 3.4(a)) and (b) for different ground plane sizes and inter-element spacings between elements $W' = d = \lambda/2$, $\lambda/4$, $\lambda/5$, $\lambda/10$, $\lambda/20$, $\lambda/50$, and 0 (refer to Fig. 3.4(a) to see array dimension.)

Different incident angles on the array were then simulated for the case of $W' = L' = d = \lambda/5$. Fig. 3.6 compares the 1×3 DRA array power efficiency for three different incident angles $\theta = 0$, $\theta = 15$, and $\theta = 30$ where $\phi = 0$.

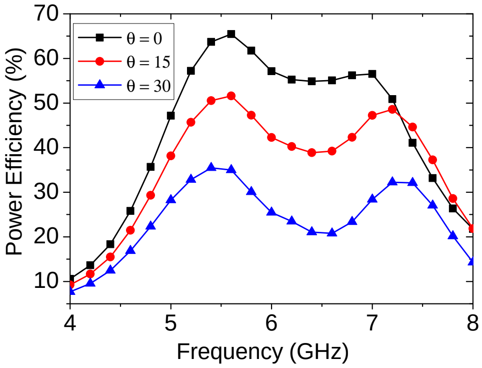

Figure 3.6: Simulated power efficiency of a 1×3 array illuminated by a plane wave for three different incident illuminations $\theta = 0$, $\theta = 15$, and $\theta = 30$ where $\phi = 0$ for ground plane size and inter-element spacing of $\lambda/5$.

Here, a calculation for the harvesting efficiency using the aperture efficiency is shown for only one case of the above 1×3 array study. The aperture efficiency can be defined as follows:

$$Aperture\ efficincy = \frac{maximum\ effective\ area}{physical\ area} \tag{3.4}$$

Referring to Fig. 3.5(b) and when the inter-element spacing between element and the ground size were of $\lambda/50$, the harvesting efficiency was around 140% at 4.5 GHz. This obtained efficiency was based on the physical area of the array. To find the corresponding efficiency considering the effective aperture for the case of $\lambda/50$ of the 1×3 array, the maximum directivity D_{max} was calculated. The maximum directivity D_{max} was found to be of 5 dB at the frequency of the maximum harvesting efficient (4.5 GHz) . Therefore, the erture of this structure was calculated to be of 1768.4 mm^2 where its physical area was of 708.75 mm^2. As a result, the aperture efficiency using eq. 3.4 is 249%. This results of having the effective aperture area is larger than the physical area explains the reason of having harvesting efficiencies higher that 100%.

3.2.2 Study of 5×5 Rectangular DRA array

The purpose of the above study was to obtain preliminary results as to what factors have an effect on the DRA harvesting efficiency when used as a single element or in array configuration. Next, the case of a two dimensional 5×5 array was considered where the study will be based on numerical simulation as well as experiments.

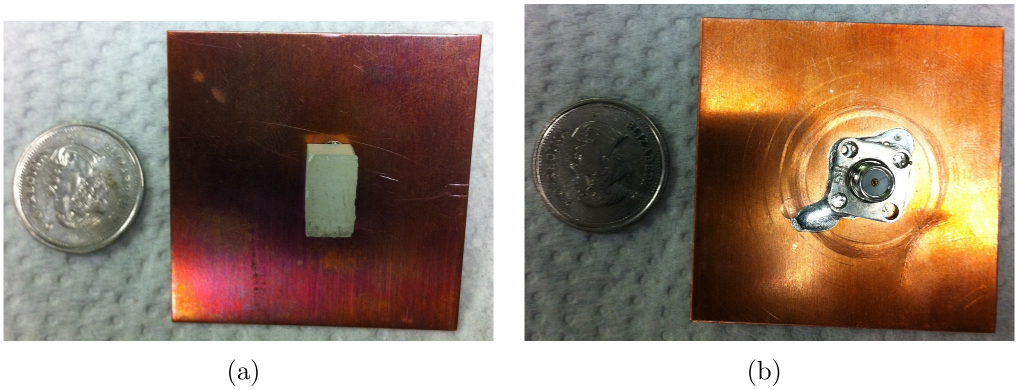
(a) (b)

Figure 3.7: Fabricated single DRA fed by a SMA coaxial probe: (a) Top view and (b) Bottom view.

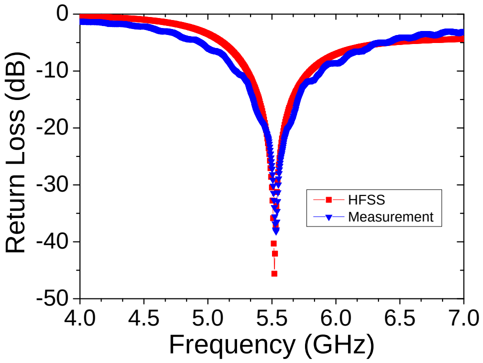

Figure 3.8: Simulation and measurement return loss (S_{11}) of the single rectangular DRA.

The above study of the single DRA element and 1×3 array built foundation bases to determine positions of the coaxial probe and inter-element spacings. The following design specifications were then taken to simulate and build the 5×5 DRA array. Probes were positioned at $c/2$ on y–$axis$ and at $s = 2.4$mm x–$axis$ (refer to Fig. 3.1 for probe position). DR dimensions were of $a = 16.5$mm, $b = 6.35$mm, and $c = 11.4$mm. Rogers TMM10i material was used as DRs. The inter-element spacing between adjacent elements (d) and the ground plane size ($W' = L'$) were chosen to be of $\lambda/5$. This made an array of a ground plane size of $W = 122.6$mm, $L = 148$mm and inter-element spacing d of 10.9mm (refer to Fig. 3.1 and Fig. 3.4(a) for probe position and array geometry). Holes of 0.64mm radius (SMA inner conductor) were drilled in all DRs. Each DR was terminated with an SMA having 50Ω input impedance. The top and bottom face of the fabricated 5×5 DRA array is shown in Fig. 3.9.

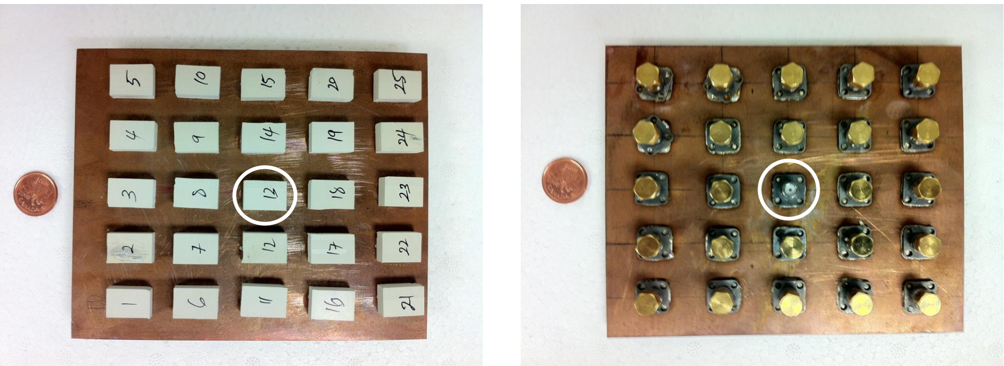

(a) (b)

Figure 3.9: Fabricated 5×5 DRA array where all ports are terminated by 50Ω except the centered element (circled) to measure its return loss: (a) Top view and (b) Bottom view.

A single DRA was fabricated using the dimensions and specifications mentioned in the previous section. This was done before performing any simulation or fabrication of the 5×5 array. The fabricated single DRA is shown in Fig. 3.7. Rogers TMM10i having dielectric constant $\varepsilon_r = 9.8$ was used as the DR material. The DR was mounted on copper ground plane of 1mm thick. A 50Ω SMA coaxial probe was used to feed the antenna. The return loss of the fabricated DRA is shown in Fig. 3.8 and compared to the simulation result.

In a large array, the characteristics of all elements will be identical except those elements at or close to the boundary of the array. Therefore, to gauge the general performance of the fabricated array working frequency, the reflection coefficient S_{11} of the center element was measured (shown circled in Fig. 3.9) while all other array elements were terminated with 50Ω loads. The measured S_{11} was measured using an Agilent 8722ES Vector Network Analyzer (VNA) while the simulation was performed using ANSYS-HFSS. Fig. 3.10 shows good agreement between the two results.

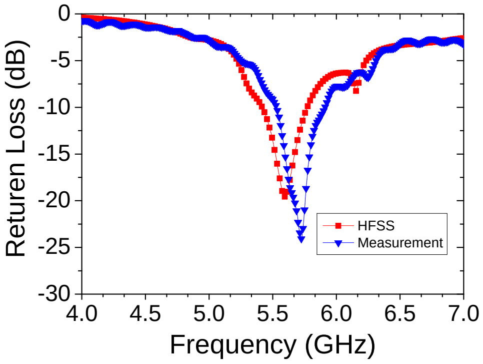

Figure 3.10: Simulation and measurement of the return loss for the central element of the 5×5 DRA array.

Next, the performance of the 5×5 array was studied as a microwaves energy absorber. The study is carried out numerically and experimentally. Figure 3.11 shows the simulation setup using ANSYS HFSS where the DRA array was illuminated by a horn antenna placed at a distance of 100 *cm*. The array was illuminated by plane waves with different incident angles. The simulated power efficiencies are shown in Fig. 3.12 for three different incident angles.

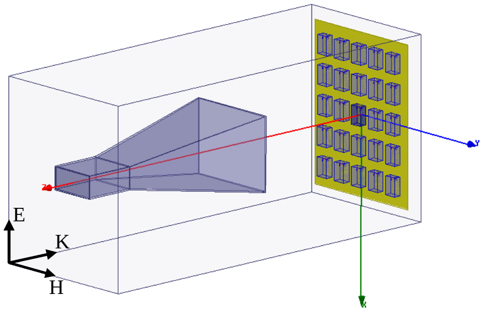

Figure 3.11: Simulation setup of the 5×5 DRA array illuminated by a horn antenna (Note: Distance between the horn and array is not to scale).

Figure 3.13 shows the measurement setup for testing the 5×5 array. A broadband horn antenna (0.7GHz to 18GHz frequency range with a maximum gain of 14.71 *dB*) was used as the source of electromagnetic power. The horn was powered by an Agilent E8257D Signal Generator. The array was placed at a distance of 100 *cm* from the horn antenna.

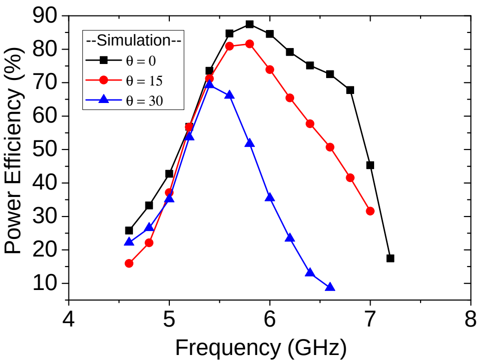

Figure 3.12: Simulation results of the power harvesting efficiency of the 5×5 DRA array for three different incidents $\theta = 0$, $\theta = 15$, and $\theta = 30$ where $\phi = 0$.

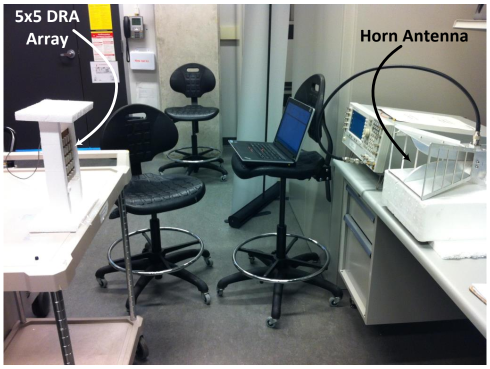

Figure 3.13: Measurement setup of the 5×5 array in the harvesting mode which shows the horn antenna (right side) as a source and the DRA array under test (left side) where the distance in between is 100 *cm*.

Each array's element contributes differently to the measured receiving power over the testing frequency range of 5GHz to 8GHz. Since the testing is for the maximum power that can be absorbed by the entire array, the power received by each element $p_{out}^{(n)}$ was measured while terminating all other ports with 50Ω load as shown in Fig. 3.9. An Agilent E4448A PSA Spectrum Analyzer was used to measure the received power. The impact of cable losses connected between the array and the spectrum analyzer was considered when calculating the total absorbed power of the array P_{out}. The total absorbed power P_{out} received by the array were then calculated using Eq. 3.3.

The power provided by the horn antenna at the array plane P_{in} was calculated using the following equations:

$$P_{in} = P_t \times \textbf{array area} \tag{3.5}$$

where:

$$P_t = \frac{P}{4\pi R^2} G_t(f) \tag{3.6}$$

P_t is the radiated power density generated by the horn at the location of the structure (receiving antenna) but without the structure present, and P is the power fed to the transmitting antenna's (horn) input terminal. R is the distance between the transmitter and the receiver. $G_t(f)$ is the gain of horn antenna as a function of frequency. In the above equation, only the area of the array was used to measure the effective aperture of the array. Normally, however, Friis equation [91] uses the gain of the array over a spherical area to measure the effective aperture of antennas. In addition, impact of gain level over the testing frequency was considered in calculating the power provided by the horn antenna. The impact of the cable losses connected between the horn and the signal generator was also measured over the testing frequency of 5GHz to 8GHz. These considerations have ensured accurate measurements of the power P_t provided by the horn antenna. The available power at the array, P_{in}, was then calculated, from which the overall power efficiency of the array was obtained using Eq. 3.5.

The maximum measured efficiency obtained for the 5 × 5 array was found to be 67% as shown in Fig. 3.14. This obtained efficiency was different from the simulated one which gave a maximum efficiency of 88% with wider bandwidth coverages as shown in Figs. 3.14.

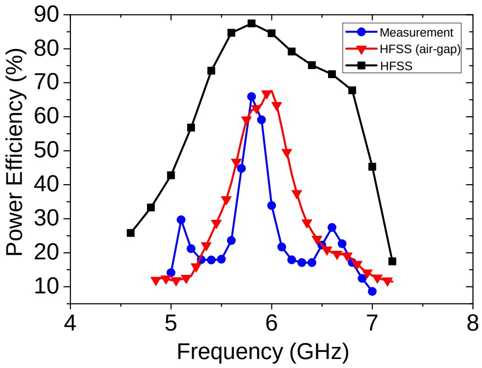

Figure 3.14: Measured power absorbing efficiency of the 5 × 5 DRA array with normal incident angle $\theta = 0$ and $\phi = 0$.

Careful scrutiny of the fabricated array revealed gaps between the DR and the conductor surface of the probe. These gaps can cause an impedance mismatch between the DR and its feeder [117] which, in turn, affects the power harvesting efficiency. To include this effect, air gaps were introduced in the simulated DRA array between the DRs and their feeding probes. The gaps were simulated by adding annular vacuum layer of thickness 0.5mm surrounding the feeding probes. This makes the hole's radius of the DRs 1.14mm instead of 0.64mm (which is also the feeding probe's radius). Good agreement is observed between the measurements and simulation when air gaps were included in the simulation as clearly shown in Fig. 3.14.

3.2.3 Discussion

The study of the single rectangular DRA has proved the capability of the antenna as energy absorber. The numerical simulation results showed that the power efficiency for a single DRA could reach a maximum of 80%. Maintaining high efficiency levels over wide bandwidth depends on the antenna probe position. The simulation of the single DRA also showed that the ground plane size has a significant impact on the harvesting efficiency. The smaller the ground plane, the higher the harvesting efficiencies. However, this conclusion applies to a single DRA and does not necessarily imply that the smaller the ground plane, the higher the absorbed power. For a single antenna in general, the absorbed energy is not limited to the precise footprint of the antenna, which in the case of the DRA, comprises the ground plane. This is because the near field of the antenna, which depends on the wavelength, extends beyond the ground plane. Therefore, the single DRA analysis is only intended to achieve preliminary conclusion about parameters that can affect the harvesting efficiency.

For the 1×3 DRA array, inter-element spacing d between array elements was found to be an important factor that influences the array efficiency. For instance, an efficiency of 20% was obtained for the 1×3 array of $\lambda/5$ inter-element spacing with a fixed ground plane (refer to Fig. 3.5(a)). The efficiency with the same inter-element spacing was dramatically increased to 80% when the ground plane sized of $W^{\prime} = L^{\prime} = \lambda/5$ (refer to Fig. 3.5(b)). In addition, when the array elements were placed with almost zero separation with a ground plane covering the area of the elements, a harvesting efficiency of 160% was obtained. The range of frequency that gives higher level of efficiencies was shifted from the resonance frequency of 5GHz by 1GHz .

For the 5×5 DRA array, the design specifications were chosen based on the studied single DRA and 1×3 array. The array was simulated and fabricated using $W' = L' =$

$d = \lambda/5$. Air gaps were noticed when performing the measurement for the fabricated 5×5 array. This factor was considered as another important factor besides the probes position that influences the level of power harvesting efficiency. These gaps were due to imprecise drilling in the DRs that resulted in wider holes than the dimensions of the feeding probes. As a result, impedance mismatching occurred between the DR elements and their feedings. This mismatching directly affects the overall harvesting efficiency. In the simulation and prior to introducing air gaps between the feeding probe and the DR, high efficiency levels between 69% and 88% were achieved over wide range of frequencies and for different incident angles. Introducing air gaps lowered the efficiency levels and narrowed the frequency band. Good agreement was obtained between measurements and simulations that accounted for air gaps. Clearly, more precise fabrications lead to higher energy efficiency levels.

Finally, it is critical to mention that the recently published works showed that ensembles of metamaterial particles provide higher harvesting efficiency than the DRA array presented here. In fact, in [118], a near-unity absorption was achieved. Comparison between the structure presented here and those reported in the literature cannot be easy as there are variety of factors that need to be considered including the frequency bandwidth and the range of incident angles over which a specific level of energy harvesting takes place. For meaningful comparison, structures need also to be tested for their energy harvesting effectiveness for different incident field polarizations. Additionally, fabrication material and cost differ sharply between dielectric resonator structures and metallic patches. All these factors make quantitative and systematic comparison difficult.

3.3 Complement Blocks of DRA for Energy Harvesting

In the previous section, a DRA array is presented as a new candidate that can efficiently used as an energy harvester. The above section has showed the effects of ground plane size and inter-element spacing on the energy harvesting efficiency of the DRA array. In particular, the study focused on the effects of mutual coupling between array elements and the size of the ground plane on the energy harvesting efficiency. Since the DRA array harvester presented in section 3.2.2 requires precise cut for the DRA elements, the final designed array was complex to fabricate and as a result creating discrepancy between simulations and measurements.

This section proposes a solution to overcome the fabrication challenge for DRA by considering the potential of having no spacing between the DRs with a minimal ground plane size which can result to have less number of elements when forming a harvesting array. In fact, the study in section 3.2.1 showed that the harvesting efficiency was improving with the minimal inter-element spacing between DRA elements; i.e., the DRs, and when having smaller ground plane size, but no analysis has been given to such considerations. This section therefore focuses on studying the harvesting efficiency using dielectric resonators as blocks; i.e., the block is formed by three elements with enter-element spacing of zero, to form an array where each block has more than three feedings.

3.3.1 Complimentary DR for Energy Harvesting

It is observed from the above study presented in section 3.2.1 for the one-dimensional array of 1×3 DRA that the smaller the ground plane, the higher the efficiency. This conclusion, although not intuitive, does not necessarily imply that the smaller the ground plane, the higher the power absorbed by the DRAs. It needs to be kept in mind that the efficiency definition is based on the total flat footprint of the entire antenna structure. Also it is observed that the inter-element spacing d between array elements and the ground plane size are important factors that affect the ground plane surface current density and distribution and as a result influence the array absorbing efficiency. For instance, efficiencies of 20% and 12% were obtained for the 1×3 array having respectively $\lambda/5$ and $\lambda/20$ inter-element spacing over a fixed ground plane (see Fig. 3.5(a)). However, higher absorbing efficiencies of 70% and 100% were obtained when shrinking the ground plane size to $W' = L' = \lambda/5$ and $W' = L' = \lambda/20$, respectively (see Fig. 3.5(b)).

The study of the above 1×3 DRA array gave insight to make an array made of DR blocks instead of using single elements. Investigating in [119] showed the highest harvesting efficiency when a zero inter-element spacing was given to the array sized of the 1×3. Have a zero enter-element makes what is called here a DR block, e.i the 1×3 with zero inter-element spacing. The DR block was designed to have dimensions of $16.5\ mm \times 34.2\ mm \times 6.35\ mm$ where the size of the ground plane is identical to the DR block as shown in Fig. 3.15(a). Using an HRM(V)-306S SMAs type 50Ω with outer radius of $2.05\ mm$ and inner conductor radius of $0.635\ mm$ and height of $5.37\ mm$. The probes are positioned where they are maximumly coupled to DR block occur.

The surface current distribution on the DR block's ground plane (see Fig. 3.15(b)) shows a potential to further minimizing the size of the ground plane which is going to be studied next. Also, the position of the exciting probes has a huge impact in the harvesting efficiency of the structure. The designs studied here were carried out and obtained directly from the full wave analysis [120].

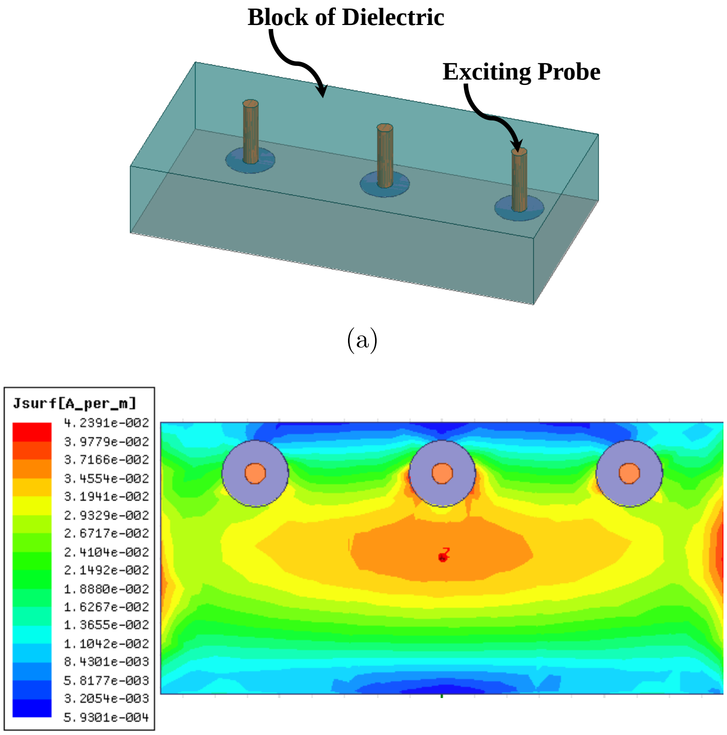

(a)

(b)

Figure 3.15: (a) Top view of the DR block. (b) Simulated surface current density at the frequency (4.4 GHz) of the maximum absorbing efficiency with normal incident plane waves.

The surface current distribution on the DR block's ground plane shown in Fig. 3.15(b) suggests a possibility to further minimizing the ground plane size. The intention here is to maximize the absorption efficiency and the coupling between the exciting probes and DR block. As the losses in the DR is almost negligible, minimizing the loses that are caused by the ground plane may minimize the loses and thus enhance the harvesting efficiency. The harvesting efficiency was defined based on the footprint (area) of the harvester [119, 92] and is given by $\eta_{eff} = P_{out}/P_{in}$. Again, this definition expresses how efficient the harvester is in converting the available incident microwave power P_{in} to the total average AC power P_{out} captured by the harvester.

Cutting the DR block ground plane around each feeding forms a 1×3 cut pieces of grounds as shown in Fig. 3.16(a), hence is referred to as a complementary DR. Different size of ground cuts have been investigated, and only the case with the highest harvesting efficiency is reported here. The surface current distribution of the optimal case is shown in Fig. 3.16(b).

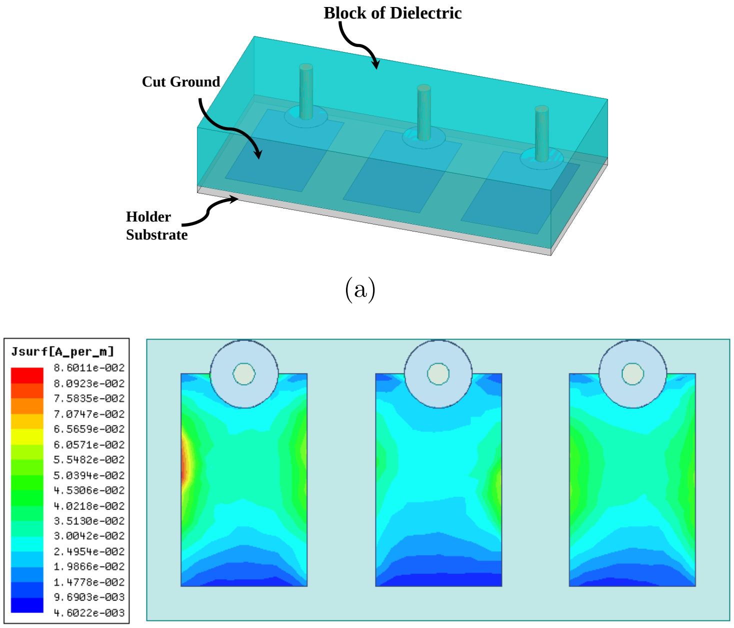

(a)

(b)

Figure 3.16: (a) Single complementary DR with 1 × 3 cut grounds. (b) Simulated surface current density at the frequency of the maximum absorbing efficiency (4.4 GHz) with normal incident plane waves.

The surface current is highly concentrated on those cut grounds. The obtained harvesting efficiency was close 180% as shown in Fig. 3.17.

Then a two-dimensional array was considered as a further extension to the above findings of the single complementary DR block. The aim here was to study a small-scale array configuration to better understand and build an efficient harvester. Thus, a 5 × 5 complementary array blocks of DR of configurations shown in Fig. 3.18 was studied.

As the array's DR blocks have to be placed next to each other with certain inter-element spacings shown in Fig. 3.18(b)), a substrate of dielectric constant of $\varepsilon_r = 2.2$ with loss tangent of 0.0009 was used. Different inter-element spacings between the DR blocks have been studied. The spacings were varied from $s = \lambda/2$ to $s = \lambda/6600$ where $\lambda = 66.67\ mm$.

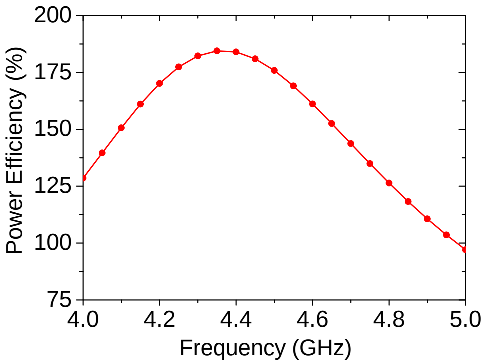

Figure 3.17: Power absorbing efficiency of a single complementary DR block with cut grounds.

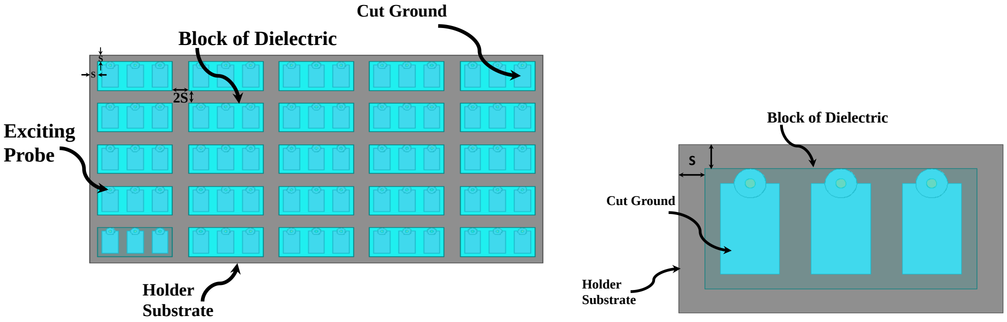

(a)

(b)

Figure 3.18: 5 × 5 complementary array blocks of DR: (a) Top view and (b) single unit top view.

In summery, the size of the DR blocks were 34.29 $mm \times 16.51$ $mm \times 6.35$ mm with dielectric constant of $\varepsilon_r = 9.8$ with loss tangent of 0.002. The holder substrate dimension of the highest resulting efficiency was 208.12 $mm \times 119.22$ $mm \times 0.787$ mm with inter-element spacing of $s = \lambda/10$. The array was then illuminated by a normally incident planewave and the maximum absorption efficiency is shown in Fig. 3.19. It was observed that the single element of this complementary block configuration is able to harvest with an efficiency of 180% whereas the efficiency of its array configuration is dropped down to 80%. This drop in the efficiency is in fact expected as our harvesting efficienct definition is more suitable to the large array configurations where the effective aperture reach the physical area of the structure. The single configuration is only given an minimum indicative of the harvesting efficiency. The later chapters will avoid this single element's efficiency by studying unit cell's configurations in periodic boundaries to represent an infinite array where the absorption and harvesting efficiency definition will make perfect sense.

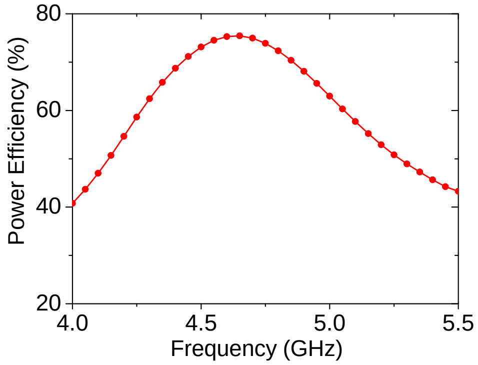

Figure 3.19: The array maximum absorption efficiency obtained when $s = \lambda/10$.

3.4 Electrically-Small DRA Elements

Electrically-small antennas generally are antennas with their longest dimension being less than or equal $\lambda/10$ of the free-space operating wavelength. DRA antennas can be miniaturized by using material with high as the size of the antenna is proportional to $1/\sqrt{\varepsilon_r}$, where ε_r is the effective permittivity of the DRA material. DRAs can be designed in smaller size than conventional metallic antennas $(1/\sqrt{\varepsilon_r})$. For example, for material with relative permittivity varying from 10 to 100, DRA size can be designed to be 5 to 10 times smaller than microstrip antennas [107]. When using high permittivity material for compact antenna designs, DRAs among other antennas offer wider bandwidth compared to microstrip antennas [108, 101].

This section presents electrically-small DRA elements as efficient energy harvesters in the microwaves regime. An electrically-small unit cell DRA is studied as a prelude to building an infinite array. Different array configurations were studied and designed to resonate around $2GHz$. The study examined different array factors that affect the efficiency of the harvested power. The coupling between adjacent cells and the self-coupling within each unit were studied to highlight their effects on the overall efficiency of the harvester.

3.4.1 Single Cell Electrically-Small DRA

The following approach was taken to design a single cell rectangular DRA. Initially a DRA cell, with operating frequency of $2GHz$ was chosen. The free-space wavelength of this operating frequency is $\lambda = 150\ mm$. For this wavelength, the longest dimension antenna to be considered as an electrically-small antenna should not exceed 15 mm ($\lambda_s = \lambda/10$). Therefore, a constraint on the size of the DR to be a cube with side dimension of λ_s or less is imposed. Then the DR's dielectric constant was determined for the operating frequency ($2GHz$) by employing the DWM formula, Eqs. 3.1 and 3.2 for the rectangular dielectric resonator [113].

The calculated dielectric constant based on the DWM formula was found to be $\varepsilon_r\ = 100$ with a side length of $0.8\lambda_s$ (12 mm). Such high dielectric constant is commercially available. A Trans-Tech (D-100 Titania) with loss tangent of 0.001 is chosen to simulate the proposed antenna. The antenna ground plan size was a square of $L = \lambda_s$ (15 mm). Rogers RT5880 of thickness 1.757 mm with a dielectric constant of $\varepsilon_r\ = 2.2$ and loss tangent of 0.0009 was used as a substrate. By using the commercial electromagnetic full-wave simulator ANSYS® HFSS™ [120], the single cell DRA was simulated to determine the position of the aperture and length of the transmission line to have the antenna resonate at $2GHz$. The following are the antenna dimensions: $w_a = 9.6\ mm$, $l_a = 1.8\ mm$, $w_L = 4\ mm$ and $L' = 0.1\lambda_s$ (1.5 mm), and are shown in Fig. 3.20.

The feeding excitation for the designed antenna consisted of an aperture and a transmission line terminated with a 50Ω load. The aperture acts as a magnetic dipole in which the aperture's position needs to be at the maximum magnetic field of the DR's desired mode at the operating frequency $2GHz$, refer to Fig. 3.20(a) for the aperture position. Later, it will be shown that the aperture excitation gives additional degrees of freedoms other than the dimension of the DR when designing an array as to maximize the goal toward the desired operation. The return loss for two different aperture positions t_a and transmission line length t_L are shown in Fig. 3.21. This figure shows how the aperture different positions affects the behavior of the antenna.

3.4.2 Array of Electrically-Small DRA cells

Our aim was to build a large array energy harvester (e.g., 20 × 20 elements) using the electrically small DRA cell that was established in previous section. Such large array is very costly to solve numerically. Therefore, enforcing periodic boundary conditions that are extending in both x–$axis$ and y–$axis$ were used to solve such a large problem as an infinite

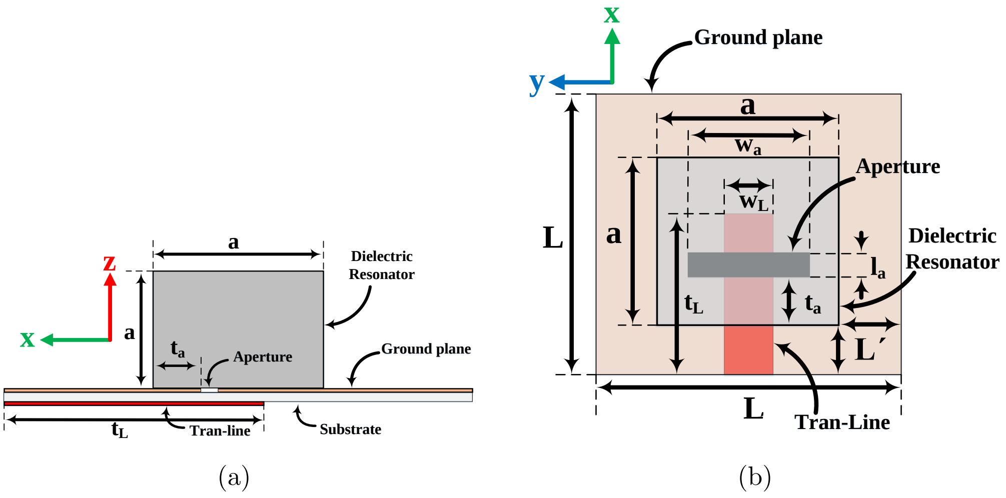

Figure 3.20: Schematic showing a single cell DRA placed on a conducting ground plane fed by a transmission line: (a) Side view and (b) Top view showing the aperture location and the design geometrical specifications.

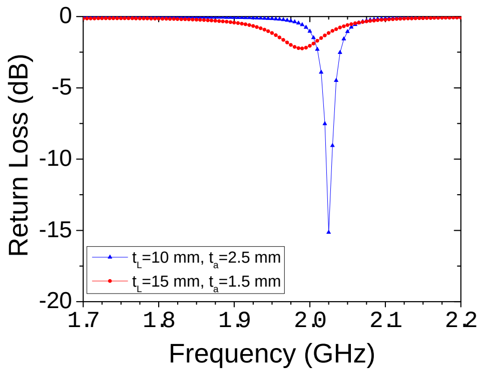

Figure 3.21: The return loss of two different configurations of a single cell DRA (refer to Fig. 3.20 for the aperture position and transmission line length).

array using ANSYS® HFSS™. The dimensions of the single cell designed in previous section were used to design the unit cell for the infinite array as shown in Fig. 3.22 (refer to Figs. 3.20 for the single cell schematic). Once the DRA cells became part of an array, the self-coupling (i.e., the energy coupled from the aperture to the DR) within each DRA cell was affected by any neighboring adjacent cell. It was noticed from the return loss of the infinite array configured using the dimensions of the single DRA cell that most of the

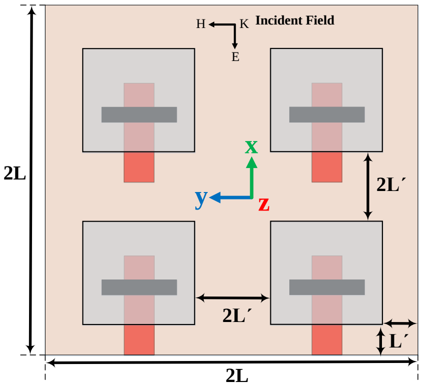

Figure 3.22: An array of 2 × 2 electrically-small DRA cells as an example to illustrate how an array of different number of cells is configured.

power was reflected as shown in Fig. 3.23.

To regain and maintain an efficient self-coupling for the array cells, different aperture positions and transmission line lengths were studied. Here, the dimensions of the unite cell of the infinite array has to be kept electrically-small and unchanged, and only the aperture position and the length of transmission line were modified to minimize the return loss reflection. Two configurations are reported here. The first case was when having $t_a = 1.5\ mm$ and $t_L = 15\ mm$. In this case, the transmission line became of the same length as the single cell where $L = 15\ mm$ (refer to the right inset attach to Fig. 3.23). This configuration has made the transmission line of the infinite array cells connected vertically, but terminated with 50Ω loads between each cell. The second case was to study the first mentioned configuration without having the terminated loads between the array cells (only the front load was kept) while keeping other specifications unchanged. For this setup, a 10 × 1 cells has been considered as a unit cell fed by a single transmission line terminated with 50Ω (refer to the left inset attach to Fig. 3.23). The two cases were studied as an infinite array using periodic boundary conditions in both $x\text{–}axis$ and $y\text{–}axis$. The return loss of the two cases is shown in Fig. 3.23.

Then a consideration is given to study the infinite array of the above mentioned configurations as an energy harvester. A normally incident plane wave was used as a source of the incident field. The overall harvesting efficiency of the array η_{eff} was defined as the ratio of the total time-average power P_{out} to the microwave power P_{in} available at the entire footprint area and dependent only on the incident plane wave, its propagation direction

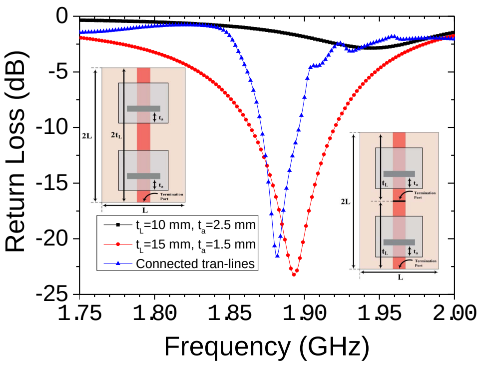

Figure 3.23: The return loss of to three different configurations of a single cell DRA (refer to Fig. 3.20 for the aperture position and transmission line length). The two insets show the two configurations when $t_a = 1.5\ mm$ and $t_L = 15\ mm$ were set. Each cell was terminated (right) and vertical cells were connected with single transmission line (left). Note: Only an example of 2×1 elements is shown.

and polarization. This efficiency is given by [92]:

$$\eta_{eff} = P_{out}/P_{in} \tag{3.7}$$

The harvesting efficiency of the normally incident microwave power based on the above efficiency definition for the three configurations are shown in Fig. 3.24. The case with connected transmission line that was terminated only in the front (the 10×1 unit cell for the infinite array) gave the highest efficiency among the cases with a harvesting efficiency close to 85%

3.4.3 Discussion

It's observed that the adjacent coupling between cells; i.e., the inter-element spacing, in an infinite array degrades the self-coupling within the unit cell and lower the harvesting efficiency as shown in Figs. 3.23 and 3.24. Also, controlling the coupling by changing the position of the aperture and the length of the transmission line gives a degree of freedoms to maximize the coupling between each DR element with its aperture and to minimize the reflection seen at termination ports for a better matching condition.

The energy harvesting efficiency for the infinite array was clearly enhanced when restoring the self-coupling by controlling the position of aperture and the length of the transmission line as shown in Fig. 3.24. The harvesting efficiency increased from 40% to 65%

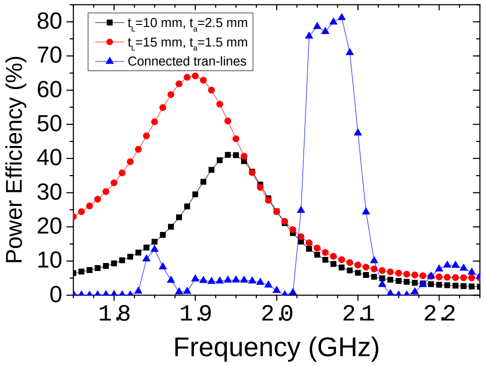

Figure 3.24: The energy harvesting efficiency for the three studied infinite array configurations.

for the cases where each cell was terminated. Exciting the 10 × 1 electrically-small cells by a single transmission line connected without any termination except at the feeding points was to further improve the harvesting efficiency and has increased it to 85%. The case of having connected transmission line array configuration is suggested to achieve a highly efficient rectenna system as it can be easily integrated with a rectification circuit.

3.5 Conclusion

This first section of this chapter (section 3.2) presents DRAs as a new candidate for microwave energy harvesting . A single and an array DRA have been studied and designed. The study has combined both simulation and measurement. The analyses included the effects of different ground plane sizes, array inter-element spacing, and positions of feeding probes. Comparisons between power efficiencies of the different configurations and different field incident angles were presented. In particular, a 5 × 5 DRA array was fabricated and tested showing measured power harvesting efficiency close to 70%.

Then the chapter extends on the study presented in the first section by conducting further analyses to the inter-element spacing and coupling between DR elements. These analyses were used to form blocks of DRs. Investigations on the ground plane current distribution have led to cut and minimize the ground size which has a great impact in the harvesting efficiency. An array of 5 × 5 blocks was considered as a two-dimension energy harvester. The obtained array efficiency was close to 80%. This array efficiency is very close to the measured and tested efficiency obtained in [119]. However, the use of the presented block concept minimizes the need to cut the DRs into very small pieces which makes the fabrication of this kind of structure much easier.

The chapter concludes with a numerical attempt study for using electrically-small DRA as an efficient electromagnetic energy harvester. Single cell self-coupling of an electrically-small DRA energy harvester was studied for better coupling optimality and low return loss reflection. Different configurations of electrically-small DRA arrays were designed and studied using an electrically-small unit cell in an infinite configuration. The 10×1 linked cells array configuration of electrically-small elements DRA shows a radiation to AC conversion efficiency close to 85%. The numerical study shows that this design configuration is potentially more suitable to be integrated with a rectification circuit, thus can be more suitable to build a complete rectenna system for full conversion from electromagnetic radiation to usable DC power.

Chapter 4

Planar Dipoles Energy Harvesting Surfaces

4.1 Introduction

In this chapter, our goal is twofold. First, to design an energy harvesting planar surface based on printed circuit board technology that has high microwaves to AC/DC conversion efficiency. While most of the previous works that show high energy harvesting efficiencies were focused on single rectennas [61], arrays of rectennas are introduced in this chapter. The rectnenna EHS are designed to have a near unity radiation to AC conversion efficiency. Second, the design ensures that the harvester provides high power density per diode to maximize diode turn-on time period over the duration of operation. To maximize the energy density per diode, harvesting with elements that are not electrically small is considered. For channeling the DC current, a channeling mechanism is introduced which places the rectification diode on the same layer of the printed dipoles. This avoids the need for an RF or DC combining circuit that require additional layers. Lastly, the proposed harvester shows less sensitivity to incident angles.

The chapter presents a design of an electromagnetic energy harvesting surface inspired by an array of printed metallic dipolar elements. The unit cell of the proposed harvester is based on two printed asymmetric off-center fed dipoles. As a proof of concept, a finite array was analyzed numerically and experimentally. The array was first analyzed for maximizing radiation to AC absorption where each dipole was terminated by a resistor across its gap. For DC conversion, the resistors were the replaced by Schottky diodes. A critical feature of the proposed designs is enhancing the power density per diode in order to maximize its turn-on time.

4.2 Radiation to DC Harvesting of Asymmetrical Planar Dipoles EHS

In light of our goal of increasing the power density per diode while achieving high microwaves to AC/DC conversion efficiency and using printed circuit board technology, as a starting point, the simplest type of antennas is considered, namely printed planar dipoles (recall that this finding is purely empirical and is based on the studied and the findings presented in section 4.2). The evolution in these findings led to the unit cell structure presented in this section. Such dipoles are appreciably larger than metasurface elements used in our earlier works and thus are expected to have equally appreciable higher power density at their input terminals. Since our interest is in large arrays (as opposed to powering electrically-small devices such as medical implants), when the printed dipoles were placed in an array form, it was found that if the dipoles were fed off center and placed asymmetrically and covered with a dielectric material, a significant enhancement in the received power is observed. Specifically, it was found that the dielectric layer must be placed in the direction of the incoming wave to affect the surface impedance seen by the incoming waves.

4.2.1 Unit Cell Design Methodology

The unit cell consists of two asymmetrical dipolar metallic elements covered with a high-permittivity dielectric superstrate shown in Fig. 4.1. To achieve full energy absorbtion at the chosen frequency of 3.4 GHz, the harvester's unit cell occupied a footprint of 18.7 mm × 38.4 mm. (note: there was no particular reason for choosing this frequency aside from compatibility with our limited testing setup and facilities.) The covering dielectric superstrate was Rogers TMM-10i material of a thickness of t = 6.35 having a dielectric constant of $\varepsilon_r = 9.8$ and a loss tangent of 0.002. The dielectric superstrate was chosen for its low loss such that the absorbed energy was not dissipated within the dielectric material. The asymmetrical dipoles have a length of L = 14.7 mm, width of W = 6.80 mm, gap of g = 1 mm, and spacing between adjacent unit cells of $s_x = 1$ mm and $s_y = 5$ mm. The separation between the two dipoles is d = 14.8 mm. The two asymmetrical dipolar elements were initially terminated by 50 Ω resistive loads across their gaps as illustrated in Fig. 4.1.

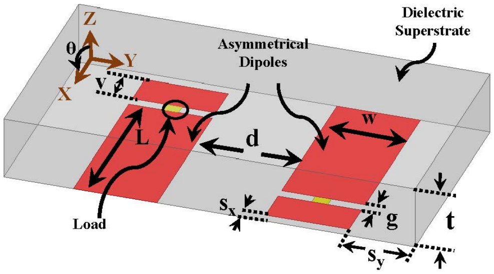

Figure 4.1: Schematic showing the unit cell of the proposed dipole absorber covered with a high-permittivity dielectric superstrate.

The input impedance of the unit cell as seen from the gap can be controlled by varying the separation distance d between the two dipolar elements. This design feature is important for DC conversion when a diode is placed across the feeding gap. Later, it will be shown that the input impedance of the dipoles can be tailored by tuning d in order to match a diode that is needed for eventual DC rectification. In fact, such tuning eliminates the use of a matching network between the antenna and the diode.

All the numerical simulations needed for this work used ANSYS® HFSS™ [120]. Since numerous simulations were required during our design development stage, for computational efficiency, a single unit cell was simulated on the assumption that it lies in an infinite periodic structure. Since an infinite array is neither practical nor the intended goal of this work, a unit cell positioned in the middle of a large array is expected to have highly similar behavior to a unit cell placed in an infinite array. To this end, the periodic boundary condition was used to model a periodically infinite structure in the $x - y$ plane of the unit cell [121]. Master and slave boundaries were applied on the faces parallel to the wave propagation direction (the negative $(\hat{z})$ direction). The unit cell of the energy harvesting surface was illuminated by a normally incident plane wave propagating in the negative $(\hat{z})$ direction using a Floquet port. Floquet excitation modes were used to simulate the incident wave with specular modes consisting of two orthogonally polarized plane waves propagating normally to the $x - y$ plane of the unit cell. Initially, and for the purpose of gauging the effectiveness of the absorber to absorb and channel energy to a load, lumped resistors were placed across the gaps of the two metallic elements. These resistive loads will be replaced later by a rectification circuit having an input impedance matched to the unit cell's impedance at the maximum power absorption frequency.

The radiation to AC/DC absorption efficiency describes the ability of an absorber to capture the energy per footprint area [77]. What is referred to in this work as a radiation to AC efficiency is the efficiency of the harvester to transfer the total power incident on a specific area to available power at the feed (i.e., where a resistive load or rectifying circuitry is placed, referred to as the load location in Fig. 4.1). The radiation to AC conversion efficiency is calculated by calculating the footprint (surface area) in square meters. The Radiation to AC conversion efficiency of an energy harvester occupying a specific footprint is then described as

$$\eta_{Rad-AC} = P_{out}/P_{in} \tag{4.1}$$

where P_{in} is the total time-average power incident on the footprint, and P_{out} is the available time-average AC power received by the harvesters' collectors (i.e., where a resistive load or a diode rectifying circuity is placed) and is given by

$$P_{out} = \sum_{n=1}^{N} V_i^2/R_i \tag{4.2}$$

where V_i is the voltage across the resistance of the i^{th} collector, R_i and N is the total number of collectors.

This Radiation to AC efficiency definition is indicative of the ability of the harvester to utilize the available electromagnetic energy incident on a given area and the ability of the harvester or its collectors to deliver the absorbed energy to resistive loads. This definition provides a measure of how efficient the absorber, occupying a specific footprint, in converting the available incident microwave power to RF energy.

The simulated radiation to AC power conversion efficiency of the surface (assuming infinite periodicity) is shown in Fig. 4.2. Based purely on empirical findings, the asymmetrical dipoles were found to give higher harvesting efficiency than symmetrical dipoles with center feeding or off-center feeding. In fact the asymmetrical case provided more than 40% increase in efficiency compared to the other cases.

The design of the unit cell presented shows a very high radiation to AC conversion efficiency approaching unity at a frequency very close to the design frequency of 3.4 GHz. If harvesting at a different frequency is desired, the design parameters such as the dipoles length and width, superstrate material and thickness, and separation distance between the dipole can all be adjusted accordingly. It is important to realize that the near-unity radiation to AC conversion efficiency achieved here used energy harvesting elements having dimensions appreciably larger than the metamaterial elements used in earlier works [77, 80]. The significance of such achievement is primarily due to reducing the requirement for the number of rectification diodes per footprint, which implies higher power density per diode. This in turn is expected to maximize diode turn on time and thus higher overall efficiency in practical applications where the incident field power density cannot be predicted in advance.

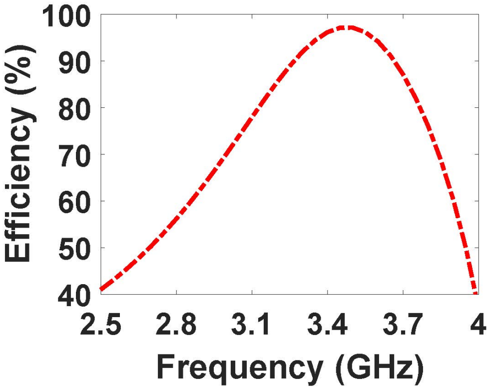

Figure 4.2: The simulated radiation to AC conversion efficiency for the unit cell when the structure is illuminated by a plane wave traveling in the negative $(\hat{z})$ direction. The dipoles are terminated with 50 Ω loads.

For radiation to DC conversion, the input impedance of the dipoles need to be analyzed. Lumped excitation ports were placed at the asymmetrical dipolar elements' terminals (i.e., replacing the lumped loads used to determine the radiation to AC conversion efficiency) in order to calculate the input impedances of the dipoles. The Floquet port in this case was replaced by a radiation boundary on top of the structure. For a fixed size unit cell of the proposed absorber, the input impedance appeared at the dipolar elements' terminals can be controlled by changing the inter-spacing between the asymmetrical dipoles. An HSMS-2860 Schottky diode was considered in this work. The diode has an input impedance of Z_d= 184 - j45 Ω when terminated with a load of 300 Ω at a frequency of 3.4 GHz (the input impedance was obtained from its model [96].)

DC channeling can be accomplished by connecting a diode directly across each dipole terminals and routing the resulting DC currents through copper planar wires placed on the same plane of the dipoles or through vias to a different layer. The first option introduces additional wiring that can potentially alter the absorption effectiveness of the unit cell, whereas the latter option requires the fabrication of vias and an additional metalization layer, both of which add appreciable fabrication cost. Instead, small connectors to the unit cell are introduced as shown in Fig. 4.3. Naturally, the DC connectors altered the topology of the unit cell and the dipoles, however, their input impedance was slightly affected. In fact, the DC connectors essentially increased the size of the dipoles. Thus, to maintain maximum absorption around the frequency of interest (3.4 GHz), the unit cell dimensions and the spacing between the asymmetrical dipolar elements were modified to achieve the desired input impedance, which is the conjugate of the diode's impedance. The dimensions

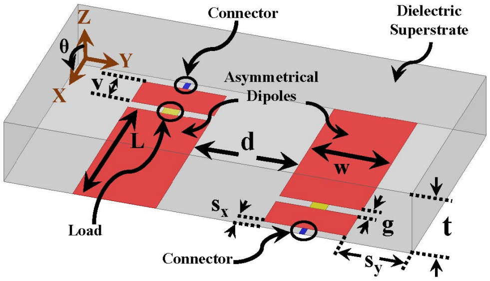

Figure 4.3: Schematic showing the unit cell of the proposed energy harvesting surface showing the connectors used for DC channeling.

of the modified unit cell became as follow: L=8.35 mm, W=6.80 mm, v=2 mm, g=1 mm, d=10.79 mm, s_x=1 mm, and s_y=7 mm. The size of the unit cell became 12.35 mm × 38.39 mm. The thickness of the superstrate was kept unchanged at t = 6.35 mm.

To verify the surface performance of the modified design (with DC connectors), the unit cell dipoles were terminated by lumped elements having the conjugate impedance of the dipoles. The radiation to AC power conversion efficiency for the unit cell with DC connectors is shown in Fig. 4.4 when the absorber was illuminated by a plane wave traveling in the negative ($\hat{z}$) direction.

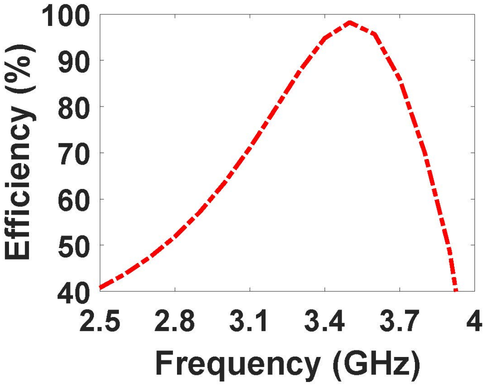

Figure 4.4: The simulated radiation to AC power conversion efficiency for the modified design with DC connectors (infinite periodic array) when illuminated by a plane wave traveling in the negative ($\hat{z}$) direction. The dipoles were terminated with 184 - j45 Ω.

In some applications, the harvesting surface is placed above a conducting surface. Therefore, the proposed surface was tested when backed by a perfect electrically con-

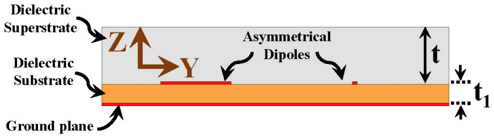

Figure 4.5: A schematic of the side view for the dielectric and PEC backed harvester.

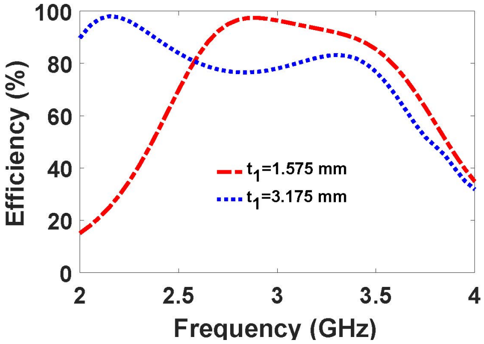

Figure 4.6: Simulated radiation to AC power conversion efficiency for the finite array when backed by a low permittivity dielectric layer and PEC plane.

ducting (PEC) surface. A low permittivity substrate separated a PEC surface from the metalized layer of the harvester as shown in Fig. 4.5. Two different grounded substrate thicknesses of $t_1 = 1.575$ mm and 3.175 mm of Rogers 5880 material having a dielectric constant of $\varepsilon_r = 2.2$ were tested. Figure 4.6 shows numerical simulation of the radiation to AC efficiency. The grounded low-permittivity substrate is observed to provide a wider frequency absorption range.

Next, an analyze for the behavior of a finite array is considered. The numerical setup is shown in Fig. 4.7 where a horn antenna is used in the simulation to provide a physically-realistic plane wave as opposed to the plane wave feature available in HFSS$^{\mathrm{TM}}$. A finite size array consisting of 9×3 unit cells in the $x - y$ plane using a Rogers TMM-10i superstrate was numerically simulated. The dipoles were all terminated by their conjugate input impedance (recall that the unit cell was designed such that the input impedance of the dipoles were the conjugate of the input impedance of the Schottky diode at 3.4 GHz and when terminated with 300 Ω.) The entire array size was 111.2 mm × 115.2 mm.

The simulated radiation to AC efficiency for the finite array is shown in Fig. 4.8 when it was illuminated by a plane wave traveling in the negative ($\hat{z}$) direction. The total available

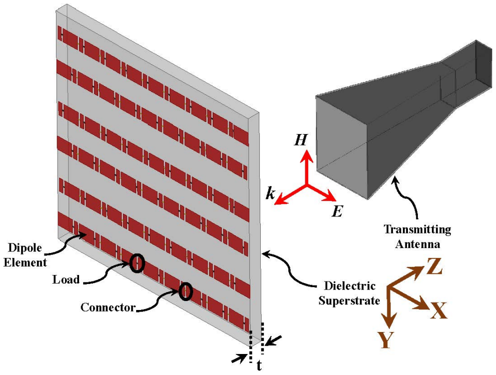

Figure 4.7: A schematic showing the proposed planar dipole array energy absorber covered with a dielectric superstrate under illumination by a transmitting horn antenna.

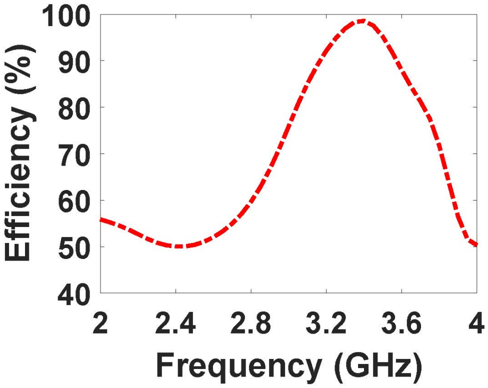

Figure 4.8: Simulated radiation to AC absorption for the finite array when the structure is illuminated by a plane wave traveling in negative $(\hat{z})$ direction.

absorbed power is given by

$$P_{out} = \sum_{n=1}^{N} p_{out}^{(n)} \tag{4.3}$$

where N is the number of elements in the array and $p_{out}^{(n)}$ is the received power from each array element.

Figure 4.9 shows the simulated surface current on the absorber's conducting elements and the magnitude of the electric field on the absorber's bottom layer. Both, the current and electric field were taken at the maximum absorption frequency 3.4 GHz with incidence

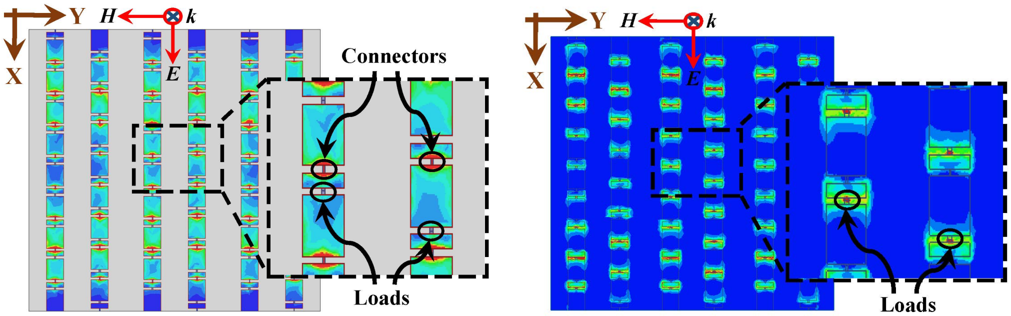

(a)

(b)

Figure 4.9: (a) Surface current distribution on the dipole elements and (b) Electric field magnitude on the bottom layer at the maximum absorption frequency of 3.4 GHz when illuminated by an plane wave incident in the negative ($\hat{z}$) direction. The surface current highest intensity (red) corresponds to 7×10^{-2} A/m and the lowest intensity (blue) corresponds to 8×10^{-5} A/m. The electric field highest intensity (red) corresponds to 12 V/m and the lowest intensity (blue) corresponds to 1.25×10^{-2} V/m.

plane wave propagating in the negative ($\hat{z}$) direction. Of course, since the array is not infinite, some non uniformity is observed in the current and field distributions. Interestingly, however, significantly higher current density is observed through the DC connectors in comparison to the impedance loads. The reason for having higher current densities developed on thesis little DC connectors can be due to the higher inductance that is developed when linking the dipole cells to form an array.

To visualize the physical response of the absorbers to the plane wave excitation, the time-averaged Poynting vector of the total field is shown in Fig. 4.10 at 3.4 GHz when the structure is illuminated by a plane wave traveling in the negative ($\hat{z}$) direction. Fig. 4.10 clearly shows the channeling of the power of the incident plane wave as it propagates closer to the surface and eventually into the impedance loads. It is critical to note that even though the absorber surface not being homogeneous (i.e., not in the macroscopic sense) nor being composed of periodic arrangement of electrically-small cells as in metasruface type absorbers, the absorber's elements are practically channeled all the energy into the designated loads. The significance of this physical insight is that one does not need an absorbing surface with uniform surface impedance matched to free space to achieve full energy absorption.

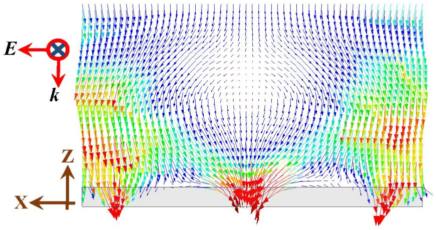

Figure 4.10: The Poynting vector of the total incident field at the maximum absorption frequency of 3.4 GHz when the structure is illuminated by an incident plane wave traveling in the negative ($\hat{z}$) direction. The highest intensity (red) corresponds to 2×10^{-3} W/m^2 and the lowest intensity (blue) corresponds to 8×10^{-5} W/m^2.

4.2.2 Experimental Verification

The planar array absorber was fabricated using the above simulated array's specifications. Figure 4.11 shows an array of 9 × 3 made with the TMM-10i superstrate. The surface was illuminated by a broadband commercially available horn antenna (0.7 GHz to 18 GHz frequency range with a maximum gain of 14.71 dBi) placed at a distance of 1 m for a plane wave illumination. The broadband horn antenna was excited by a Keysight signal generator through with a 42 dB gain power amplifier to investigate the required power level that would allow the diode to operate at its maximum efficiency. The experiments were carried out in an anechoic chamber for maximum accuracy. Also, the impact of the horn antenna gain level over the testing frequency was carefully considered in calculating the power provided by the horn antenna. The cable loss connecting the horn antenna to the signal generator was also measured over the testing frequency. The following formula was then employed to calculate the power provided by the horn antenna at the absorber plane P_{in}:

$$P_{in} = A \times P_t, \tag{4.4}$$

where

$$P_t = \frac{P}{4\pi R^2}\, G_t(f) \tag{4.5}$$

A is the harvester surface area (footprint), P_t is the radiated power density generated by the horn at the harvester surface plane in the absence of the harvester, and P is the power fed to the transmitting horn's input terminal. $G_t(f)$ is the gain of the horn antenna as a function of frequency and R is the distance between the horn antenna and the array.

The available power at the absorber plane, P_{in}, was then calculated from which the overall power absorption of the array can be obtained using Equation 4.1.

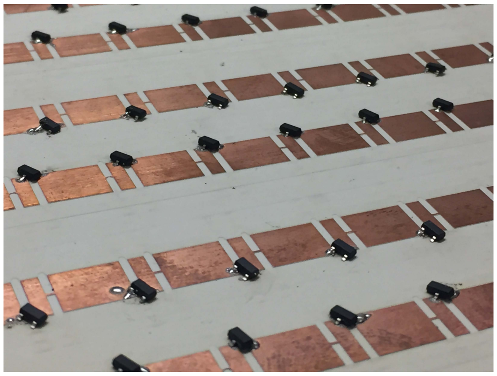

Figure 4.11: The fabricated bottom view of the planar dipole absorbers covered by high permittivity superstrate made of Rogers TMM-10i material.

The nonlinear performance of the rectifying diodes will have an effect on the absorber rectifying/absorption performance for various DC connections topologies (i.e., series or parallel connection of the absorber's elements), loads, incident power and frequencies [122, 123]. Therefore, a balanced topology between series and parallel connections was considered for the DC measurements where each two columns of the array elements in the $\hat{x}$ axis were connected in series and then connected in parallel. A schematic representing the chosen DC channeling topology is shown in Fig. 4.12.

The fabricated planar dipole array using Rogers TMM-10i shown in Fig. 4.11 was illuminated by the horn antenna in negative ($\hat{z}$) direction (refer to Fig. 4.7 for the illumination directions). The load impedance and power at the receiving end were swept at the highest absorption frequency of 3.4 GHz. The purpose of those sweeps was to find the optimal DC load and input power that will deliver maximum power across the load. Figures 4.14(a) and 4.14(b) show that the harvesting surface achieves maximum power across the load when illuminated by a power level of 27 mW (i.e., the available power at the absorber plane, P_{in}) with a load of 2 kΩ for $-\hat{z}$ illumination. This optimal load value was in fact expected which is the result of connecting 18 dipolar elements (two columns of the array elements along the $\hat{x}$ axis) of the harvesting array with 300 Ω termination loads in series and then connected in parallel as illustrated in Fig. 4.12.

The DC absorption efficiency for the illumination in the negative ($\hat{z}$) direction was then recorded at multiple frequency points at which the absorber had maximum power across the load (i.e., with the optimal obtained input power and load). This is given in Fig. 4.15.

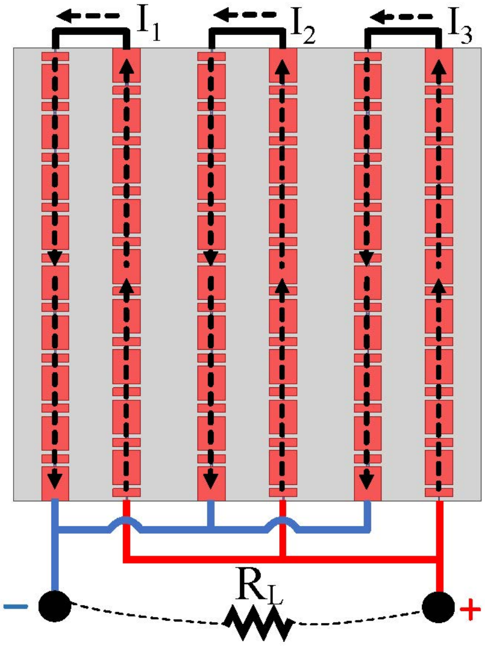

Figure 4.12: A schematic showing the DC current channeling configuration adopted for the harvesting array.

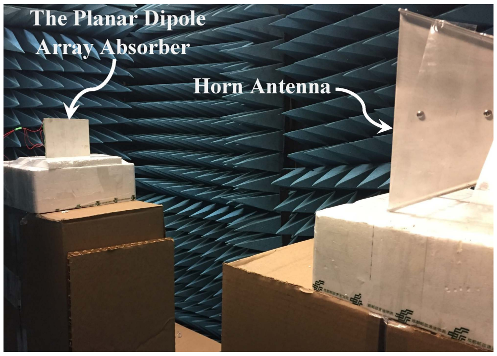

Figure 4.13: The absorber under illumination by a broadband horn antenna for DC measurements.

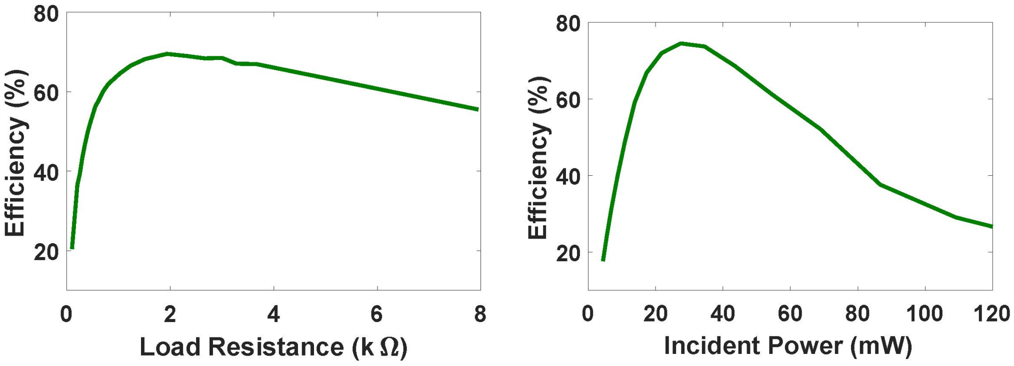

(a)

(b)

Figure 4.14: Measured DC absorption as a function of (a) the load impedance and (b) the available power at the absorber plane P_{in} when the structure is illuminated by a horn antenna in the negative $(\hat{z})$ direction.

The absorber achieved a radiation to DC conversion efficiency of 76%. Finally, the absorber was tested for capturing the incoming radiation at different angles of incidence. Fig. 4.16 shows the measurement results for different angels of illumination. The simulated radiation to DC absorption η_{Rad-DC} efficiency given in Figs. 4.15 and 4.16 was calculated as follows

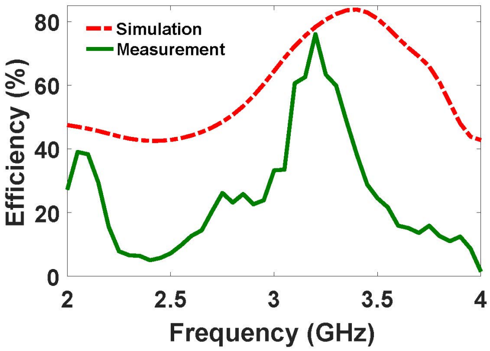

Figure 4.15: Efficiency of the measured and simulated radiation to DC absorption of the dipole array harvester as a function of frequency when the structure is illuminated by a horn antenna in the negative $(\hat{z})$ direction.

$$\eta_{Rad-DC} = \eta_{Rad-AC} \times \eta_{AC-DC} \tag{4.6}$$

where η_{Rad-AC} is the harvester radiation to AC efficiency and η_{AC-DC} is efficiency of the rectifier over the tested frequency range 2 to 4 GHz, with a 300 Ω termination load.

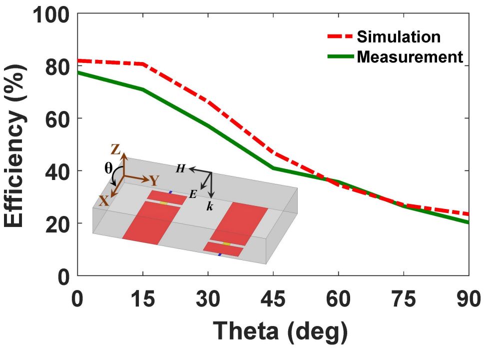

Figure 4.16: Efficiency of the measured and simulated radiation to DC absorption of the dipole array harvester as a function of different incident illuminations when E-field polarized in the positive ($\hat{x}$ direction (Note: The normal incident illumination is in the negative ($\hat{z}$) direction.

4.3 Multi-Polarization Multilayer Planar Dipoles EHS

This section presents a design of a multi-polarization electromagnetic energy harvesting surface inspired by a multi-layer unit cell of printed asymmetrical metallic dipolar elements that is presented in previous sections. The harvesting array features two layers that collectively capture the incident energy from various incident angles. The harvester was first analyzed for maximizing radiation to AC absorption where each dipole was terminated by a resistor across its energy-collecting gap. In the two previous sections, EHS arrays were designed to have a near unity radiation to AC conversion efficiency. However, those EHSs were only capable of harvesting the incoming electromagnetic energy in one polarization. While most of the previous works that show multi-polarization high energy harvesting efficiencies were focused on single rectennas [61], this section will introduce the harvesting for multiple polarizations using an array of multiple layers using the previously developed asymmetrical dipolar elements. The design ensures that the harvester can efficiently absorb at different polarization incidents using appreciably electrically large elements in order to maximize the energy density per diode. Lastly, the design also avoids the use of any complicated RF or DC combining or feeding circuit and vias that require adding more layers to the structure.

4.3.1 Unit Cell Design Methodology

Guided by our recently published paper [124] that showed the possibility of achieving a near-unity AC absorption of the incoming electromagnetic energy, the goal in our approach here was to build a multi-polarization harvester. The work in [124] interestingly uses asymmetrical planar dipoles (i.e., the elements are not electrically very small like in metamaterials or metasurfaces [125, 82]) with a unit cell consists of two asymmetrical dipolar metallic elements covered with a high-permittivity dielectric superstrate without a backed ground plane as shown in Fig. 4.17. In [124], the possibility of placing the asymmetrical dipolar harvester above a conductive surface was numerically simulated using a low permittivity substrate that separates the conductive surface from the metalized layer. This consideration was taken to isolate the portion of the far field that may affect the harvesters elements. It is noted that that the backed with grounded low-permittivity substrate, planar asymmetrical dipole harvester provides a wider frequency absorption range.

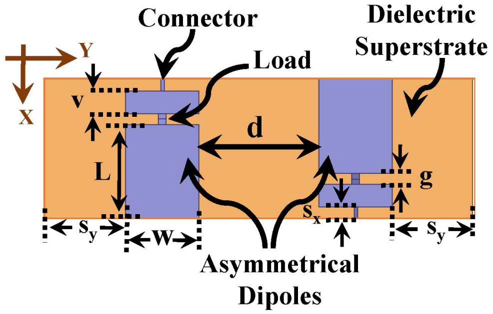

Figure 4.17: Schematic showing the unit cell of the proposed dipole harvester covered with a high-permittivity dielectric superstrate Schematic with the integrated connectors used for DC channeling.

In light of our finding in [124] that showed the possibility of backing the harvesting structure with another layer, a multi-layer harvesting structure is considered to collect the energy from multiple polarizations. To this end, the unit cell shown in Fig. 4.18 is considered that consists of two layers asymmetrical dipolar metallic elements where each elements' layer is covered with a different thickness high-permittivity dielectric superstrate and backed with a grounded low-permittivity substrate. The unit cell shown in Fig. 4.18 is composed of 1x3 elements of the unit cell shown Fig. 4.17. Each layer was intended to fully absorb one polarization, namely the $\phi = 0$ and $\phi = 90$ polarization angles. To achieve the desired input impedance that is conjugate to a diode's input impedance and have an efficient energy absorption at the chosen frequency of 3.25 GHz, the unit cell dimensions

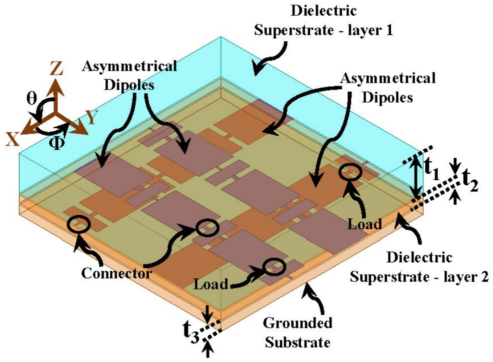

Figure 4.18: Schematic showing the defined unit cell structure of the two-layer energy harvester backed with a grounded low-permittivity substrate used to simulate an infinite periodic array.

and the spacing between the asymmetrical dipolar elements for each layer were found to be as follow for layer 1 (top layer) and layer 2 (bottom layer): L=8.35 mm, W=6.80 mm, v=2 mm, g=1 mm, d=10.79 mm and s_x=1 mm. The size of the two layers is identical with a footprint size of 12.35 mm × 38.39 mm where only the element spacing d is different in each layer. The spacing between the asymmetrical dipoles for layer 1 and layer 2 are d_1 = 10.79 mm d_2=6.63 mm, respectively. The covering dielectric superstrates were Rogers TMM-10i material having a dielectric constant of ε_r =9.8 and a loss tangent of 0.002 of a thickness of t_1=6.35 mm for layer 1 and a thickness of t_2=2.54 mm for layer 2. Stacking the harvester's layers on top of each other creates a small air gap between the layers because of rectifying diodes' hight that will be mounted on each layer. Thus, vacuum layers were sandwich between each of the harvester's layer to account for the diodes' hight. This approach was taken to minimize the discrepancy that may occur between the simulation and measurement results.

An infinite array is considered to simulate the harvesting structure. The infinite array simulation significantly reduces the computation complexity without compromising the behavior of simulated structure as it is expected to similarly behave as a large array. Therefore, periodic boundary conditions were used to model an infinite structure in the $x - y$ plane of the unit cell shown Fig. 4.18. Master and slave boundaries were applied on the faces parallel to the wave propagation direction negative $(\hat{z})$ direction). The energy harvesters unit cell was illuminated by a normally incident plane wave propagating in the negative $(\hat{z})$ direction using Floquet port considering two polarizations, namely $\phi = 0$ when the E-field is aligned on the x-axis and $\phi = 90$ the E-field is aligned with the y-axis.

In this work, the definition of the radiation to AC/DC absorption efficiency is considered as the ability of an absorber to capture the energy per footprint area following [77]. This Radiation to AC efficiency definition is indicative of the ability of the harvester to utilize the available electromagnetic energy incident on a given area and the ability of the harvester or its collectors to deliver the absorbed energy to resistive loads. Thus, the radiation to AC efficiency is defined as the efficiency of the harvester to transfer the total power incident on a specific area to available power at the feed (i.e., where a resistive load or rectifying circuitry is placed, referred to as the load location in Fig. 4.17). The radiation to AC conversion efficiency is calculated by calculating the footprint in square meters. The Radiation to AC conversion efficiency of an energy harvester occupying a specific footprint is then described as

$$\eta_{Rad-AC} = P_{out}/P_{in} \tag{4.7}$$

where P_{in} is the total time-average power incident on the footprint, and P_{out} is the available time-average AC power received by the harvesters' collectors (i.e., where a resistive load or a diode rectifying circuity is placed) and is given by

$$P_{out} = \sum_{n=1}^{N} V_i^2/R_i \tag{4.8}$$

where V_i is the voltage across the resistance of the i^{th} collector (R_i) and N is the total number of collectors.

Another step was considered here in the simulation environment for the radiation to DC conversion efficiency. This step was take to match the input impedance of the multi-layer harvester to a conjugate input impedance of a diode. Lumped excitation ports were placed at the asymmetrical dipolar elements' terminals in order to calculate the input impedances of the dipoles. An HSMS-2860 Schottky diode was considered in this work. The diode has an input impedance of Z_d= 200 - j40 Ω when terminated with a load of 300 Ω at a frequency of 3.25 GHz (the input impedance was obtained from its model [96].

The simulated radiation to AC efficiencies are shown in Figs. 4.19 and 4.20 for the multi-layer harvester when the harvester is matched to the chosen Schottky diode's impedance for the $\phi = 0$ and $\phi = 90$ polarizations, respectively. Here, the total available harvested power was calculated as follow:

$$P_{out} = \sum_{n=1}^{N} p_{out}^{(n)} \tag{4.9}$$

where N is the number of elements in the unit cell and $p_{out}^{(n)}$ is the received power from each dipolar element.

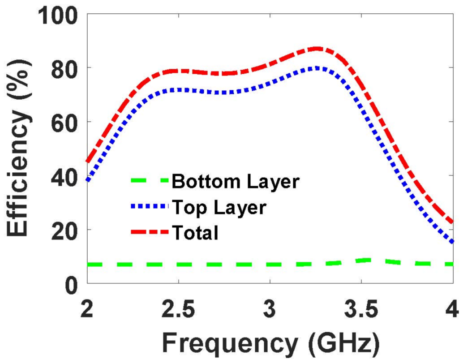

Figure 4.19: The simulated radiation to AC power conversion efficiency for the two-layer harvester with DC connectors (infinite periodic array) illuminated by a plane wave traveling in the negative ($\hat{z}$) direction with incident angle of $\phi = 0$ and $\theta = 0$ (refer to Fig. 4.18 for the illumination directions).

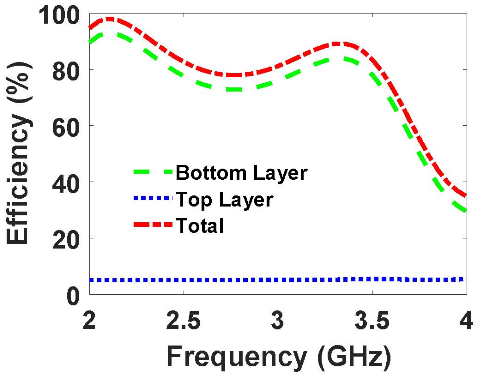

Figure 4.20: The simulated radiation to AC power conversion efficiency for the two-layer harvester with DC connectors (infinite periodic array) illuminated by a plane wave traveling in the negative ($\hat{z}$) direction with incident angle of $\phi = 90$ and $\theta = 0$ (refer to Fig. 4.18 for the illumination directions).

Figure 4.21 shows the simulated surface current on the absorber's conducting elements on the absorber's two layers. The current was taken at the maximum absorption frequency 3.25 GHz with incidence plane wave propagating in the negative ($\hat{z}$) direction for the two layers at E and H incident polarizations. It is observed from Fig. 4.21 significant higher current densities that flow through the DC connectors.

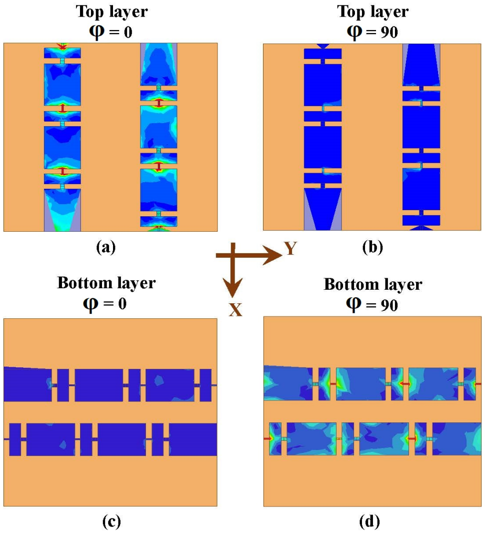

Figure 4.21: Surface current distribution when the harvester illuminated at different incident planes for (a) the top layer with ϕ = 0, (b) ϕ = 90, (c) the bottom layer with ϕ = 0 and (d) ϕ = 90. The surface current on the layers were measured at the absorption frequency of 3.25 GHz when illuminated by a normal incident plane the negative ($\hat{z}$) direction. The surface current highest intensity (red) corresponds to 1.2×10^2 A/m and the lowest intensity (blue) corresponds to 4 A/m.

4.3.2 Experimental Verification

A finite size array of 3 × 3 elements of the defined multi-layer unit cell shown in Fig. 4.18 was fabricated using the above-mentioned design specifications. The array consists of two layers of the same number of elements using Rogers TMM-10i as a superstrate for each layer. The array was backed with a grounded substrate made of RT/duroid 5870. The surface was illuminated by a broadband commercially available horn antenna (0.7 GHz to 18 GHz frequency range with a maximum gain of 14.71 dBi) placed at a distance of 1 m to ensure a far-field plane wave illumination. The broadband horn antenna was excited by a Keysight signal generator through with a 42 dB gain power amplifier to investigate the required power level that would allow the diode to operate at its maximum efficiency as shown in Fig.4.22. The experiments were carried out in an anechoic chamber for maximum accuracy. The following formula was then employed to calculate the power provided by the horn antenna at the absorber plane P_{in}:

$$P_{in} = A \times P_t, \tag{4.10}$$

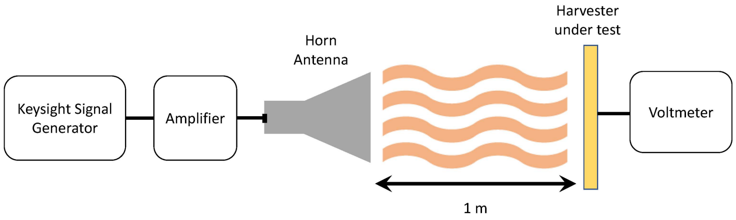

Figure 4.22: Schematic illustrates the measurement setup.

where

$$P_t = \frac{P}{4\pi R^2}\, G_t(f) \tag{4.11}$$

A is the harvester surface area (footprint), P_t is the radiated power density generated by the horn at the harvester surface plane in the absence of the harvester, and P is the power fed to the transmitting horn's input terminal. $G_t(f)$ is the gain of the horn antenna as a function of frequency and R is the distance between the horn antenna and the array. The available power at the absorber plane, P_{in}, was then calculated from which the overall power absorption of the array can be obtained using Eq. 4.7.

The DC absorption efficiency for the illumination in the negative $(\hat{z})$ direction was then recorded at $\phi = 0$ and $\phi = 90$ incident polarizations at multiple frequency points. The frequency sweeps were taken with the optimal input power level and load to ensure maximum harvesting power across the terminated load. The radiation to DC conversion efficiencies for $\phi = 0$ and $\phi = 90$ incidents are shown in Fig. 4.23 yielding a radiation to DC conversion efficiency of 70% at the two incident polarizations.

4.3.3 Discussion

The discrepancy between the simulation results shown in Figs. 4.19 and 4.20 and the measurement shown in Fig. 4.23 is mainly due to the non-linearity behavior of the rectifying diodes. The diodes turn-ON voltages are intrinsically dependent on the operating frequency, level of power, and the terminated load connected to the circuit. It is critical to emphasize that all simulated efficiencies only represent the Radiation to AC conversions in which the harvester captures the incident energy. The captured energy gets efficiently dissipated across resistive loads that their values are the conjugate impedance of the chosen diode (Z_d= 200 - j40 Ω). The measurement results, on the other hand, show the results of the radiation to DC efficiency. In the simulation results, the diodes input impedance was determined at 3.25 GHz while terminated with a 300 Ohm resistor. Therefore, the

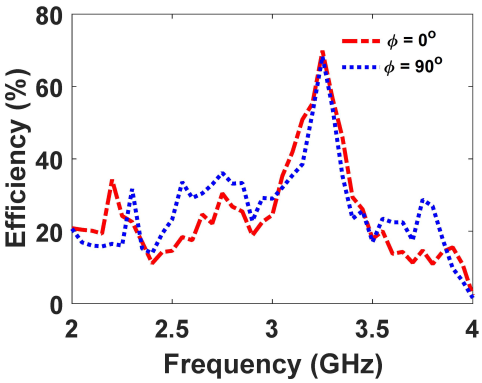

Figure 4.23: The efficiency of the measured radiation to DC absorption of the dipole array harvester as a function of different frequencies when illuminated by a normal plane wave traveling in the negative $(\hat{z})$ direction with different planes of incident angles, $\phi = 0$ and $\phi = 90$. Note: The normal incident illumination is in the negative $(\hat{z})$ direction with $\theta = 0$ with the E-field polarized in the positive $(\hat{x})$ direction (refer to Fig. 4.18 for the illumination directions).

energy harvesting structure was optimally designed to be matched with the diodes only at 3.25 GHz with a load termination of 300 Ohm. Mismatching between the diode impedance and the array elements impedance is in fact expected outside of the optimal absorption frequency 3.25 GHz due to the nonlinear behavior of the rectifying diodes.

4.4 Conclusion

This chapter introduces a study of the material aspect for the absorption of electromagnetic energy and WPT. The unit cell considered in this chapter consists of two asymmetrical dipole elements covered with a high-permittivity dielectric material. A load that maximizes the absorption of the incoming energy is placed at each dipole. Our study suggests that asymmetrical dipoles with a superstrate were capable to maximize the absorption efficiency as well as to increase the power density appeared at the energy collectors with a wide absorption bandwidth. This asymmetrical configuration can be considered as an efficient EHS when combining rectification circuits utilizing the radiation to DC conversion.

Although metamaterial array structures based on populated electrically-small resonators were capable of providing high absorption as energy absorbers [77, 80, 78], the level of power density appeared at each resonator element is low [74]. As the ultimate goal is to rectify and channel the absorbed AC power, the low-density factor, in fact, degrades the radiation to DC efficiency as a more complicated rectifying circuitry and channeling mechanism might be required.

A planar dipole EHS array covered with a high-permittivity dielectric superstrate was built and tested first for radiation to AC conversion as an efficient microwave energy absorber operating in the microwave regime. The proposed absorber is based on appreciable electrically-large elements that are capable of not only high absorption efficiency but also more power density per dipole element. Different superstrates materials were considered showing their effects in the absorption efficiency as well as in the desired operating frequency. A unit cell of the proposed absorber comprises two dipoles with asymmetric feeding gaps. As a proof of concept, an array of 8×4 unit cells covered with a dielectric superstrate was analyzed numerically and experimentally where each dipole element was terminated by a resistor across its gap. The simulation and experimental results showed a radiation to AC absorption efficiency of 99% and 96%, respectively. The primary advantage of this absorber is maximising the energy density per load which is a highly critical consideration for wireless power transfer applications.

Building upon the encouraging measurement results achieved for the radiation to AC absorption was considered next as a forward logical step to build complete energy harvesting system. The concept of using EHS for electromagnetic energy is extended to build a full harvester and WPT system to convert the electromagnetic radiation to usable DC power. The harvester unit cells consists of two asymmetrical dipolar elements covered with a high permittivity dielectric superstrate. The energy harvesting surface was tested for its potential as an absorber to channel energy by placing a resistive load across the gaps of the dipoles. The dimensions of the dipoles were optimized in order to provide maximum power transfer to a rectification diode. The design essentially evolved from a simple printed center-fed dipoles without any dielectric material to off-center fed dipoles with a dielectric layer placed in the direction of the incoming energy. Conducting elements are introduced to effectively turn the planar dipoles themselves into a DC channeling network. An overall radiation to DC power conversion efficiency of 76% was obtained experimentally for normal incidence.

The chapter concludes with presenting a multi-layer EHS for electromagnetic energy harvesting using a unit cell consists of asymmetrical dipolar elements that are covered with high permittivity dielectric superstrates and backed with a grounded substrate. The proposed multi-layer dual polarizations harvester was evolved from the single layer off-center fed dipoles that are presented and tested in earlier sections. Those off-center asymmetrical dipoles in each layer were covered by a dielectric layer placed in the direction of the incoming energy forming a multi-layer harvester. The multi-layer energy harvesting array was tested for its potential to harvest at two different polarizations with the capability to channel the captured energy to rectifying diodes placed across the gaps of the dipoles replacing the resistive loads used in simulating the amount of the dissipated power. The two layers harvester were optimized by varying the spacing between the dipolar element and its superstrate thickness in order to provide maximum power transfer to the rectification diodes. The multi-layer harvester uses the advantage of the small connectors to connect the dipolar elements on a plane for each absorption layer. An overall radiation to DC power conversion efficiency of 70% was obtained for the normal incidence at $\phi = 0$ and $\phi = 90$ polarizations.

It's important to note that, to the best of my knowledge, the radiation to DC conversion efficiency achieved by the presented EHSs in this chapter are higher than what was achieved using all previous surfaces reported in the literature including metasurfaces and planar antenna arrays [56, 125]. This chapter also showed that near-unity absorption of incoming electromagnetic energy can be made possible without the use of metasurfaces. In metasurface technology, the surface impedance of the metasurface is designed to be equal to that of free space. The EHS's structures proposed here achieved near-unity absorption (for AC) without the need to meet such constraint. Unlike metasurface technology, the advantage of having fewer absorbing elements is to maximized energy density per diode, which in turn maximizes diode turn on time period and the overall efficiency.

Chapter 5

Polarization Independent Cross-Dipole Energy Harvesting Surfaces

5.1 Single Frequency Multiple Polarization EHS

In this chapter, an efficient energy harvesting surface EHS array using cross-dipole elements are introduced. The cross-dipole EHS can efficiently harvest energy at multiple polarizations. The proposed EHS is based on appreciable electrically-large cross-dipole elements that allow maximizing the power density per element. Critically, the EHS array shows efficient harvesting efficiencies that are independent of the incoming wave polarizations. Practically, the polarization independence feature is of extreme importance for energy harvesters as to increase the harvesting freedom and not to restrict the harvester with only one narrow-angle of incident. The radiation to AC efficiency for the proposed EHS was studied numerically and the radiation to DC conversion efficiencies of the fabricated EHS array rectenna system was studied experimentally. In fact, none of the available full-wave simulation tools, to the best of our knowledge, are capable of analyzing a structure that is integrated with non-linear elements. Last, the rectification mechanism is implemented directly at the same plane of the EHS harvester without the need for matching circuits. The DC channeling is also achieved for all harvesting polarizations and collected at the elements' plane.

5.1.1 Design Methodology of the EHS Unit Cell

Man-made artificial materials have recently gained special attention as they exhibit extraordinary electromagnetic responses and phenomena that cannot be achieved using the natural existing materials. The unusual electromagnetic properties of the artificial structures, such as the negative refraction [126], have inspired researchers to explore new electromagnetic paradigms. Artificial structures, such as frequency selective surfaces, metamaterials, and metasurfaces, are made of periodic elements with different geometric shapes. Invisibility cloaks [127, 128], perfect absorbers [129], and near unity electromagnetic energy harvester [80] are only a few examples that use the concept of artificial materials. The concept of near unity absorption introduced in [80] using metamaterial structure has, in particular, gained a special attention as it showed that the incident electromagnetic power can be fully dissipated on resistive loads. Majority of published work discussing metamaterial harvesters in the microwave regime are in fact metasurfaces or plannar surface harvesters as all were planar structures [77, 78, 79, 80, 81, 82, 83]. In this section, a novel surface for energy harvesting is proposed, that is neither a metamaterial nor a metasurface, that incorporates DC paths within the entire structure. In our proposed EHS structure, appreciable large elements are used, unlike the previously published metamaterial or metasurface works that strictly use electrically small elements. With our novel EHS structure, not only it was managed to have close to unity absorption, but also the rectifying circuitry was achieved along with the DC channeling at one plane.

The developed cross-dipole EHS unit cell structure is shown in Fig. 5.1. The unit cell consists of cross-dipole metallic elements sandwiched between two dielectric layers that were chosen for their low loss such that the absorbed energy dissipated mostly on resistive loads and not within the dielectric materials. A feeding/harvesting gap was created at the cross-dipole arms that contribute to the harvested energy with respect to the various polarization angles of the incident field. To achieve full energy absorption at the chosen frequency of 3 GHz while maximizing the harvesting efficiency, the EHS's unit cell occupied a square footprint's side length of 19.92 mm. This frequency was only chosen for its compatibility with our testing equipment and the setup facilities (Note: the structure can be scaled to operate at other frequencies). The dipole elements are attached to a high-permittivity Rogers TMM-13i dielectric superstrate of a thickness of $t_1 = 2.54$ mm having a dielectric constant of $\varepsilon_r = 9.8$ and a loss tangent of 0.002. The EHS is backed with a grounded low-permittivity Roger RT/duroid 5880 dielectric substrate of a thickness of $t_2 = 1.5748$ mm having a dielectric constant of $\varepsilon_r = 2.2$ and a loss tangent of 0.0009. The cross dipoles have a length and width of L = 17.54 mm W = 1.56 mm, respectively. The EHS unit cell as shown in Fig. 5.1 consists of two feeding ports of width p = 0.5 mm width and n

= 0.8 mm where resistive loads or rectifying circuitry can be placed across the gaps. A small connector of length d = 0.94 mm and width of c = 0.25 mm are used to link the harvester's cells with a spacing of s = 0.5 mm between adjacent unit cells when forming an array. A small vacuum layer of g = 0.254 mm that accounts for the hight of diodes was placed between the top and bottom dielectric layers. It is important to note here that the cross dipoles were patterned on the bottom of dielectric superstrate).

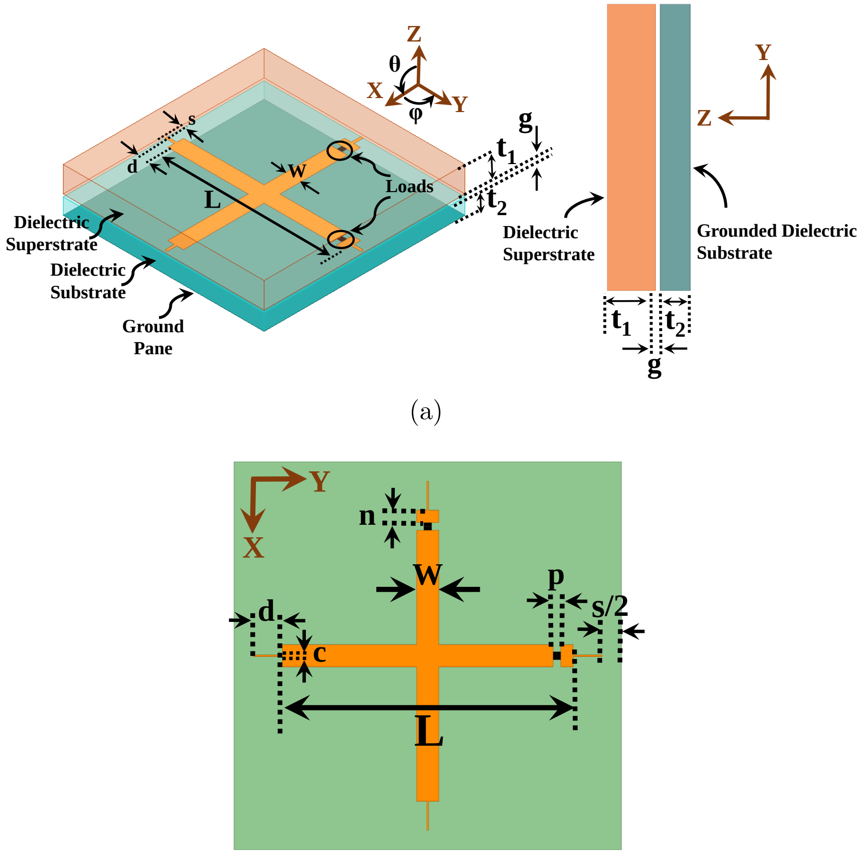

(a)

(b)

Figure 5.1: Schematic views for the proposed cross-dipole EHS unit cell. (a) Perspective view (left) with the definition of incident angles ϕ and θ and side (right) view showing the dielectric layers. (b) Top view showing the geometrical details.

All numerical results in this work were simulated using the commercially available full-wave simulator ANSYS® HEHS™ [120]. The shown EHS unit cell in Fig. 5.1 was simulated on the assumption that it lies in an infinite periodic structure with periodic boundary conditions in the $x - y$ plane [121]. Master and slave boundaries were applied on the faces parallel to the wave propagation direction ($-\hat{z}$ direction).

The input impedance of the cross dipoles needs to be analyzed for radiation to DC conversion for an optimal matching condition to a rectifying diode. In this case, lumped excitation ports were placed at the EHS feeding gaps to determine the input impedance of the cross dipoles. Then a Floquet port having a power level of 1 W was considered in the case of calculating the harvested power efficiency. The Floquet port was used to generate a plane wave illumination that propagates in the $-\hat{z}$ direction with different polarizations of ϕ angles (refer to Fig. 5.1 for the angles definition). Lumped loads that are matched to the conjugate input impedance of a rectifying diode were placed across the EHS feeding gaps. The diode impedance was determined at the maximum power absorption/harvesting frequency of 3 GHz.

The harvester's input impedance seen at the feeding gaps is critical as it determines the matching condition between the harvester and its rectifying circuitry (diodes). An input impedance that matches a diode's conjugate impedance eliminates the need for an additional layer to incorporate a matching network. The input impedance of the harvester's unit cell, as seen from the gaps, can be controlled by varying the position of the ports gap I and the connectors length (d) while keeping the length of the cross dipoles (L) and the unit cell' spacing (s) unchanged (increasing (d) may give a larger unit cell's side length). This design feature of tailoring the harvester's input impedance is important for DC conversion when placing rectifying diodes directly on the feeding gaps without a matching network.

Transmission analyses were performed to find the input impedance of the cross-dipole feeding gaps that are shown as loads in Fig. 5.1. HSMS-2860 Schottky diode was considered in this work as a rectifying element for its low turn-on voltage of 0.28 V and fast switching speed at the operating frequency of 3 GHz. The EHS harvester unit cell was carefully designed to have a conjugate input impedance at its feeding gaps to the rectifying diode. This configuration insured a direct matching between the energy harvester and the DC rectifier circuitry. The diode has an input impedance of Z_d = 202 - j46.34 Ω when terminated with a load of 300 Ω at a frequency of 3 GHz (the input impedance of the diode was obtained from its model [96]). The harvester input impedance seen at the feeding gaps is shown in Fig. 5.2. Lumped excitation ports were placed on the feeding gaps with an impedance of Z_{EHS} = 202 + j46.34 Ω which is the conjugate impedance of the diode's input impedance. Figure 5.3 shows the scattering parameters for each feeding gaps when the harvester was matched to the diode impedance where the reflection coefficients S_{11} and S_{22} show good matching at the resonance frequency of 3 GHz. The reflection coefficients S_{11} and S_{22} show that each arm of the cross-dipole structure is well matched to the chosen diode impedance. The reflection coefficients seen at each feeding gaps can be as well used here as an initial indicator that for the harvester's capability to harvest at multiple angles of polarization; however, a firm conclusion for the harvester efficiency cannot be reached without examining the harvester under electromagnetic illumination.

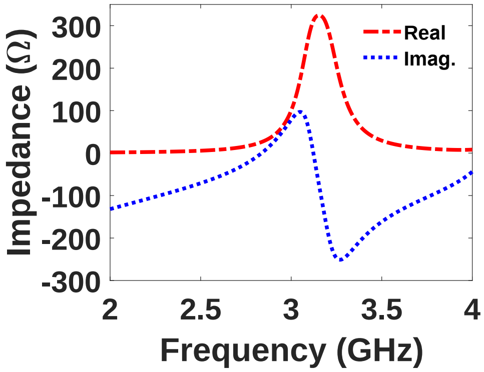

Figure 5.2: Simulation of the real and imaginary parts of the input impedance seen at the EHS unit cell's feeding gaps (Note: the input impedance seen at the EHS gaps is identical).

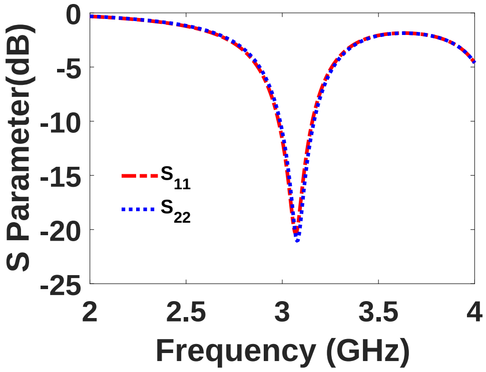

Figure 5.3: Simulation of the scattering parameters showing the reflection coefficient of the EHS's feeding gaps, S_{11} and S_{22}, when the two gaps are matched to the diode impedance Z_d = 202 - j46.34 Ω.

Next analyses were performed for the EHS unit cell under electromagnetic illuminations. These analyses allow calculating the absorption/harvesting efficiency of the EHS unit cell. Lumped loads with an input impedance of Z_d = 202 - j46.34 Ω were placed on the feeding gaps as shown in Fig. 5.1 (replacing the exciting/feeding gaps used in the transmitting analyses). The EHS was illuminated using Floquet port to generate a plane wave that propagates normally in $-\hat{z}$ direction. Floquet port's scattering parameters can be used to gauge the amount of incident power that is absorbed or reflected power by the harvester. The absorption of the unit cell is expressed as follow:

$$A(w) = 1 - |S_{11}|^2 - |S_{21}|^2 \tag{5.1}$$

In calculating the absorption by the harvester unit cell, the transmission coefficient $|S_{21}|^2 = 0$ in the above equation due to the presence of the back grounded substrate. The absorbed power by unit cell can be in a form of lost energy on either the unit cell's dipoles or the dielectric substrate, or in a form of harvested energy form dissipated on the resistive loads. The radiation to AC/DC harvested efficiency describes the ability of a harvester/absorber to capture the energy per footprint area [77]. What is referred to in this work as a radiation to AC efficiency is the efficiency of the harvester to transfer the total power incident on a specific area to available power at the feed (i.e., where a resistive load or rectifying circuitry is placed, referred to as the load location in Fig. 5.1). The radiation to AC conversion efficiency is calculated by calculating the footprint (surface area) in square meters. The Radiation to AC conversion efficiency of an energy harvester occupying a specific footprint is then given by

$$\eta_{Rad-AC} = P_{out}/P_{in} \tag{5.2}$$

where P_{in} is the total time-averaged power incident on the footprint, and P_{out} is the available time-average AC power received by the harvesters' collectors (i.e., where a resistive load or a diode rectifying circuity is placed) and is given by

$$P_{out} = \sum_{n=1}^{N} V_i^2/R_i \tag{5.3}$$

where V_i is the voltage across the resistance of the i^{th} collector, R_i and N is the total number of collectors.

This Radiation to AC efficiency definition (i.e., the harvested efficiency) is indicative of the ability of the harvester to utilize the available electromagnetic energy incident on a given area and the ability of the harvester or its collectors to deliver the absorbed energy to resistive loads. This definition provides a measure of how efficient the absorber, occupying a specific footprint, in converting the available incident microwave power to RF energy.

With the EHS cross dipoles terminated by lumped loads matched to the diode impedance, the obtained simulated absorption, reflected, lost and harvested (radiation to AC power conversion efficiency) of the EHS unit cell (assuming infinite periodicity) is shown in Fig. 5.4 for an incident plane wave traveling in $-\hat{z}$ direction with the E-field being polarized at $\phi = 0$ (refer to Fig. 5.1 for the angles definition). This result shows that the cross-dipole unit cell absorbs the incident microwave energy with a near unity absorption efficiency. A critical feature is that the EHS unit cell dissipates most of the absorbed energy across the resistive loads with a harvesting efficiency of 94% where the remaining 7% were lost on the dielectric layers.

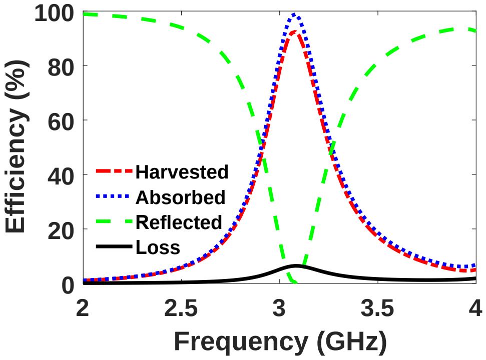

Figure 5.4: Simulation results showing the harvested (dissipated in a the resistive loads), absorbed, reflected and lost efficiencies within the EHS's unit cell when it is illuminated by a plane wave traveling in $-\hat{z}$ direction and polarized at $\phi = 0$.

The EHS unit cell was then examined for its capability of capturing the incoming radiation at different polarization angles. Here the incident plane wave illuminates the EHS normally with various angles ϕ for the E-field (refer to Fig. 5.1 for the incident angles definition). Figure 5.5 shows the simulated radiation to AC efficiencies for the EHS unit cell at various angles with normal illumination. From the simulation results, it can be observed that the cross-dipole EHS unit cell equally and efficiently harvests the incident microwave energy independent of the E-filed polarization angles with a consistent harvesting peak efficiency of 94%.

The magnitude of the electric fields and the current vectors developed on the cross dipoles were also simulated. The electric field and current were taken at the frequency of the maximum harvesting efficiency of 3 GHz with an incidence plane wave propagating in the $-\hat{z}$ direction when the E-field being polarized at $\phi = 0$, $\phi = 30$, $\phi = 60$ and $\phi = 90$ (refer to Fig. 5.1 for the angles definition).

Figure 5.6 shows significant high E-field magnitudes on the cross-dipole feeding gaps that aligned with the incident E-field polarization. The field concentrates mostly on the

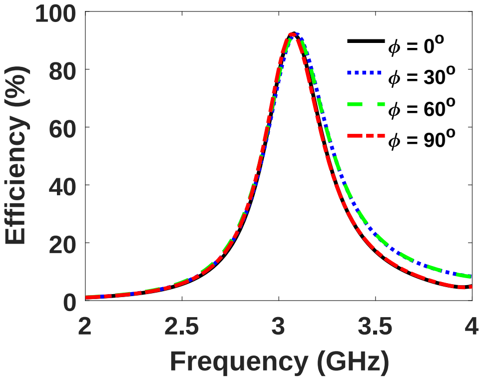

Figure 5.5: The simulated radiation to AC conversion efficiency for the EHS's unit cell when the structure was illuminated by a plane wave that is traveling in $-\hat{z}$ direction and polarized at different ϕ incident angles (refer to Fig. 5.1 for the incident angles definition).

feeding gap (only one gap) that is aligned with the electric incident field as shown in Figs. 5.6(a) and 5.6(d) for the cases of the incident electric field with $\phi = 0$ and $\phi = 90$ polarizations, respectively. However, the electric field concentration is split between the two feeding gaps for any other incident polarizations (considering only normal illuminations) as shown in Figs. 5.6(b) and 5.6(c) for the $\phi = 30$ and $\phi = 60$ polarizations, respectively.

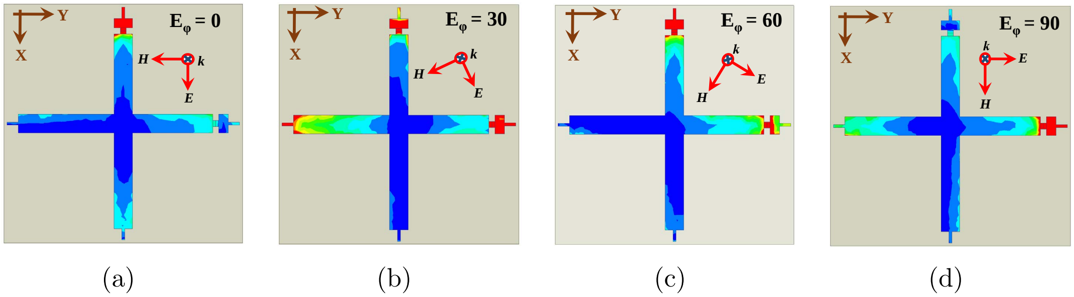

(a) (b) (c) (d)

Figure 5.6: Simulation of the electric field magnitude developed on the cross dipoles for various incident polarization angles. The electric fields were taken at the maximum absorption frequency of 3 GHz when the EHS unit cell was illuminated by a normal incident plane wave traveling in the $-\hat{z}$ direction with an E-field being polarized at (a) $\phi = 0$, (b) $\phi = 30$, (c) $\phi = 60$ and (d) $\phi = 90$ (refer to Fig. 5.1 for the angles definition). The electric field highest intensity (red) corresponds to 1×10^4 V/m and the lowest intensity (blue) corresponds to 1×10^2 V/m.

It is observed from the current vectors' simulations shown in Figure 5.7 that the current mostly flows on the cross-dipole arm that aligned with the incident E-field. In Figs 5.7(a) and 5.7(d), for instance, where the E-field was polarized on $\phi = 0$ and $\phi = 90$, the current mostly flows on the cross-dipole arm that was aligned with the incident E-field. For the other E-field polarizations, the current flows on both arms of the cross dipoles as shown in Figs. 5.7(b) and 5.7(c).

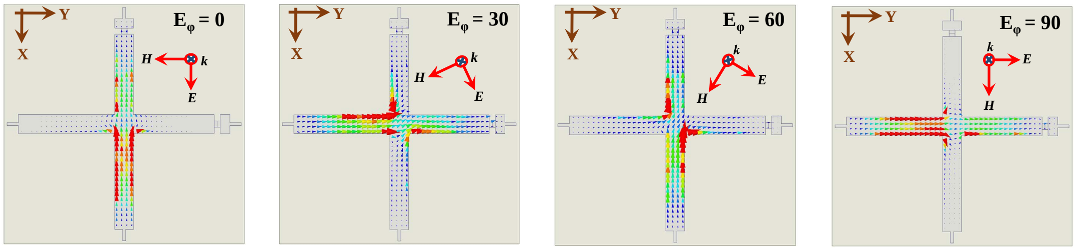

(a) (b) (c) (d)

Figure 5.7: Simulation of the surface current vector shows the current flow directions on the cross dipoles for various incident polarization angles. The currents were taken at the maximum absorption frequency of 3 GHz when the EHS unit cell was illuminated by a normal incident plane wave traveling in the $-\hat{z}$ direction with an E-field being polarized at (a) $\phi = 0$, (b) $\phi = 30$, (c) $\phi = 60$ and (d) $\phi = 90$ (refer to Fig. 5.1 for the angles definition). The surface current vectors highest intensity (red) corresponds to 2.5×10^2 A/m and the lowest intensity (blue) corresponds to 1×10^2 A/m.

Figures 5.6 and 5.7 clearly show that each feeding/harvesting gap is fully or partially contributed to the harvested energy with respect to various E-field polarizations for the incident plane wave.

5.1.2 Experimental Verification

In light of the obtained numerical results for the EHS's unit cell, a finite EHS array consist of 7×7 cross-dipole elements was fabricated as shown in Fig. 5.8. The entire array was of size 140 mm × 140 mm. The fabricated EHS array was patterned on a Rogers TMM-13i superstrate and backed with an RT/duroid 5880 grounded substrate. The feeding gaps of the cross dipoles were all terminated by Schottky diodes (recall that the EHS unit cell was designed such that the input impedance is matched to the Schottky diode impedance at the frequency of 3 GHz when terminated with a load of 300 Ω). Low loss inductors connecting the array elements were placed across the small gap between the cross dipoles (refer to Fig. 5.1 for the (s) gap locations and to Figs. 5.9(a) and 5.9(b) for the linking inductors (L) locations).

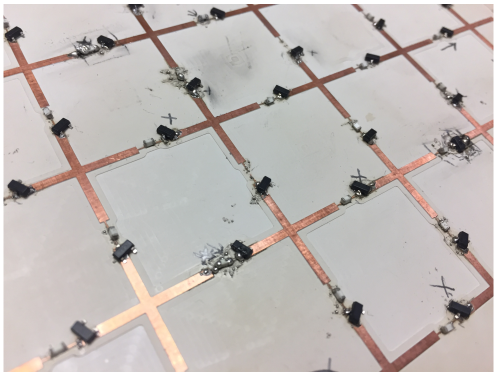

Figure 5.8: The fabricated crossed-dipole harvesting array patterned on a high-permittivity superstrate bottom view made of Rogers TMM-13i material.

It is important to realize that DC channeling can be accomplished by placing diodes directly across each cross-dipole feeding gaps (recall that the feeding gaps are matched to a diode impedance) and connecting the array elements by inductors. A schematic representing the adopted DC channeling topology is shown in Fig. 5.9 illustrating the rectifying diodes (D_x) and (D_y) that are placed across the cross-dipole feeding gaps and the AC filtering inductors (L) that are placed between every cross-dipole element. The diodes indicated as (D_x) and (D_y) rectify the ac signals when the incident E-field being polarized on $\phi = 0$ (Fig. 5.9(a)) and $\phi = 90$ (Fig. 5.9(b)), respectively. This allows the DC current to flow mostly on one arm of the cross-dipole elements. However, both the (D_x) and (D_y) diodes play a roll on the rectification mechanism for any other E-field polarizations, not from $\phi = 0$ and $\phi = 90$ of the incident field. In this case, the current flows on the two arms of the cross-dipole elements. In all cases, the voltage is collected across a load from the two positive and negative nodes as illustrated in Figs. 5.9(c) and 5.9(d).

The experiment was performed using the setup shown in Fig. 5.10(a). The measurements of the EHS array were taken in an anechoic chamber as shown in Fig. 5.10(b). The EHS energy harvesting array was illuminated by a broadband commercially available horn antenna (0.7 GHz to 18 GHz frequency range with a maximum gain of 14.71 dBi) placed at a distance of 1 m from the harvester to insure a plane wave illumination. The broadband horn antenna was excited by a Keysight signal generator (a maximum power and frequency of 25 dBm and 6 GHz, respectively) through a 42 dB Mini-Circuits High Power

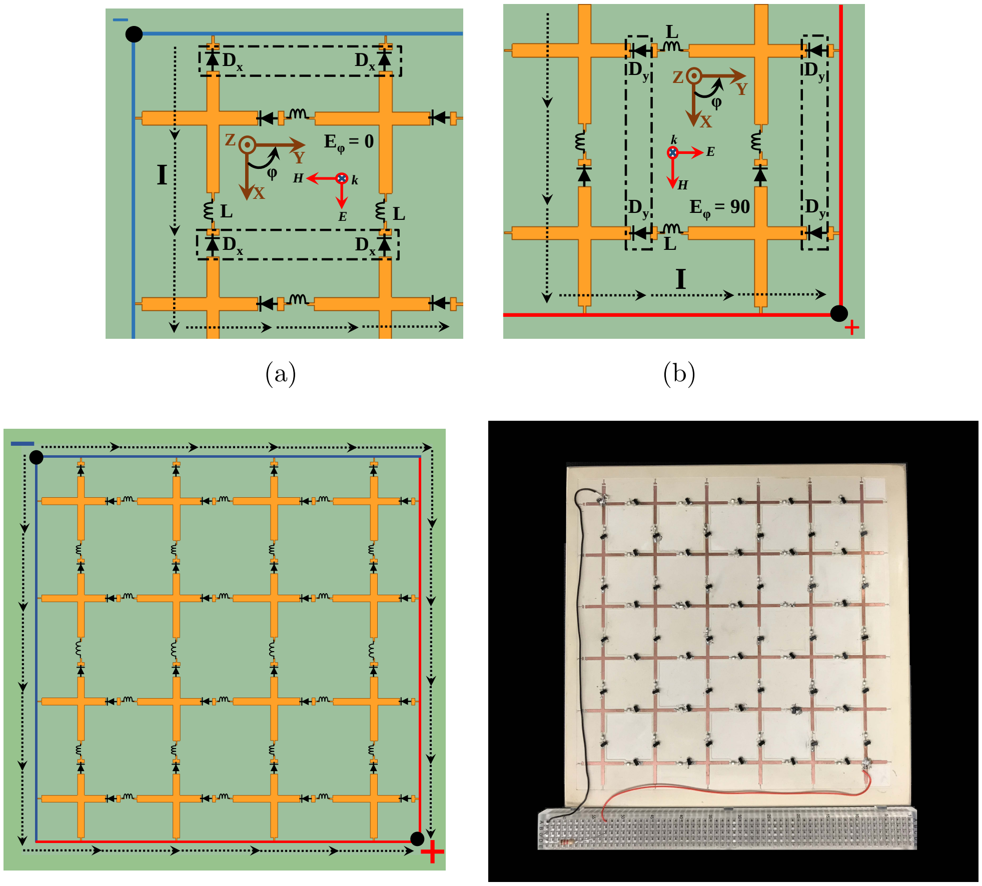

(a) (b)

(c) (d)

Figure 5.9: Schematics of the cross-dipole EHS array looking from the bottom showing the DC channeling configuration and the flow of the DC current (I). The diodes designated as D_x and D_y are turned on when the illuminated plane wave is polarized with an E-field at (a) $\phi = 0$, (b) $\phi = 90$. L is the AC filtering inductor connecting the cross-dipole EHS cells and (c) is a sample schematic for a 4×4 cross-dipole EHS array showing the DC channeling. (d) The fabricated 7×7 cross-dipole EHS is made ready for DC measurement.

Amplifier ZHL-16W-43-S (refer to the measurement setup shown in Fig. 5.10(a)). The harvested voltage across a load connected between the EHS array two polarity nodes (refer to Fig. 5.9) was measured using a multimeter in which the harvested power was calculated, P_{out}. The following formula was then employed to calculate the power provided by the

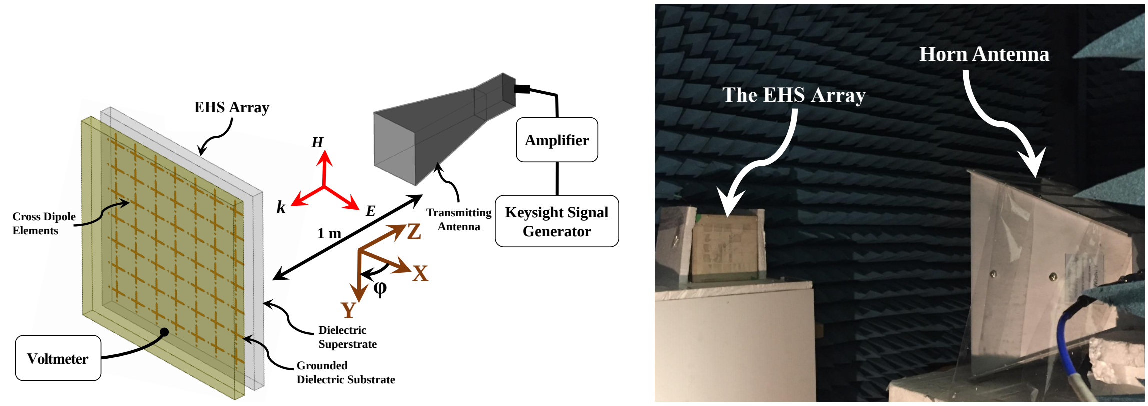

(a) (b)

Figure 5.10: (a) Schematic showing the measurement setup for the planar dipole array energy absorber covered with a dielectric superstrate under illumination by a transmitting horn antenna. (b) The EHS under illumination by a broadband horn antenna for DC measurements inside an anechoic chamber.

horn antenna at the EHS plane (P_{in}):

$$P_{in} = A \times P_t, \tag{5.4}$$

where

$$P_t = \frac{P}{4\pi R^2} G_t(f) \tag{5.5}$$

A is the harvester surface area (footprint), P_t is the radiated power density generated by the horn at the harvester surface plane in the absence of the harvester, and P is the power fed to the transmitting horn's input terminal. $G_t(f)$ is the gain of the horn antenna as a function of frequency and R is the distance between the horn antenna and the array. The available power at the absorber plane, P_{in}, was then calculated from which the overall power absorption of the array can be obtained using Equation 5.2.

The fabricated EHS harvesting array shown in Fig. 5.9 was illuminated by the horn antenna in $-\hat{z}$ direction as shown in Fig. 5.10. The load impedance and power at the receiving end were swept at the highest harvesting frequency of 3 GHz. The purpose of these sweeps were to find the optimal DC load and input power that will deliver maximum power across the load. Figures 5.11(a) and 5.11(b) show that the harvesting surface achieves maximum power across the load when illuminated by a power level of 40 mW (i.e., the available power at the harvester plane, P_{in}) with a load of 0.6 kΩ for $-\hat{z}$ illumination when the incident E-field was polarized on $\phi = 0$. These operating load and power level were considered as the optimal condition and were used for all other measured incident polarizations.

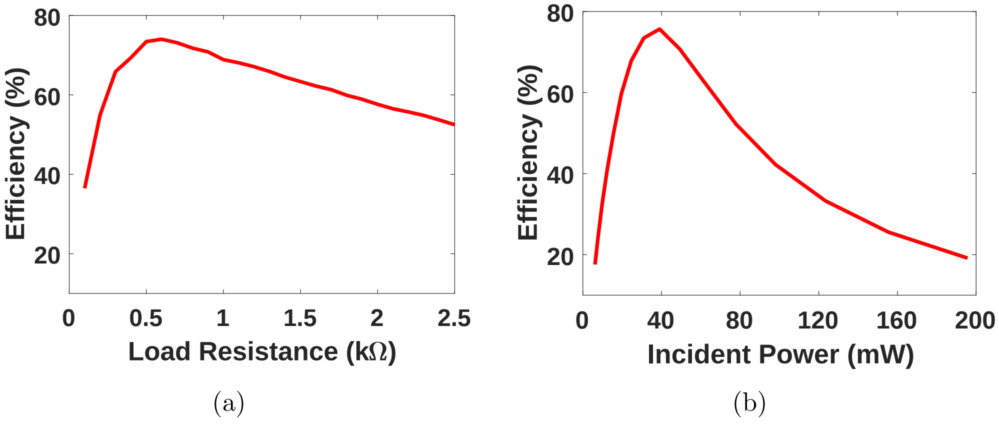

(a)

(b)

Figure 5.11: The measured DC absorption as a function of (a) the load impedance and (b) the available power at the absorber plane P_{in} when the structure is illuminated by a horn antenna transmitting waves propagating in ($-\hat{z}$) direction when the E-field is polarized along $\phi = 0$.

The DC harvesting efficiency for the illumination in the $-\hat{z}$ direction was then recorded at multiple frequency points at which the harvested power had maximum power across the load (i.e., with the optimal obtained input power and load). The EHS harvesting array was then tested for capturing the incoming radiation at various angles of E-field polarizations. Fig. 5.12 shows the measurement radiation to DC efficiencies for various angels of E-field (ϕ angles) polarizations when the harvester illuminated normally in the ($-\hat{z}$) direction (i.e.; $\theta = 0$). These measurement results prove the capability of the EHS for capturing the incident energy for all incident polarizations with a maximum efficiency of 74% at the designed operating frequency of 3 GHz. The shown measurement results in Fig. 5.12 are nicely agreed with the obtained simulation results. It is critical to realize the EHS captures the incident energy efficiently with one optimal load for all incident polarizations. This is evidence that EHS sees the incoming wave equally and that its response irrespective and independent of its polarization.

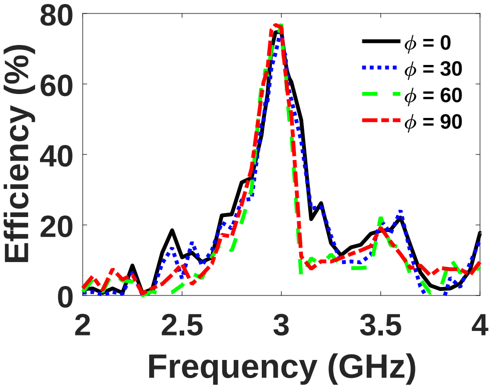

Figure 5.12: The measured radiation to DC conversion efficiencies for the EHS harvesting array when the structure was illuminated by a plane wave generated by a horn antenna transmitting waves propagating in $(-\hat{z})$ direction and polarized at various ϕ angles for the incident E-field (refer to Fig. 5.1 for the incident angles definition).

5.2 Dual-Band Multilayer Energy Harvesting Surface

This section introduces an efficient dual-band EHS array using two stacked-layer of cross-dipole elements that can efficiently harvest at two frequency bands for multiple polarizations. The proposed EHS array introduces the concept of using stacked layer harvesting surfaces that were directly integrated with rectification circuitry. The EHS layers are based on electrically-large cross-dipole like elements that allow maximizing the power density per element at the desired harvesting frequency band. The radiation to AC efficiency for the proposed EHS layers was studied numerically. While the layers of the EHS structure contributed collectively to the total harvesting efficiency, each layer, in fact, was destined such that it was mostly responsible for harvesting one desired frequency band. This critical feature allows for separately matching each EHS layer with its own rectification circuity at its desired harvesting frequency band. Another feature is that the rectification mechanism was implemented directly on each layer in its own plane without the need for matching circuits. It is valuable to point out that since full-wave simulation tools are not capable to analyze nonlinear elements integrated with passive structures, only measurement results were presented for the ac to DC harvesting efficiencies for the manufactured EHS layers. The DC channeling was also achieved for the multilayer EHS structure such that it is collected at the elements' plane for each layer where the total achieved harvested DC power is the collective contribution of the rectified DC power from the EHS layers.

5.2.1 Design Methodology of the Mulit-layer EHS Unit Cell

The multi-layer cross-dipole EHS unit cell structure is shown in Fig. 5.13. The unit cell consists of two stacked layers of cross-dipole metallic elements backed with a grounded substrate. The cross-dipole elements in each layer are sandwiched between two dielectric layers that were chosen for their low loss such that the absorbed energy dissipated mostly on resistive loads and not within the dielectric materials. Two Feeding/harvesting gaps were introduced on the arms' of each cross-dipole layer allowing to harvest from various polarization angles of the incident field. Resistive loads or rectifying circuitry are embedded within these feeding/harvesting gaps such that the incident radiation is fully or mostly dissipated on the loads or rectified to DC power. To achieve full energy absorption at two frequency bands of 2.5 GHz and 3.5 GHz while ensuring that most of the absorbed energy is efficiently harvested, the multilayer EHS's unit cell occupied a square footprint's side length of 21.78 mm. This frequency again was chosen for its compatibility with our testing equipment and the setup facilities (Note: the structure can be scaled to operate at other frequencies). The stacked layers were ordered with respect to the operational frequency bands such that the top layer is responsible for harvesting the upper-frequency band of 3.5 GHz whereas the bottom layer is responsible to harvest the lower frequency band of 2.5 GHz. The dipole elements in each layer are attached to a high-permittivity Rogers TMM-13i dielectric superstrate of a dielectric constant of $\varepsilon_r = 9.8$ and a loss tangent of 0.002. The top and bottom layers are having thicknesses of $t_1 = 1.27$ mm and $t_2 = 1.905$ mm, respectively. The multilayer EHS structure is backed with a grounded low-permittivity with a thinness of $t_3 = 1.5748$ mm made of Roger RT/duroid 5880 dielectric substrate having a dielectric constant $\varepsilon_r = 2.2$ and a loss tangent of 0.0009. The cross dipoles have a length and width of $L_1 = 8.91$ mm $W_1 = 2.45$ mm for the top layer and $L_2 = 16.85$ mm $W_1 = 1.43$ mm for the bottom layer. Each EHS layer as shown in the unit cell shown in Fig. 5.13(a)) consists of two feeding ports of width p = 0.5 mm and n = 0.8 mm where resistive loads or rectifying circuitry can be embedded in the feeding/harvesting gaps. Small connectors of a fixed width c = 0.25 mm and length of $d_1 = 5.53$ mm and $d_2 = 1.56$ mm are used to link the harvester's cells for the top and bottom layer, respectively. Spacings of s = 0.5 mm are kept constant between adjacent unit cells that are allocated to place filtering inductors when linking the unit cells to form an array structure. Small vacuum layers of g = 0.254 mm that account for the hight of diodes were introduced between the dielectric layers. It is important to note here that the cross dipoles were patterned on the bottom of dielectric layer such the incoming wave sees first dielectric layers that act as superstrates above the cross dipoles. All numerical results presented in this section were also simulated using the commercially available full-wave simulator ANSYS® HEHS™. The two stacking layer of the cross-dipole EHS unit cells shown in Fig. 5.13 was simulated

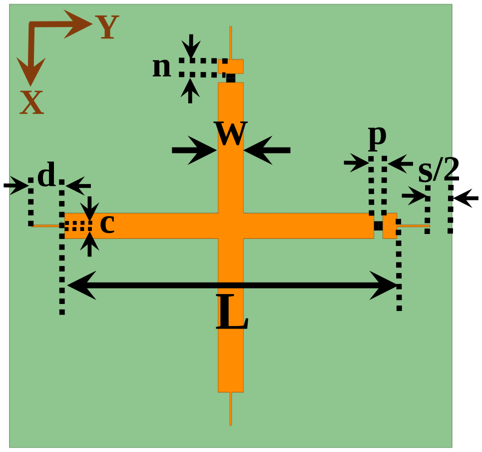

(a)

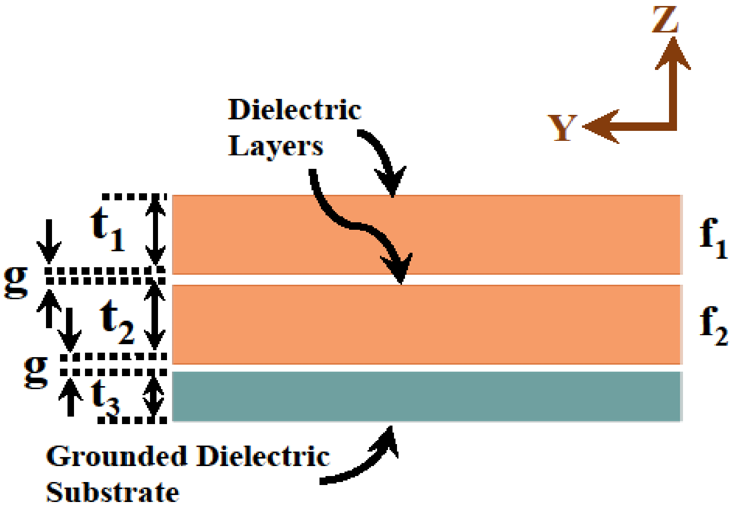

(b)

Figure 5.13: Schematic views for the proposed multilayer cross-dipole EHS unit cell. (a) Top view showing the geometrical details. (b) Side view of the multilayer cross-dipole EHS stacked dielectric layers.

on the assumption that it lies in an infinite periodic structure with periodic boundary conditions in the $x-y$ plane [121]. Master and slave boundaries were applied on the faces parallel to the wave propagation direction ($-\hat{z}$ direction).

As the multilayer EHS is operating at two frequencies, lumped loads were placed on the feeding gaps with an input impedance of Z_{d1} = 220 - j50.34 Ω at the lower layer that operates at 2.5 GHz and Z_{d2} = 270 - j40.22 Ω for the top layer that is responsible for harvesting at 3.5 GHz (replacing the exciting/feeding gaps used in the transmitting analyses). The EHS was illuminated using Floquet port to generate a plane wave that propagates normally in $-\hat{z}$ direction. Floquet port's scattering parameters can be used to gauge the amount of incident power that is absorbed or reflected power by the harvester. With the multilayer EHS cross dipoles terminated by lumped loads matched to the diodes' impedance, the obtained simulated absorption, reflected, losses and harvested (radiation to AC power conversion efficiency) of the EHS unit cell (assuming infinite periodicity) is shown in Fig. 5.14 for an incident plane wave traveling in $-\hat{z}$ direction with the E-field being polarized at $\phi = 0$ (refer to Fig. 5.1 for the angles definition). This result shows that the multilayer cross-dipole unit cell absorbs the incident microwave energy with a high absorption efficiency and is peaked at multiple frequencies of 2.5 GHz and 3.5 GHz.

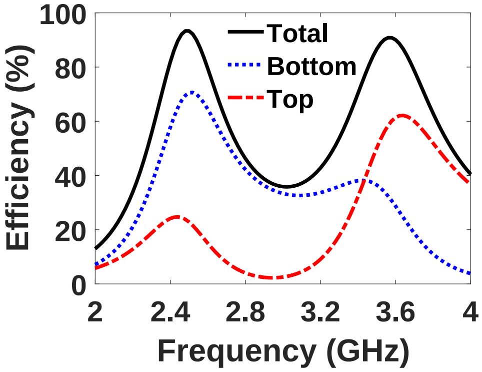

Figure 5.14: Simulation results showing the harvested efficiencies of the multilayer EHS's unit cell when it is illuminated by a plane wave traveling in $-\hat{z}$ direction and polarized at $\phi = 0$.

Similar to the single frequency EHS, the multilayer EHS unit cell was then examined for its capability of capturing the incoming radiation at different polarization angles. Here the incident plane wave illuminates the EHS normally with various angles of ϕ and θ (refer to Fig. 5.1 for the incident angles definition). Figure 5.15 shows the simulation radiation to AC efficiencies for the EHS unit cell at various angles with normal illumination. From the simulation results, it can be observed that the multilayer cross-dipole EHS unit cell efficiently harvests the incident microwave energy at multiple polarizations.

The magnitude of the electric fields and the current vectors developed on the cross dipoles are then simulated. The electric field and current were taken at the frequency of

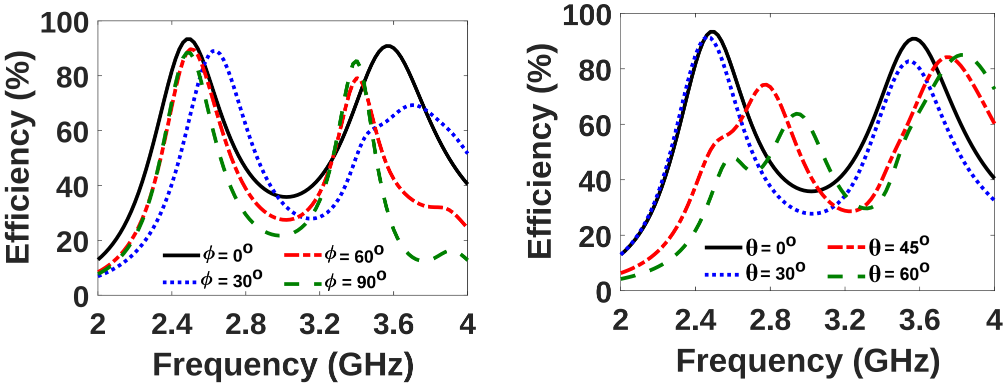

(a) (b)

Figure 5.15: The simulated radiation to AC conversion efficiency for the multilayer EHS's unit cell when the structure was illuminated by a plane wave traveling in $(-\hat{z})$ direction and polarized at (a) different ϕ incident angles when θ is 0 and (b) various θ angles when ϕ angle is 0 (refer to Fig. 5.1 for the incident angles definition).

the maximum harvesting efficiency of 2.5 GHz and 3.5 GHz with an incidence plane wave propagating in the $-\hat{z}$ direction when the E-field being polarized at $\phi = 0$ and $\phi = 90$ for each peaking harvesting frequency(refer to Fig. 5.1 for the angles definition). Figure 5.16 and Figure 5.17 show significant high E-field magnitudes on the cross-dipole feeding gaps that aligned with the incident E-field polarization for each layer. For instance, the E-field at each layer is maximized with respect to layer's operating/harvesting frequency and is concentrated mostly on the feeding gap (only one gap) that aligns with the electric incident field for the top layer that operates at 3.5 GHz as shown in Figs. 5.16(c) and 5.16(a) for $\phi = 0$ and $\phi = 90$ polarizations.

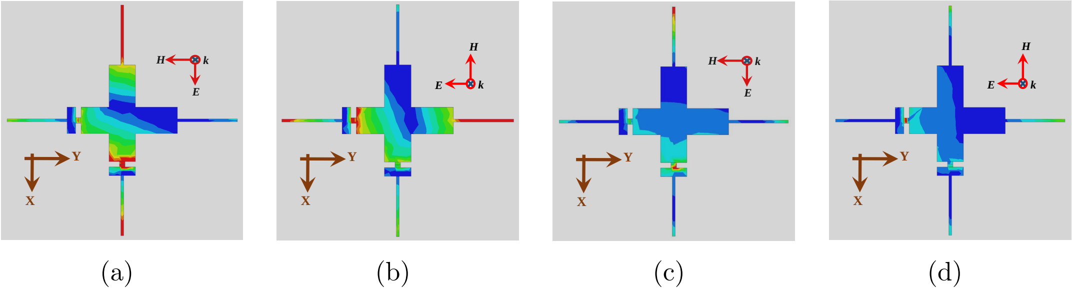
(a) (b) (c) (d)

Figure 5.16: Simulation of the electric field magnitude developed on the cross-dipoles unit cell that is responsible for harvesting at 3.5 GHz (top layer) for two incident polarization angles. The electric fields were taken at its maximum absorption frequency of 3.5 GHz when the EHS unit cell was illuminated by a normal incident plane wave traveling in the $-\hat{z}$ direction with an E-field being polarized (a) $\phi = 0$, (b) $\phi = 90$, and at the other harvesting frequency of the second layer (bottom layer) at 2.5 GHz at (c) $\phi = 0$ and (d) $\phi = 90$ (refer to Fig. 5.1 for the angles definition). The electric field highest intensity (red) corresponds to 1×10^4 V/m and the lowest intensity (blue) corresponds to 1×10^2 V/m.

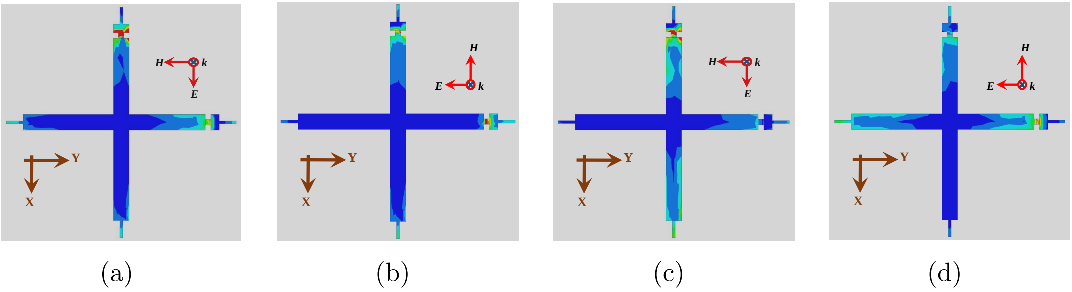
(a) (b) (c) (d)

Figure 5.17: Simulation of the electric field magnitude developed on the cross-dipoles unit cell that is responsible for harvesting at 2.5 GHz (bottom layer) for two incident polarization angles. The electric fields were taken at the maximum absorption frequency of 3.5 GHz when the EHS unit cell was illuminated by a normal incident plane wave traveling in the $-\hat{z}$ direction with an E-field being polarized at (a) $\phi = 0$, (b) $\phi = 90$, and at the other harvesting frequency of the first layer at 3.5 GHz (top layer) at (c) $\phi = 0$ and (d) $\phi = 90$ (refer to Fig. 5.1 for the angles definition). The electric field highest intensity (red) corresponds to 1×10^4 V/m and the lowest intensity (blue) corresponds to 1×10^2 V/m.

5.2.2 Experimental Verification

In light of the obtained numerical results for the EHS's unit cell, a finite EHS array consist of 7 × 7 multilayer cross-dipole elements was fabricated as shown in Fig. 5.18. The entire array was of size 140 mm × 140 mm. The fabricated EHS array layers were patterned on a Rogers TMM-13i superstrate and backed with an RT/duroid 5880 grounded substrate. The feeding gaps of the cross dipoles were all terminated by Schottky diodes (recall that the EHS unit cell was designed such that the input impedance is matched to the Schottky diode impedance at the two absorption frequencies of 2 GHz and 3 GHz when terminated with a load of 300 Ω). Low loss inductors connecting the array elements were placed across the small gap between the cross dipoles.

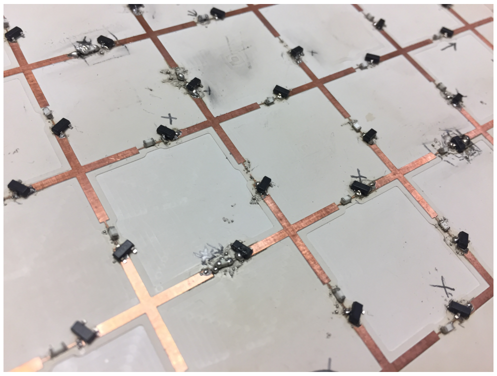

Figure 5.18: The fabricated bottom view of the crossed-dipole harvesting array patterned on a high-permittivity superstrate made of Rogers TMM-13i material.

Similar to the above single frequency structure, the DC channeling can be accomplished here by placing diodes directly across each cross-dipole feeding gaps (recall that the feeding gaps are matched to a diode impedance) and connecting the array elements by inductors. Refer to Fig. 5.9 for the schematics that represent the adopted DC channeling topology illustrating the rectifying diodes (D_x) and (D_y) that are placed across the cross-dipole feeding gaps and the ac filtering inductors (L) that are placed between every cross-dipole element. The output DC voltages form each layer are then connected and summed. The experiment was performed considering the setup provided in Fig. 5.10(a). The fabricated EHS harvesting array shown in Fig. 5.18 was illuminated by the horn antenna in $-\hat{z}$ direction. The load impedance and power at the receiving end were swept at the highest harvesting frequency of 2.5 GHz (only this frequency was considered to find the optimal operation). The purpose of those sweeps was to find the optimal DC load and input power that will deliver maximum power across the load. Fig. 5.19 show that the harvesting surface achieves maximum power across the load when illuminated by a power level of 20 mW (i.e., the available power at the harvester plane, P_{in}) with a load of 1.2 kΩ for $-\hat{z}$ illumination when the incident E-field was polarized on $\phi = 0$ (only this polarization was considered to find the optimal operation). This determined optimal operating load and power level were considered as the optimal condition and used on the all other measured incident polarizations.

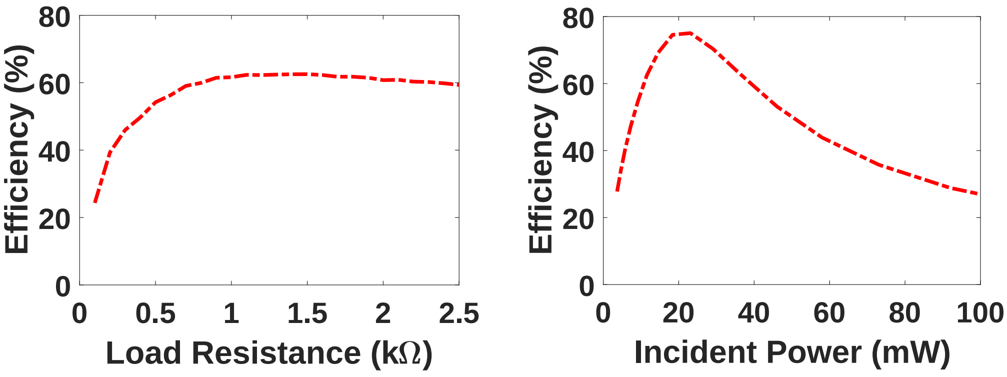

(a)

(b)

Figure 5.19: The measured DC absorption as a function of (a) the load impedance and (b) the available power at the absorber plane P_{in} when the structure is illuminated by a horn antenna in the $(-\hat{z})$direction when the E-field polarized along $\phi = 0$.

The DC harvesting efficiency for the illumination in the $-\hat{z}$ direction was then recorded at multiple frequency points at which the harvested power had maximum power across the load. The multilayer cross-dipole EHS array was then tested for capturing the incoming radiation at two angles of E-field polarizations. Fig. 5.20 shows the measurement radiation to DC efficiencies for two angels of E-field (ϕ angles) polarizations when the harvester illuminated normally in the $(-\hat{z})$ direction (i.e.; $\theta = 0$). These measurement results prove the capability of the multilayer EHS for capturing the incident energy for the two transmitted polarizations with a maximum efficiency of 77% and 70%, respectively, at $\phi = 0$ and 90 polarization angles at the desired operating frequencies of 2.7 GHz and 3.4 GHz. The shown measurement results in Fig. 5.20 are nicely agreed with the obtained simulation results.

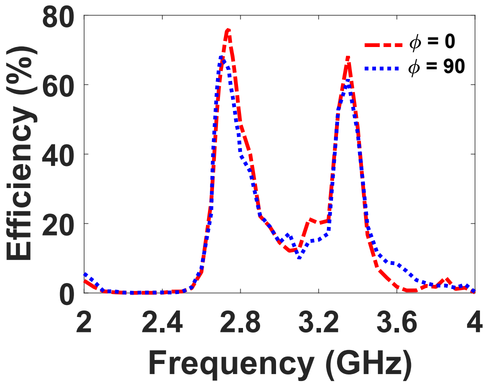

Figure 5.20: The measured radiation to DC conversion efficiencies for the EHS harvesting array when the structure was illuminated by a plane wave generated by a horn antenna traveling in $-\hat{z}$ direction and polarized at $\phi = 0$ and 90 for the incident E-field (refer to Fig. 5.1 for the incident angles definition).

5.3 Discussion

It is important to note that the infinite unit cell simulation results are carried out to fabricate the finite array EHS shown in Fig. 5.8. The fact that the aim of this work is to build a finite array energy harvester, but only a single unit cell of the proposed EHS was analyzed considering a periodic boundary [121] to simulate an infinite array structure in the $x - y$ plane of the proposed harvester shown in Fig. 5.1 and in Fig. 5.13 for the dual-band multilayer EHS structure. This can be justified as follows: a unit cell positioned in the middle of a large array is expected to behave highly similar to a unit cell placed in an infinite array which in turn increases the computational efficiency. A clear distinction between what it meant by the absorption and harvesting terms needs to be addressed here. In an absorption structure, the main goal is to maximize the absorption of the incoming energy within the structures irrespective of where this absorbed energy is dissipated and that this occurs with very minimum transmission and/or reflection. On the other hand, an efficient electromagnetic energy harvester must absorb all the energy from the incoming wave and deliver the most portion of this absorption to resistive loads where it can be converted to a usable DC power. In other words, a good harvester may qualify as an absorber, but not vice versa.

The proposed EHS experiences a near to unity absorption efficiency for the incoming electromagnetic energy with a harvesting efficiency of 94% as indicated in Fig. 5.4. This harvested amount of the incoming energy, which is the dissipated amount of power in resistive loads, has been made ready for DC conversion by considering a direct matching to rectifying elements. For more insight, cross sections of the Poynting vector for the scattered field are shown in Fig. 5.21 when the incident plane wave has an E-field polarized at $\phi = 0$. It is clearly illustrated form the Poynting vector arrows in Figs. 5.21(a) and 5.21(b) that the incident energy is mostly dissipated across the resistive loads with minimal reflections, whereas the EHS reflects all energy away from its surface at a frequency of 2 GHz as shown in Fig. 5.21(c), away from the frequency that corresponds to the EHS's highest harvesting efficiency. It is of importance to emphasize here that the partial reflection (red arrows) shown for the finite array in Fig. 5.21(a) is expected for small array with a little number of elements compared to no reflection with high power intensity towards the feeding gaps for the infinite case shown in Fig. 5.21(b). The reflection on the finite array can be due to the less in inhomogeneity of the surface exciting current for the finite array with this number of elements in contrast to the infinite case assuming infinite periodicity. These figures are evidence that most incoming energy is absorbed by the EHS with minimum scattering at the harvester operating frequency.

The Poynting vector for the scattered field of the dual-band multilayer EHS structure are shown in Fig. 5.22. Fig. 5.22(a) which is taken at 2.5 GHz shows how the power directly flows and maximize at the lower layer that was responsible to operate at this particular frequency. Similarly for the top layer, Fig. 5.22(b) shows that the power all channeled to in the top layer's feeding at its harvesting frequency of 3.5 GHz.

A critical feature for the proposed EHS array is that it was configured such that the rectenna system (antenna or harvester + rectifier) converts the harvested AC power to a usable DC power on the same plane of the cross-dipole elements. The EHS harvesting array eliminates the need for adding an AC or DC matching networks or a fabrication of vias that required an additional metalization layer for a rectification purpose. The energy is directly channeled to the desired loads where each element was made ready to be terminated by diodes replacing the resistive loads (recall the EHS unit cell shown in Fig. 5.1 where each element has to terminated loads). This design feature allows channeling the harvested energy, at any polarizations, to the desired load from two nodes indicated as positive and negative polarity nodes shown in Fig. 5.9.

Also, inductors connecting the array elements play a major rule (refer to Fig. 5.9) as they act as an open circuit on the high frequencies (microwaves) and as a short circuit in DC (very low frequencies $\backsimeq$ 50 Hz). This configuration allows to filter out the AC components and to smooth the DC signals. These inductors must have a way far self-resonance ($\backsimeq$ 30 GHz) from the EHS operating frequency of 3 GHz such that they don't interfere with harvesting signals (frequencies). Moreover, It is important to realize that the high radiation to AC conversion efficiency (94%) was achieved using cross-dipole elements

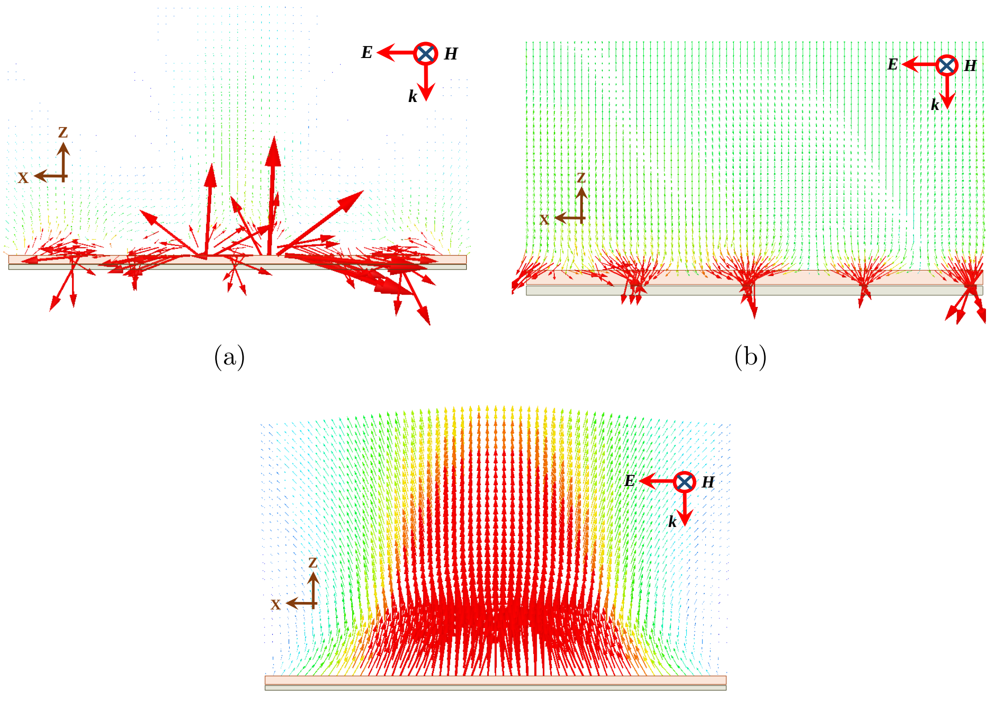

(a)

(b)

(c)

Figure 5.21: The simulated Poynting vector over a cross section sheet in the x-z plane of the cross-dipole EHS harvesting array when the the the structure is illuminated by an incident plane wave traveling in $-\hat{z}$ direction with an E-field being polarized at $\phi = 0$ at the harvester operating frequency of 3 GHz for (a) a finite EHS array of 7×7 elements and (b) for an infinite array assuming infinite periodicity. (C) At 2 GHz which is a frequency far away from the harvesting frequency for a finite EHS array of 7×7 elements. The Poynting vectors highest intensity (red) corresponds to 1×10^3 W/m^2 and the lowest intensity (blue) corresponds to 0 W/m^2.

of electric lengths larger than the electrically small metamaterial or metasurface particles used earlier [77, 80, 82, 83]. This achievement minimizes the number of required rectifiers per footprint which means a more power density is acquired by each rectifier.

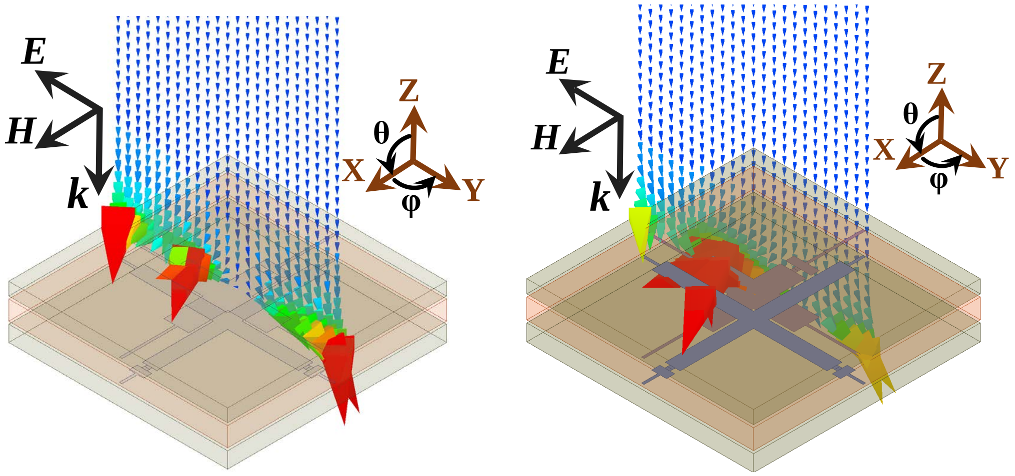

(a) (b)

Figure 5.22: The simulated Poynting vector over a cross section sheet in the x-z plane of the multilayer cross-dipole EHS harvesting array when the the the structure is illuminated by an incident plane wave traveling in $-\hat{z}$ direction with an E-field being polarized at $\phi = 0$ at the harvester two operating frequencies of (a) 2.5 GHz and (b) 3.5 GHz. The Poynting vectors highest intensity (red) corresponds to 1×10^3 W/m^2 and the lowest intensity (blue) corresponds to 0 W/m^2.

5.4 Conclusion

An EHS is presented that is efficiently capable of harvesting energy independent of the incoming wave polarizations. An extension work was done by introducing an appreciable electrically-large element as I introduced earlier in [124] which can harvest efficiently without the need to use metamaterial or metasurface's structures. An EHS unit cell consists of two feeding gaps was designed and analyzed for maximizing the radiation to AC harvesting efficiency at multiple polarizations. An array of 7×7 cross-dipole elements was then fabricated based on the simulated results. Rectifying diodes were then placed at each cross-dipole element feeding gap to covert the collected ac power to DC. The array elements are linked by inductors to channel the converted DC power. This converted DC power of any incoming polarizations was then channeled to a load for measuring the radiation to DC conversion efficiency. The obtained measurement results agree nicely with the simulated ones considering the losses that accumulate from the rectifying diodes with a radiation to DC efficiency of 74% over all polarizations. More importantly, the proposed EHS harvesting array was capable to capture the incoming energy from various polarizations.

Extension to the single harvesting frequency was presented introducing the concept of stacking EHS layers to harvest at multiple frequencies. An efficient dual-band EHS array using two stacked-layer of cross-dipole elements that can efficiently harvest at two frequency bands for multiple polarizations is presented. A finite multilayer array of 7×7 unit cells was fabricated and tested experimentally. The experimental results of the dual-band EHS energy harvesting array show an overall radiation to DC harvesting efficiencies of 77% and 70%, respectively, at two polarization angles at the desired operating frequencies of 2.7 GHz and 3.4 GHz. Another feature is that the rectification mechanism was implemented directly on each layer in its own plane without the need for matching circuits. It is valuable to point out that since full-wave simulation tools are not capable to analyze nonlinear elements integrated with passive structures, only measurement results were presented for the AC to DC harvesting efficiencies for the manufactured EHS layers. The DC channeling was also achieved for the multilayer EHS structure such that it is collected at the elements' plane for each layer where the total achieved harvested DC power is the collective contribution of the rectified DC power from the EHS layers.

Chapter 6

Accomplished and Future Work

6.1 Accomplished Work

The following list summarizes the work accomplished in this thesis:

1. Introducing the use of DRAs in an array form to efficiently build energy harvesting system in the microwave regime considering the fabrication challenges of such antennas (**Chapter 3**).
2. Provide solutions to minimize the fabrication complexity of designing DRA array for EH's purposes by proposing a complementary design DRA (**Chapter 3**).
3. Obtain a near-unity absorption of the incoming electromagnetic energy without the use of metasurfaces or metamaterials. (**Chapter 4 & 5**).
4. Achieved a near-unity absorption deleivered to designated loads (radiation to AC) for multiple polarizations. (**Chapter 4 & 5**).
5. Eliminate the need to integrate extra layers for AC feeding network, DC channeling, or DC rectifying circuitry (**Chapter 4 & 5**).
6. Proposed a planar surface EHS structures based on printed circuit board with rectification and channeling mechanisms that places the rectification diode on the same layer of the EHSs' elements. (**Chapter 4 & 5**).

7. Maximize the power density seen by the rectifying diodes to increase the turn-ON period time of the rectifying circuity. (**Chapter 4 & 5**).

8. Propose the concept of using multi-layering EHSs to operate the WPT and EH systems at multiple frequencies (**Chapter 5**).

9. Propose a dual-band cross-dipole EHS array with an overall radiation to DC harvesting efficiencies of 77% and 70%, respectively, at two polarization angles at the desired operating frequencies of 2.7 GHz and 3.4 GHz (**Chapter 5**).

6.2 List of Publications

[1] Ahmed Z. Ashoor and O. M. Ramahi. Polarization independent cross-dipole energy harvesting surface. *IEEE Transactions on Microwave Theory and Techniques*, 2018 **(submitted-Under second review)**.

[2] Ahmed Z. Ashoor and O. M. Ramahi. Mulit-Polarization planar dipole array surface for electromagnetic energy harvesting and wireless power transfer. *IEEE EuCAP 2018 Conference*, 2018 **(Accepted)**.

[3] Ahmed Z. Ashoor and O. M. Ramahi. A planar dipole array with high-permittivity superstrate for efficient electromagnetic wireless energy harvesting. *IEEE Antennas and Propagation & USNC/URSI National Radio Science Meeting, 2017 IEEE International Symposium*, 2017 **(Published)**.

[4] Ahmed Z. Ashoor and O. M. Ramahi. On the cause of radiation from dielectric resonator antennas. *IEEE Antennas and Propagation & USNC/URSI National Radio Science Meeting, 2017 IEEE International Symposium*, 2017 **(Published)**.

[5] Ahmed Z. Ashoor, Thamer S. Almoneef and O. M. Ramahi. A planar dipole array surface for electromagnetic energy harvesting and wireless power transfer. *IEEE Transactions on Microwave Theory and Techniques*, 2017 **(Published)**.

[6] Ahmed Z. Ashoor and O. M. Ramahi. Electromagnetic energy harvesting using dielectric resonator antenna. *IEEE Antennas and Propagation & USNC/URSI National Radio Science Meeting, 2016 IEEE International Symposium*, 2016 **(Published)**.

[7] Ahmed Z. Ashoor and O. M. Ramahi. Dielectric resonator antenna arrays for microwave energy harvesting and far-field wireless power transfer. *Progress in Electromagnetic Research*, 2015 **(Published)**.

[8] O. M. Ramahi, Thamer S. Almoneef, Babak Alavikia and Ahmed Z. Ashoor Metasurfaces for Far-Field Wireless Power Transfer. *Metamaterial Conference*, 2015 **(Published)**.

[9] O. M. Ramahi and Ahmed. Z. Ashoor. Dielectric resonator antennas and arrays for electromagnetic energy harvesting. *US Provisional Patent Application No. 62035265* **(Patented)**.

[10] Ahmed Z. Ashoor, Zhao Ren Omar M. Ramahi.. Localization of Buried Object Using Back Propagation Artificial Neural Networks. In *Antennas and Propagation Society International Symposium (APSURSI), 2012 IEEE*, 2012 **(Published)**.

6.3 Future Work

1. **Study and analyze** a wide-band rectifying circuity that can be implemented with the presented EHS structures to increase the bandwidth of the harvesting frequencies.
2. **Build and analyze** designing models for the stacking layers' concept to increase the number of operating and harvesting frequencies which will result to increase the harvesting bandwidth.
3. **Extend** the concept presented in **Chapter 4 & 5** for the appreciably electrically-large elements harvesting from the microwave to the THz regime. This will allow building harvesting structures operating at the infrared regime.
4. **Study and analyze** the electromagnetic property of the materials to further develop highly efficient wireless power transfer system operating at the infrared regime.

References

[1] Bernd Strassner and Kai Chang. Microwave power transmission: Historical milestones and system components. *Proceedings of the IEEE*, 101(6):1379–1396, 2013.

[2] William C Brown. The history of power transmission by radio waves. *IEEE Transactions on Microwave Theory and Techniques*, pages 1230–1242, 1984.

[3] William C Brown, Roscoe H George, Neil I Heenan, and Roger C Wonson. Microwave to dc converter, March 25 1969. US Patent 3,434,678.

[4] Gokul Rachiraju, Selvakumar Ganesan, and Boselin Prabhu. Evaluation of wireless solar power transmission through satellite (sps). 2017.

[5] Joseph A Paradiso and Thad Starner. Energy scavenging for mobile and wireless electronics. *Pervasive Computing, IEEE*, 4(1):18–27, 2005.

[6] Shad Roundy and Paul K Wright. A piezoelectric vibration based generator for wireless electronics. *Smart Materials and structures*, 13(5):1131, 2004.

[7] Edgar H Callaway Jr. *Wireless sensor networks: architectures and protocols*. CRC press, 2003.

[8] Rangarajan Jegadeesan and Yong-Xin Guo. Topology selection and efficiency improvement of inductive power links. *IEEE Transactions on Antennas and Propagation*, 60(10):4846–4854, 2012.

[9] Jiejian Dai and Daniel C Ludois. A survey of wireless power transfer and a critical comparison of inductive and capacitive coupling for small gap applications. *IEEE Transactions on Power Electronics*, 30(11):6017–6029, 2015.

[10] Andre Kurs, Aristeidis Karalis, Robert Moffatt, John D Joannopoulos, Peter Fisher, and Marin Soljačić. Wireless power transfer via strongly coupled magnetic resonances. *science*, 317(5834):83–86, 2007.

[11] Arthur A Oliner, David R Jackson, and JL Volakis. Antenna engineering handbook. *McGraw Hill*, 2007.

[12] Alanson P Sample, David T Meyer, and Joshua R Smith. Analysis, experimental results, and range adaptation of magnetically coupled resonators for wireless power transfer. *IEEE Transactions on industrial electronics*, 58(2):544–554, 2011.

[13] Rangarajan Jegadeesan, Kush Agarwal, Yong-Xin Guo, Shih-Cheng Yen, and Nitish V Thakor. Wireless power delivery to flexible subcutaneous implants using capacitive coupling. *IEEE Transactions on Microwave Theory and Techniques*, 65(1):280–292, 2017.

[14] Anil Kumar RamRakhyani, Shahriar Mirabbasi, and Mu Chiao. Design and optimization of resonance-based efficient wireless power delivery systems for biomedical implants. *IEEE Transactions on Biomedical Circuits and Systems*, 5(1):48–63, 2011.

[15] Jiejian Dai and Daniel C Ludois. Capacitive power transfer through a conformal bumper for electric vehicle charging. *IEEE Journal of Emerging and Selected Topics in Power Electronics*, 4(3):1015–1025, 2016.

[16] Takehiro Imura, Hiroyuki Okabe, and Yoichi Hori. Basic experimental study on helical antennas of wireless power transfer for electric vehicles by using magnetic resonant couplings. In *Vehicle Power and Propulsion Conference, 2009. VPPC'09. IEEE*, pages 936–940. IEEE, 2009.

[17] P. E. Glaser. The satellite solar power station. In *1973 IEEE G-MTT International Microwave Symposium*, pages 186–188, June 1973.

[18] Peter E Glaser. An overview of the solar power satellite option. *IEEE Transactions on Microwave Theory and Techniques*, 40(6):1230–1238, 1992.

[19] James O McSpadden and John C Mankins. Space solar power programs and microwave wireless power transmission technology. *Microwave Magazine, IEEE*, 3(4):46–57, 2002.

[20] Yu-Chung Cheng, Yatin Chawathe, Anthony LaMarca, and John Krumm. Accuracy characterization for metropolitan-scale wi-fi localization. In *Proceedings of the 3rd*

international conference on Mobile systems, applications, and services, pages 233–245. ACM, 2005.

[21] A. Takacs, A. Okba, H. Aubert, S. Charlot, and P. F. Calmon. Recent advances in electromagnetic energy harvesting and wireless power transfer for iot and shm applications. In *2017 IEEE International Workshop of Electronics, Control, Measurement, Signals and their Application to Mechatronics (ECMSM)*, pages 1–4, May 2017.

[22] J Clerk Maxwell. A dynamical theory of the electromagnetic field. *Philosophical transactions of the Royal Society of London*, 155:459–512, 1865.

[23] Heinrich Hertz and William Thomson Baron Kelvin. *Electric waves.* Macmillan London, 1893.

[24] Margaret Cheney. *Tesla: man out of time.* Simon and Schuster, 2011.

[25] H. Yagi and S. Uda. On the feasibility of power transmission by electric waves. *in Proc. 3rd Pan-Pacific Sci. Congr*, 2(2):1305–1313, 1926.

[26] H. A. H. Boot and J. T. Randall. Historical notes on the cavity magnetron. *IEEE Transactions on Electron Devices*, 23(7):724–729, July 1976.

[27] JF Skowron, GH MacMaster, and WC Brown. The super power cw amplitron. *Microwave J.*, 7, 1964.

[28] Ernest C Okress. *Microwave Power Engineering: Generation, Transmission, Rectification*, volume 1. Academic Press, 2017.

[29] RH George and EM Sabbagh. An efficient means of converting microwave energy to dc using semiconductor diodes. *Proceedings of the IEEE*, 51(3):530–530, 1963.

[30] William C Brown. The history of the development of the rectenna.[solar power satellites]. 1980.

[31] W. C. Brown. Status of the microwave power transmission components for the solar power satellite. *IEEE Transactions on Microwave Theory and Techniques*, 29(12):1319–1327, Dec 1981.

[32] W. Brown. Experiments in the transportation of energy by microwave beam. In *1958 IRE International Convention Record*, volume 12, pages 8–17, March 1964.

[33] Peter E Glaser, OwenE Maynard, JJR Mackovciak, and EI Ralph. Feasibility study of a satellite solar power station. 1974.

[34] RM Dickinson. Evaluation of a microwave high-power reception-conversion array for wireless power transmission. 1975.

[35] RM Dickinson and William C Brown. Radiated microwave power transmission system efficiency measurements. 1975.

[36] William C Brown. Electronic and mechanical improvement of the receiving terminal of a free-space microwave power transmission system. 1977.

[37] JJ Schlesak, A Alden, and T Ohno. Sharp (stationary high altitude relay platform)-rectenna and low altitude tests. In *GLOBECOM'85-Global Telecommunications Conference*, pages 960–964, 1985.

[38] R Dickinson and O Maynard. Ground based wireless and wired power transmission cost comparison. 1999.

[39] H Matsumoto, N Kaya, I Kimura, S Miyatake, M Nagatomo, and T Obayashi. Minix project toward the solar power satellite-rocket experiment of microwave energy transmission and associated nonlinear plasma physics in the ionosphere. In *ISAS Space Energy Symposium*, pages 69–76, 1982.

[40] Y Fujino. A rectenna for milax. In *Proc. of 1st Wireless Power Transmission Conference*, pages 273–277, 1993.

[41] N Kaya, H Matsumoto, and R Akiba. Rocket experiment mets-microwave energy transmission in space. In *SPS 91-Power from Space*, pages 336–342, 1991.

[42] H. Matsumoto. Research on solar power satellites and microwave power transmission in japan. *IEEE Microwave Magazine*, 3(4):36–45, Dec 2002.

[43] J. Heikkinen and M. Kivikoski. A novel dual-frequency circularly polarized rectenna. *IEEE Antennas and Wireless Propagation Letters*, 2:330–333, 2003.

[44] C. Song, Y. Huang, P. Carter, J. Zhou, S. Yuan, Q. Xu, and M. Kod. A novel six-band dual cp rectenna using improved impedance matching technique for ambient rf energy harvesting. *IEEE Transactions on Antennas and Propagation*, 64(7):3160–3171, July 2016.

[45] H. Kamoda, S. Kitazawa, N. Kukutsu, and K. Kobayashi. Loop antenna over artificial magnetic conductor surface and its application to dual-band rf energy harvesting. *IEEE Transactions on Antennas and Propagation*, 63(10):4408–4417, Oct 2015.

[46] Yong Huang, N. Shinohara, and H. Toromura. A wideband rectenna for 2.4 ghz-band rf energy harvesting. In *2016 IEEE Wireless Power Transfer Conference (WPTC)*, pages 1–3, May 2016.

[47] M. Arrawatia, M. S. Baghini, and G. Kumar. Broadband bent triangular omnidirectional antenna for rf energy harvesting. *IEEE Antennas and Wireless Propagation Letters*, 15:36–39, 2016.

[48] C. Song, Y. Huang, J. Zhou, J. Zhang, S. Yuan, and P. Carter. A high-efficiency broadband rectenna for ambient wireless energy harvesting. *IEEE Transactions on Antennas and Propagation*, 63(8):3486–3495, Aug 2015.

[49] P. Lu, X. S. Yang, J. L. Li, and B. Z. Wang. Polarization reconfigurable broadband rectenna with tunable matching network for microwave power transmission. *IEEE Transactions on Antennas and Propagation*, 64(3):1136–1141, March 2016.

[50] Zoya Popovic, Sean Korhummel, Steven Dunbar, Robert Scheeler, Arseny Dolgov, Regan Zane, Erez Falkenstein, and Joseph Hagerty. Scalable rf energy harvesting. *IEEE Transactions on Microwave Theory and Techniques*, 62(4):1046–1056, Apr 2014.

[51] J.A. Hagerty, F.B. Helmbrecht, W.H. McCalpin, R. Zane, and Z.B. Popovic. Recycling ambient microwave energy with broad-band rectenna arrays. *Microwave Theory and Techniques, IEEE Transactions on*, 52(3):1014–1024, 2004.

[52] M. Piuela, P. D. Mitcheson, and S. Lucyszyn. Ambient rf energy harvesting in urban and semi-urban environments. *IEEE Transactions on Microwave Theory and Techniques*, 61(7):2715–2726, July 2013.

[53] Jamal Zbitou, Mohamed Latrach, and Serge Toutain. Hybrid rectenna and monolithic integrated zero-bias microwave rectifier. *IEEE Transactions on Microwave Theory and Techniques*, 54(1):147–152, 2006.

[54] Yu-jiun Ren and Kai Chang. 5.8-GHz Circularly Polarized Dual-Diode Rectenna and Rectenna Array for Microwave Power Transmission. *IEEE Trans. Microw. Theory Tech.*, 54(4):1495–1502, jun 2006.

[55] Y.J. Ren, M.F. Farooqui, and K. Chang. A compact dual-frequency rectifying antenna with high-orders harmonic-rejection. *Antennas and Propagation, IEEE Transactions on*, 55(7):2110–2113, 2007.

[56] Faruk Erkmen, Thamer S Almoneef, and Omar M Ramahi. Electromagnetic energy harvesting using full-wave rectification. *IEEE Transactions on Microwave Theory and Techniques*, 65(5):1843–1851, 2017.

[57] Erez Falkenstein, Michael Roberg, and Zoya Popovic. Low-power wireless power delivery. *IEEE Transactions on microwave theory and techniques*, 60(7):2277–2286, 2012.

[58] K. Niotaki, S. Kim, S. Jeong, A. Collado, A. Georgiadis, and M. M. Tentzeris. A compact dual-band rectenna using slot-loaded dual band folded dipole antenna. *IEEE Antennas and Wireless Propagation Letters*, 12:1634–1637, 2013.

[59] Z. Harouni, L. Cirio, L. Osman, A. Gharsallah, and O. Picon. A dual circularly polarized 2.45-ghz rectenna for wireless power transmission. *Antennas and Wireless Propagation Letters, IEEE*, 10:306–309, 2011.

[60] W. H. Tu, S. H. Hsu, and K. Chang. Compact 5.8-ghz rectenna using stepped-impedance dipole antenna. *IEEE Antennas and Wireless Propagation Letters*, 6:282–284, 2007.

[61] Christopher R Valenta and Gregory D Durgin. Harvesting wireless power: Survey of energy-harvester conversion efficiency in far-field, wireless power transfer systems. *IEEE Microwave Magazine*, 15(4):108–120, 2014.

[62] J. Heikkinen and M. Kivikoski. A novel dual-frequency circularly polarized rectenna. *Antennas and Wireless Propagation Letters, IEEE*, 2:330–333, 2003.

[63] N. P. Basta, E. A. Falkenstein, and Z. Popovic. Bow-tie rectenna arrays. In *2015 IEEE Wireless Power Transfer Conference (WPTC)*, pages 1–4, May 2015.

[64] W. Zhao, K. Choi, S. Bauman, Z. Dilli, T. Salter, and M. Peckerar. A radio-frequency energy harvesting scheme for use in low-power ad hoc distributed networks. *IEEE Transactions on Circuits and Systems II: Express Briefs*, 59(9):573–577, Sept 2012.

[65] Ning Zhu, Richard W Ziolkowski, and Hao Xin. A metamaterial-inspired, electrically small rectenna for high-efficiency, low power harvesting and scavenging at the global positioning system l1 frequency. *Applied Physics Letters*, 99(11):114101, 2011.

[66] M. Ali, G. Yang, and R. Dougal. Miniature circularly polarized rectenna with reduced out-of-band harmonics. *IEEE Antennas and Wireless Propagation Letters*, 5:107–110, 2006.

[67] J. A. G. Akkermans, M. C. van Beurden, G. J. N. Doodeman, and H. J. Visser. Analytical models for low-power rectenna design. *IEEE Antennas and Wireless Propagation Letters*, 4:187–190, 2005.

[68] G. Monti, L. Tarricone, and M. Spartano. X-band planar rectenna. *IEEE Antennas and Wireless Propagation Letters*, 10:1116–1119, 2011.

[69] T. Matsunaga, E. Nishiyama, and I. Toyoda. 5.8-ghz stacked differential rectenna suitable for large-scale rectenna arrays with dc connection. *IEEE Transactions on Antennas and Propagation*, 63(12):5944–5949, Dec 2015.

[70] Hucheng Sun, Yong-xin Guo, Miao He, and Zheng Zhong. A dual-band rectenna using broadband yagi antenna array for ambient rf power harvesting. *IEEE Antennas and Wireless Propagation Letters*, 12:918–921, Jul 2013.

[71] Fangyi Xie, Guo-Min Yang, and Wen Geyi. Optimal design of an antenna array for energy harvesting. *IEEE Antennas and Wireless Propagation Letters*, 12:155–158, 2013.

[72] X. X. Yang, C. Jiang, A. Z. Elsherbeni, F. Yang, and Y. Q. Wang. A novel compact printed rectenna for data communication systems. *IEEE Transactions on Antennas and Propagation*, 61(5):2532–2539, May 2013.

[73] S. D. Assimonis, S. N. Daskalakis, and A. Bletsas. Sensitive and efficient rf harvesting supply for batteryless backscatter sensor networks. *IEEE Transactions on Microwave Theory and Techniques*, 64(4):1327–1338, April 2016.

[74] Thamer S Almoneef, Hu Sun, and Omar M Ramahi. A 3-d folded dipole antenna array for far-field electromagnetic energy transfer. *IEEE Antennas and Wireless Propagation Letters*, 15:1406–1409, 2016.

[75] S. Y. Yang and J. Kim. Wireless power transmission using dipole rectennas made on flexible cellulose membrane. *IET Microwaves, Antennas Propagation*, 6(7):756–760, May 2012.

[76] S. Ladan, A. B. Guntupalli, and K. Wu. A high-efficiency 24 ghz rectenna development towards millimeter-wave energy harvesting and wireless power transmission.

IEEE Transactions on Circuits and Systems I: Regular Papers, 61(12):3358–3366, Dec 2014.

[77] Omar M Ramahi, Thamer S Almoneef, Mohammed AlShareef, and Muhammed S Boybay. Metamaterial particles for electromagnetic energy harvesting. *Applied Physics Letters*, 101(17):173903, 2012.

[78] Babak Alavikia, Thamer S Almoneef, and Omar M Ramahi. Electromagnetic energy harvesting using complementary split-ring resonators. *Applied Physics Letters*, 104(16):163903, 2014.

[79] Mohammed R AlShareef and Omar M Ramahi. Electrically small particles combining even-and odd-mode currents for microwave energy harvesting. *Applied Physics Letters*, 104(25):253906, 2014.

[80] Thamer S Almoneef and Omar M Ramahi. Metamaterial electromagnetic energy harvester with near unity efficiency. *Applied Physics Letters*, 106(15):153902, 2015.

[81] Mohamed El Badawe and Omar M Ramahi. Polarization independent metasurface energy harvester. In *Proceedings of the 17th annual IEEE Wireless and Microwave Technology Conference*. IEEE, April 11-13, 2016.

[82] Mohamed El Badawe, Thamer S Almoneef, and Omar M Ramahi. A metasurface for conversion of electromagnetic radiation to dc. *AIP Advances*, 7(3):035112, 2017.

[83] Thamer S Almoneef, Faruk Erkmen, and Omar M Ramahi. Harvesting the energy of multi-polarized electromagnetic waves. *Scientific Reports*, 7(1):14656, Nov 2017.

[84] Ari Juels. Rfid security and privacy: A research survey. *IEEE journal on selected areas in communications*, 24(2):381–394, 2006.

[85] F. Huang, C. Lee, C. Chang, L. Chen, T. Yo, and C. Luo. Rectenna application of miniaturized implantable antenna design for triple-band biotelemetry communication. *IEEE Transactions on Antennas and Propagation*, 59(7):2646–2653, July 2011.

[86] Liguang Xie, Yi Shi, Y Thomas Hou, and Andwenjing Lou. Wireless power transfer and applications to sensor networks. *IEEE Wireless Communications*, 20(4):140–145, 2013.

[87] Joseph Polastre, Jason Hill, and David Culler. Versatile low power media access for wireless sensor networks. In *Proceedings of the 2nd international conference on Embedded networked sensor systems*, pages 95–107. ACM, 2004.

[88] S Sasaki, JAXA Advanced Mission Research Group, et al. Ssps development road map, iac 09. *C3. 1.4, October 2009*, 2009.

[89] George Goubau and F Schwering. On the guided propagation of electromagnetic wave beams. *IRE Transactions on Antennas and Propagation*, 9(3):248–256, 1961.

[90] G Goubau. Microwawe power transmission from an orbiting solar power station. *Journal of Microwave Power*, 5(4):224–231, 1970.

[91] Constantine A. Balanis. *Antenna theory : analysis and design.* Hoboken, NJ : John Wiley, Hoboken, NJ, third edition, 2005.

[92] Omar M. Ramahi, Thamer S. Almoneef, Mohammad Alshareef, and Muhammed S. Boybay. Metamaterial particles for electromagnetic energy harvesting. *Applied Physics Letters*, 101(17):173903–173903–5, Oct. 2012.

[93] J Van Bladel. On the equivalent circuit of a receiving antenna. *Antennas and Propagation Magazine, IEEE*, 44(1):164–165, 2002.

[94] T-W Yoo. Experimental and theoretical study on 35 ghzrf-to-dc power conversion receiver for millimeter-wave beamed power transmission. 1994.

[95] BHI Strassner. Microwave rectifying circuits and antennas for radio frequency identification and wireless power transmission applications. 2003.

[96] James O McSpadden, Lu Fan, and Kai Chang. Design and experiments of a high-conversion-efficiency 5.8-ghz rectenna. *IEEE Transactions on Microwave Theory and Techniques*, 46(12):2053–2060, 1998.

[97] Adnan Harb. Energy harvesting: State-of-the-art. *Renewable Energy*, 36(10):2641–2654, Oct. 2011.

[98] J.A Paradiso and T. Starner. Energy scavenging for mobile and wireless electronics. *Pervasive Computing, IEEE*, 4(1):18–27, Jan. 2005.

[99] L. Ukkonen, L. Sydanheimo, and M. Kivikoski. Effects of metallic plate size on the performance of microstrip patch-type tag antennas for passive rfid. *Antennas and Wireless Propagation Letters, IEEE*, 4:410–413, Dec. 2005.

[100] Jen-Yea Jan and Liang-Chih Tseng. Small planar monopole antenna with a shorted parasitic inverted-l wire for wireless communications in the 2.4-, 5.2-, and 5.8-ghz bands. *Antennas and Propagation, IEEE Transactions on*, 52(7):1903–1905, July 2004.

[101] Qinghua Lai, G. Almpanis, C. Fumeaux, H. Benedickter, and R. Vahldieck. Comparison of the radiation efficiency for the dielectric resonator antenna and the microstrip antenna at ka band. *Antennas and Propagation, IEEE Transactions on*, 56(11):3589–3592, Nov. 2008.

[102] H. Jabbar, Y.S. Song, and T.T. Jeong. Rf energy harvesting system and circuits for charging of mobile devices. *Consumer Electronics, IEEE Transactions on*, 56(1):247–253, Feb. 2010.

[103] Babak Alavikia, Thamer S. Almoneef, and Omar M. Ramahi. Electromagnetic energy harvesting using complementary split-ring resonators. *Applied Physics Letters*, 104(16):163903–163903–4, Oct. 2014.

[104] Mohammed AlShareef, , and Omar M. Ramahi. Electrically small particles combining even- and odd-mode currents for microwave energy harvesting,. *Applied Physics Letters*, 104:253906–253906–4, 2014.

[105] Kwok-Wa Leung, Eng Hock Lim, and Xiao Sheng Fang. Dielectric resonator antennas: From the basic to the aesthetic. *Proceedings of the IEEE*, 100(7):2181–2193, July 2012.

[106] K. M. (K Luk and K. W. (K Leung. *Dielectric resonator antennas*. Baldock, England : Research Studies Press ; Philadelphia : Institute of Physics Publishing, Baldock, England : Philadelphia, 2003.

[107] A Petosa, A Ittipiboon, Y.M.M. Antar, D. Roscoe, and M. Cuhaci. Recent advances in dielectric-resonator antenna technology. *Antennas and Propagation Magazine, IEEE*, 40(3):35–48, June 1998.

[108] Aldo Petosa. *Dielectric resonator antenna handbook*. Artech House London, 2007.

[109] Yih-Chien Chen, Shih-Min Tsao, Chang-Shin Lin, Shun-Chung Wang, and Yu-Hua Chien. Microwave dielectric properties of 0.95mgtio(3)-0.05catio(3) for application in dielectric resonator antenna. *Journal of Alloys and Compounds*, 471(1-2):347–351, Mar. 2009.

[110] I.F. Akyildiz, Weilian Su, Y. Sankarasubramaniam, and E. Cayirci. A survey on sensor networks. *Communications Magazine, IEEE*, 40(8):102–114, Aug. 2002.

[111] James William Kingsley, Rebecca Thomas, and Susan Williams. Attaching antenna structures to electrical feed structures, Feb. 2007. US Patent 7,183,975.

[112] L. Roy, N. Berthereau, N. Hojjat, K. Kautio, and H. Panesaar. Dielectric resonator antenna with microstrip-waveguide transition in ltcc. *Electronics Letters*, 42(19):1078–1079, Sep. 2006.

[113] R. Kumar Mongia and A Ittipiboon. Theoretical and experimental investigations on rectangular dielectric resonator antennas. *Antennas and Propagation, IEEE Transactions on*, 45(9):1348–1356, Sep. 1997.

[114] O. M. Ramahi and A. Ashoor. Dielectric resonator antennas and arrays for electromagnetic energy harvesting. *US Provisional Patent Application No. 62035265.*

[115] ANSYS HFSS Version 15.0.0, Ansys Inc., http://www.ansys.com.

[116] A Petosa, R.K. Mongia, A Ittipiboon, and J.S. Wright. Design of microstrip-fed series array of dielectric resonator antennas. *Electronics Letters*, 31(16):1306–1307, Aug. 1995.

[117] G.P. Junker, A.A. Kishk, A.W. Glisson, and D. Kajfez. Effect of an air gap around the coaxial probe exciting a cylindrical dielectric resonator antenna. *Electronics Letters*, 30(3):177–178, Feb. 1994.

[118] Thamer S Almoneef and Omar M Ramahi. Metamaterial electromagnetic energy harvester with near unity efficiency. *Applied Physics Letters*, 106(15):153902, 2015.

[119] Ahmed Z Ashoor and Omar M Ramahi. Dielectric resonator antenna arrays for microwave energy harvesting and far-field wireless power transfer. *Progress In Electromagnetics Research C*, 59:89–99, 2015.

[120] ANSYS HFSS Version 16.0.0, Ansys Inc., http://www.ansys.com.

[121] ANSYS HFSS. (1970). Workshop 9-1: Unit cell analysis (infinite array). [Online]. Available: https://www.scribd.com/document/320371134/Ansys-Hfss-Antenna-w09-1-Unit-Cell [Accessed: July 18, 2017].

[122] Ronald J Gutmann and Jose M Borrego. Power combining in an array of microwave power rectifiers. *IEEE Transactions on Microwave Theory and Techniques*, 27(12):958–968, 1979.

[123] Naoki Shinohara and Hiroshi Matsumoto. Dependence of dc output of a rectenna array on the method of interconnection of its array elements. *Electrical Engineering in Japan*, 125(1):9–17, 1998.

[124] Ahmed Z Ashoor, Thamer S Almoneef, and Omar M Ramahi. A planar dipole array surface for electromagnetic energy harvesting and wireless power transfer. *IEEE Transactions on Microwave Theory and Techniques*, 2017.

[125] Peng Xu, Shen-Yun Wang, and Wen Geyi. Design of an effective energy receiving adapter for microwave wireless power transmission application. *AIP Advances*, 6:105010, 2016.

[126] Richard A Shelby, David R Smith, and Seldon Schultz. Experimental verification of a negative index of refraction. *science*, 292(5514):77–79, 2001.

[127] David Schurig, JJ Mock, BJ Justice, Steven A Cummer, John B Pendry, AF Starr, and DR Smith. Metamaterial electromagnetic cloak at microwave frequencies. *Science*, 314(5801):977–980, 2006.

[128] R Liu, C Ji, JJ Mock, JY Chin, TJ Cui, and DR Smith. Broadband ground-plane cloak. *Science*, 323(5912):366–369, 2009.

[129] NI Landy, S. Sajuyigbe, JJ Mock, DR Smith, and WJ Padilla. Perfect metamaterial absorber. *Physical review letters*, 100(20):207402, 2008.